Investigating topographic controls on Antarctic Ice Sheet flow and retreat

Santiago Munevar Garcia
Charlottesville, Virginia

B.S. Geography & Environmental Science, University of Maryland Baltimore County, 2018

A Dissertation presented to the Graduate Faculty
of the University of Virginia in Candidacy for the Degree of
Doctor of Philosophy

Department of Environmental Sciences

University of Virginia
July 2024

Committee Members:
Professor Lauren Miller
Professor Ajay Limaye
Professor Patricia Wiberg
Professor Antonios Mamalakis

Abstract

The Antarctic Ice Sheet has the potential to contribute over a meter of sea level rise by the end of the century. Despite recent advancements in direct observations and understanding, key processes at the ice-bed interface—crucial for governing its complex ice dynamics—remain unconstrained. The work presented here leverages high-resolution bathymetry from deglaciated landscapes to gain insight into local- and subglacial-scale processes governing ice sheet dynamics. To quantify the impact of subglacial bed roughness on ice flow, Chapter 2 compares different methods to assess their suitability. Results demonstrate that bed roughness measurements are significantly influenced by orientation, scale, and methodology, highlighting the importance of standardized approaches. The standard deviation method emerged as a robust tool for characterizing bed roughness, particularly in the context of paleo-ice stream bed. However, limitations imposed by low-resolution topography data, especially beneath contemporary Thwaites Glacier, West Antarctica, underscore the need for improved data acquisition. To enhance the understanding of subglacial landform evolution and its implications for ice dynamics, Chapter 3 applies an automated landform identification method to high-resolution bathymetry in the Western Ross Sea. This approach revealed a substantial increase in the number of identified landforms compared to traditional visual methods, providing new insights into landform morphology and distribution. Statistical analyses demonstrated a strong correlation between local bed slope and landform morphometrics, with steeper reverse slopes inhibiting vertical growth and influencing landform amplitude and width. Moreover, metrics suggest that ice sheet retreat has exhibited both steady and episodic phases, influenced by long-term climate variability. To explore the mechanisms controlling the formation and geometry of grounding zone wedges (GZWs), landforms formed at the terminus of marine-terminating glaciers and ice streams, a numerical model of sediment accumulation at the grounding line is used to investigate controls such as local bed slope, the depth of the deformable layer, and stoss angle. While the model successfully reproduced the asymmetry shape of GZWs and shows sediment flux to be a key control in the dimensions of GZWs, further research should incorporate additional climate forcings and local environmental variables to improve model performance. Collectively, this research advances our understanding of the critical role of small-scale topography in controlling AIS flow and retreat. By improving the characterization of bed toughness, identifying subglacial landforms, and modeling glacier-bed interactions, this dissertation contributes to a more comprehensive picture of ice sheet dynamics and its findings can refine and improve ice sheet models for better predictions of future sea level rise.

Table of contents.

List of tables

List of figures

Figure 2.7. Difference in roughness measurements of parallel transects between high-resolution topography and BedMachine, showing where BedMachine under- and over-estimates roughness (red and green shades, respectively). Roughness for sites 1 and 3 **(A,B)** is derived from bathymetry; sites 5 and 6 **(C,D)** is from swath-radar (Holschuh et al., 2020).

Figure 3.1. Location of moraine and GZW transects in the Western Ross Sea. Background bathymetry from Morlighem et al., 2020. Dashed white line indicates LGM ice extent. CrB (Crary Bank), CB (Central Basin), JT (JOIDES Trough), PB (Pennell Bank), PT (Pennell Trough), RB (Ross Bank), GCB (Glomar Challenger Basin).

Figure 3.2. Example transect illustrating landforms identified along a moraine transect. Amplitude and width properties are denoted by the red and yellow lines, respectively. The cross-sectional area is computed by multiplying amplitude by width. Width-to-amplitude ratio is computed by dividing width by amplitude, with higher values signifying greater asymmetry.

Figure 3.3. Zoomed in view of Figure 3.2, highlighting the spacing between landforms, as well as the amplitude and width (along-flow length) measured for each landform.

Figure 3.4. Frequency distribution of **(A)** amplitude, **(B)** width, **(C)** cross-sectional (XS) area, and **(D)** width-to-amplitude ratio of landforms identified.

Figure 3.5. Heatmap of Pearson correlation coefficient between local bed slope and morphometric properties (width, amplitude, cross-sectional area, width-to-amplitude ratio) across individual transects for **(A)** moraines and **(B)** GZWs.

Figure 3.6. Distribution of landform spacing across different transects for moraine and GZWs. The red dashed line indicates average spacing for the respective population.

Figure 3.7. Heatmap of Pearson correlation coefficient between landform spacing and morphometric properties (width, amplitude, cross-sectional area, width-to-amplitude ratio) across individual transects for **(A)** moraines and **(B)** GZWs.

Figure 3.8. Frequency distribution of local bed slope and landforms identified.

Figure 4.1. (A) Steady-state ice stream profile, **(B)** zoomed-in at the grounding zone. **(C)** Horizontal ice velocity profile. **(D)** Transition from power-law inland to Coulomb-plastic near the grounding zone.

Figure 4.2. Plots illustrating the size difference of the constructed GZW based on varying stoss angles **(A)** -0.01 degrees **(B)** -0.02 degrees, **(C)** -0.03 degrees, **(D)** -0.04 degrees. Ice dynamics, bed slope, and depth of deformable layer (25 cm) held constant. Model ran for 1 kyr at 10 yr time steps. 20 yr increments shown in plots as successive black lines.

Figure 4.3. Plots illustrating the size difference of the constructed GZW based on the depth of the deformable layer parameter. **(A)** 5 cm, **(B)** 10 cm, **(C)** 15 cm, **(D)** 20 cm. Ice dynamics, bed

slope, and stoss angle (0.02) held constant. Model ran for 1thousan years at 10 year time steps. 20 year increments shown in plots as successive black lines.

Figure 4.4. Impact of grounding line velocity on GZW formation. The blue line indicates the evolution of grounding line velocity (m/yr; shown on the left y-axis) over time as retreat advances. Brown line depicts amplitude (m; shown on the right y-axis) of constructed GZW.

Figure 4.5. Model run for time step 22 kyr after retreat from steady state, illustrating example of complete instability, where high grounding line velocities do not allow the vertical deposition of sediment. Note differences in ranges for x- and y-axes compared to Figures 4.2 and 4.3.

Figure A2.1. Elevation datasets at Jakobshavn Glacier. **(A)** First topographic realization from MacKie et al. (2021). **(B)** BedMachine (Morlighem et al., 2017).

Figure A2.2. Absolute roughness measurements for orthogonal transects in sites 1-4 showing the difference in spatial distribution between scales and methods. White arrows indicate direction of paleo ice-flow.

Figure A2.3. Absolute roughness measurements for parallel and orthogonal transects in sites 5-6 showing the difference in spatial distribution between scales. White arrows indicate direction of paleo-ice flow.

Figure A2.4. Absolute roughness measurements. **(A)** First topographic realization from Mackie et al. (2021), SD method. **(B)** SD Roughness from BedMachine dataset (Morlighem et al., 2017).

Figure A2.5. Difference in roughness measurements between topographic realization from Mackie et al. (2021) and BedMachine (Morlighem et al., 2017). BedMachine under-represents roughness in green-shaded areas.

Figure A2.6. Anisotropy values calculated from the BedMachine dataset at every intersection point between parallel and orthogonal transects at site 1 **(A)** and site 3 **(B)** represent directionality of roughness measurements at the local scale. Orthogonal roughness dominates in the purple shades, parallel dominates in the green. White indicate isotropic or random surfaces.

Figure A3.1. Example transect illustrating landforms identified along a moraine transect. Amplitude and width properties are denoted by the red and yellow lines, respectively. The cross-sectional area is computed by multiplying amplitude by width. Width-to-amplitude ratio is computed by dividing width by amplitude, with higher values signifying greater asymmetry.

Figure A5.1. Figure from Prothro et al. (2020) showing the distribution of surface ages. Relative ages are represented by the size of core marker.

Acknowledgements

No podría comenzar sin reconocer a las personas que han estado conmigo desde el principio. Quiero expresar mi más sincero agradecimiento a mi familia por su amor incondicional y apoyo constante a lo largo de estos últimos cinco años. A mis maravillosos padres, les agradezco por sus inmensos sacrificios, los riesgos que asumieron, las dificultades que soportaron y el coraje demostrado al decidir dejar nuestra Colombia. A Juanis, por personificar la amistad y el apoyo, y por las largas travesías para ir a conciertos. A mis abuelos, por su constante aliento, interés genuino en mi investigación, y apoyo en los momentos en que más los necesité. Y al resto de mi familia que, desde lejos, siempre me apoyaron.

Molly, thank you for being by my side every step of this journey with unwavering support. Your presence has been a constant reminder of what truly matters in life. Through all of this, I have learned more from you about resilience, compassion, and dedication than I ever could from the PhD process itself. I am deeply grateful for your love and encouragement.

A huge amount of gratitude goes to Dr. Lauren Miller for believing in me from the very beginning. Thank you not only for your vocal support but for always backing it up with your actions. I have greatly admired the way you stand up for your students and your care towards them not only as scientists but as individuals. Your understanding and empathy, especially during challenging times, have been invaluable. I feel extremely lucky to have had you as an advisor.

To everyone in the Ice & Ocean group—Alie, Marion, Tahi, Medha, Alejandra, Natalia—thank you for the many classes, meetings, field trips, and conference travels. These experiences provided a break from academia and offered genuine friendship. I have learned immensely from each of you. To all the students I had during my PhD, thank you for making teaching a memorable and enjoyable experience. It turned out to be one of my favorite aspects of graduate school, which I had not anticipated.

A heartfelt thanks to my longtime friends—Bilaal, Alex, and Jake—and the rest of the Baltimore crew. Your steadfast friendship over the past 15 years has been a constant anchor, helping me feel at home from the start.

To my mud sisters: Asmara, Elaine, and Rachel, sailing with you will remain one of my favorite memories. I also want to thank the rest of the NBP 20-02 party for all the expertise and mentorship provided. I am especially grateful to Lauren and Dr. Julia Wellner for their support and reassurance during the eventful and uncertain time following the cruise.

Special thanks to Drs. Alex Robel and John Christian for welcoming me to their lab and generously sharing their time and expertise with me. I am particularly grateful to John for making the world of numerical modeling more intuitive and less intimidating, which was crucial for the development of Chapter 4.

Lastly, I owe an immeasurable debt of gratitude to the Kennedy family. I simply would not have accomplished any of this without the support you gave me. Thank you.

The funding for this work comes from the National Science Foundation Office of Polar Programs (Grant 1745043).

Chapter 1: Introduction

Ice sheets are arguably among the largest, most dynamic, and influential features on Earth, covering vast areas of land and impacting global climate and sea level (Oppenheimer et al., 2019). The Antarctic Ice Sheet (AIS) is the largest land ice reservoir and holds approximately 58 meters of potential sea level rise (DeConto et al., 2021). Like any natural system, the AIS is influenced by a variety of environmental forcings, including gravity-driven flow, basal friction as ice interacts with the underlying landscape, internal ice deformation, and interactions with the ocean and atmosphere. This combination of factors causes ice sheets to fluctuate over sub-annual to geologic timescales of hundreds, thousands, and millions of years (Noble et al., 2020). A solid understanding of the evolution of non-linear ice sheet behavior, or ice dynamics, is essential for assessing ice sheet stability, which can be monitored by tracking its mass balance and the position of its terminus, or grounding line - the point where the ice sheet transitions from grounded to the land to a floating ice shelf in marine environments. Even minor changes in the imbalance of an ice sheet can shift the position of the grounding line, which is sensitive to changes in ice flux and effective changes in water depth, and have significant global impacts (Rignot, 1998; De Angelis & Skvarca, 2003; Robel et al., 2018).

Satellite observations over the past few decades have revealed patterns of AIS mass loss, which have accelerated since the 1990s, resulting in a significant increase in global mean sea level (Rignot et al., 2019; Shepherd et al., 2019; Otosaka et al., 2023). These observations indicate the extent of ice sheet changes and provide insight into potential future sea level rise. Despite observed trends in sea level rise, significant uncertainty remains in projecting future contributions from ice sheets (Robel et al., 2019; Lowry et al., 2019). This uncertainty stems from our incomplete understanding of the processes governing ice dynamics over longer-time scales such as decades and centuries (Nowicki & Seroussi, 2018; Bamber et al., 2019). Improving the representation of subglacial processes, which are influential for ice flow velocities and thus ice mass balance, in numerical ice sheet models is critical for better constraining of projections of ice sheet evolution in the future (Vaughan et al., 2013; Kazmierczak et al., 2022).

The mass balance of an ice sheet represents the net difference between mass gained through surface accumulation and mass lost through processes like ice discharge at the grounding line and melting at ice-ocean interfaces. Over the last decade, evidence has emerged highlighting the crucial role of intrusion of relatively warm circumpolar deep water (CDW) in driving sub-ice shelf melting of the AIS, making it the main driver of Antarctica's contribution to sea level rise (Pritchard et al., 2012). These CDW incursions onto the continental shelf follow bathymetric troughs, and enhance melt rates at the modern margins of ice streams that carved out glacial troughs over repeated glacial cycles. Ice streams are regions within an ice sheet where ice flow velocities are significantly higher than the surrounding ice. They account for approximately 90% of ice discharge from the interior of the ice sheet to the ocean and play a crucial role in controlling ice dynamics (Shepherd et al., 2018). Tracking the ice dynamics of major glaciers and ice streams—characterized by high spatiotemporal variability driven largely by topographic settings—provides crucial insights into the stability of ice sheets (Winsborrow et al., 2010). Their behavior is primarily influenced by subglacial processes that create landforms capable of modifying ice dynamics through changes in bed topography and basal shear stress (Livingstone et al. 2012).

Overall, by examining observations from the deglaciated continental shelf, this dissertation explores examples of ice sheet retreat since the Last Glacial Maximum (LGM) and underscores the importance of locally constraining bed topography to better understand the processes governing grounding line migration.

1.1 Topography as a control on ice dynamics

Landforms created by ice streams, often preserved as physical footprints of glacial ice, are invaluable for understanding the deglacial history of the AIS (Stokes, 2018). Despite limited direct observations of contemporary ice stream beds using geophysical methods, preserved landforms on the deglaciated continental shelf, such as those found in paleo-ice stream beds from the LGM, provide critical insights into past ice dynamics. Diverse landforms assemblages, created through both erosional and depositional processes, have been used to reconstruct the deglacial histories of paleo-ice streams, revealing patterns of asynchronous retreat across paleo-ice stream troughs in Antarctica (Livingstone et al., 2012; Anderson et al., 2014; Dowdeswell et al., 2016). Interpretation of these landforms helps infer how the ice sheet responded to environmental changes, thereby enhancing our understanding of ice dynamics and its implications for ice sheet stability.

In addition to constructional landforms, antecedent topography also plays an important role in modulating ice dynamics and grounding line migration. Topographic highs act as pinning points capable of reducing ice flow velocities by increasing basal drag through lateral friction and even promoting ice sheet advance during periods of overall ice sheet retreat (Favier et al., 2012; Jamieson et al., 2014). Recent modeling work supports bed topography as a key control on grounding line retreat observed in recent decades (Favier et al., 2016; Seroussi et al., 2017).

1.2 Importance of small-scale topographic analysis

The recent mass loss from the AIS is primarily dictated by ocean temperatures and bed topography. Elevation datasets reveal deep subglacial troughs (Morlighem et al., 2020), especially in West Antarctica, where thick ice results in greater driving stresses and faster velocities which enhances melt rates and promotes basal sliding. Large portions of West Antarctica are grounded below sea level and on a reverse bed slope, where water depth increases inland. This configuration makes it particularly susceptible to Marine Ice Sheet Instability (MISI). The MISI theory posits that as the grounding line retreats on a reverse slope, a positive feedback loop is triggered whereby the increase in ice thickness at the grounding line promotes greater ice discharge, leading to further retreat (Weertman, 1974; Pattyn et al., 2017; Robel et al., 2019).

High-resolution elevation data for Antarctica remains critically sparse. Although continent-wide datasets exist, they rely on limited observations, resulting in coarse spatial resolutions exceeding 500 meters. Recent research expeditions have increased the extent of bathymetric and seismic surveys in key sectors of Antarctica like the Amundsen, Bellingshausen, and Ross Seas. However, unpredictable ice conditions lead to data gaps that hinder complete accurate bathymetric mapping. These gaps force a reliance on interpolation methods, which can misrepresent terrain at local scales and create challenges in understanding the impact of small-scale topography on ice dynamics (MacKie et al., 2021). While existing elevation datasets have greatly advanced our understanding of the influence bed topography exerts on ice

dynamics, their inability to resolve processes at a local scale remains a significant gap in glaciology. This knowledge gap is particularly evident in numerical ice sheet models, which group basal sliding and subglacial deformation processes together to simulate basal motion. Basal motion has a strong influence on ice flow and is controlled by subglacial hydrology and bed roughness (Joughin et al., 2019; Pollard and DeConto 2012, Bingham et al., 2017), both of which are often overlooked or only considered on large continental scales (Bennett, 2003; Taylor et al., 2004). **Chapter 2 utilizes high-resolution bathymetry to explore the impact of methodology and scale selected to quantify bed roughness and its usefulness in identifying patterns of streaming flow, which highlights the need for a standardized way of quantifying bed roughness and emphasizes the limitations of low-resolution continent-wide datasets in characterizing topographic variability.**

High-resolution bathymetric datasets for Antarctica, typically ranging between 20 and 50 meters, offer much lower resolution compared to subaerial environments where direct landform observations have significantly improved the relationship between environmental forcings and retreat patterns (Bingham and Siegert, 2009; Gudlaugsson et al., 2013) . Recent advancements in marine geophysics have seen autonomous underwater vehicles that can image the sub-ice shelf environment near the grounding line at unprecedented spatial resolutions. These surveys have illuminated tidal lifting processes which create a distinctive signature on the seafloor that can be used to measure retreat rates of glacier systems (Dowdeswell et al., 2020; Graham et al., 2022). This exemplifies how high-resolution bathymetry can demonstrate the interplay between bed topography and ice dynamics. **Chapter 3 combines high-resolution bathymetry with an automated landform extraction method to identify hundreds of previously unrecognized small-scale ice-marginal landforms in the Western Ross Sea.** Interpretation of the morphometric properties of these landforms allow us to infer the control of local topography on retreat patterns since the LGM.

1.3 Controls on the timing and geometry of grounding zone wedges

Glacier flow is a complex process driven by gravity and influenced by interactions at the ice-bed interface. The three primary mechanisms by which ice flows towards the ocean are internal deformation, basal sliding, and subglacial deformation (Boulton, 1996). Internal deformation occurs through ice creep, where ice behaves as a nonlinear viscous material and deforms when the bed is frozen. Basal sliding involves the slip between a glacier and its unfrozen bed, facilitated by the presence of meltwater, which reduces frictional resistance. Subglacial deformation occurs when the glacier is decoupled from its bed and flows as underlying unfrozen sediments deform. This process is often associated with high pore water pressures within the sediment. All three of these mechanisms are thought to coexist under fast-flowing ice streams. **In Chapter 4, a one-dimensional model simulates sediment accumulation at the grounding line during glacial retreat, aiming to construct GZWs with geometries matching those observed in the geologic record of paleo-ice streams.** The model tests controls such as sediment flux and stoss angle to assess their impact on GZW geometry and the time required to construct these landforms under various conditions.

Chapter 2: Characterizing bed roughness on the Antarctic continental margin

Adapted from: **Munevar Garcia, S**., Miller, L.E., Falcini, F.A.M., and Stearns, L.A.: Characterizing bed roughness on the Antarctic continental margin, *Journal of Glaciology*, 1-12. https://doi.org/10.1017/jog.2023.88, **2023**.

2.1 Introduction

Approximately half of the Antarctic Ice Sheet (AIS) lies farther than 5 kilometers from any direct subglacial bed measurement (Morlighem et al., 2020). Interpolation techniques have been used to compensate for unresolved bed topography, but these can lead to the misrepresentation of terrain (MacKie et al., 2021). Moreover, existing topography products that rely on radio sounding systems often fail to identify deep subglacial troughs, which are critical in determining ice stream flow direction (Morlighem et al., 2020). The flow of ice streams is modulated by processes at the ice-bed interface (Stokes et al., 2007, 2018), but the extent to which subglacial topography promotes or inhibits ice flow remains uncertain (Favier et al*.,* 2014; Robel et al., 2022). This is due to the complex nature of processes at the ice-bed interface, which makes it difficult to accurately model ice-sheet behavior. The parameterization of basal traction in ice-sheet models is largely reliant on satellite-based observations of the ice-sheet surface (Arthern et al., 2015) and remains a considerable source of uncertainty (Ritz et al., 2015). The lack of direct and high-resolution (i.e., sub-kilometer) observations of subglacial topography limits our ability to separate skin drag and form drag components, often combined when defining basal traction (Kyrke-Smith et al., 2018). The skin drag component of basal friction is impacted by basal meltwater and properties of the uppermost layer of deformable sediments (Iverson and Zoet, 2015), which are not resolvable by topography (i.e., elevation) products. The form drag component, however, which describes the resistance to ice flow that originates as ice deforms around bed obstacles (Weertman, 1964), can be represented by bed roughness measurements. Sliding theories suggest that perturbations at the meter scale can generate enough basal drag to limit sliding (Weertman, 1957; Schoof, 2002; Robel et al., 2022). This is supported by the observation that form drag produced by subglacial roughness can produce significant shearing as grounded ice retreats over rugged topography (Hogan et al., 2020). Thus, the inclusion of high-resolution basal topography as a parameter is essential in producing realistic basal motion (Whillans and van der Veen, 1997; Winsborrow et al., 2010; Morlighem et al., 2020; Law et al., 2023). Bed roughness, defined here as "the extent to which terrain varies vertically over a given horizontal distance" (Rippin et al., 2014), is therefore a useful tool in determining the influence that bed topography exerts on ice flow velocities (Cooper et al., 2019; Law et al., 2023), though the range of scales at which bed roughness can be quantified is dependent on the spatial resolution of the elevation data.

Studies over large areas (>500 km^2) of the AIS use bed roughness derived from radio-echo sounding (RES) to investigate the impact of bed topography on basal processes (e.g. Taylor et al., 2004; Siegert et al., 2004, 2005; Bingham and Siegert, 2007, 2009; Rippin et al., 2006, 2011, 2014; Li et al., 2010). RES provides high along-track resolution, but the transect spacing often exceeds 10 km (Siegert et al., 2004; Bingham et al., 2007; Rippin et al., 2014), which is too wide to capture roughness associated with landform assemblages typical of paleo-ice stream beds (wavelengths between 10^1 and 10^2 m; Falcini et al., 2018). Results from early studies suggested that variations in bed roughness were spatially organized, where rough

beds were found in inland regions of slow-moving ice and smoother beds were found downstream in regions of fast-flowing ice streams (Siegert et al., 2004; Taylor et al., 2004; Bingham and Siegert, 2007). This implies a straightforward relationship where roughness is controlled by, or is a reflection of, ice-flow velocity and distance from the grounding line. However, more recent studies have shown that fast flow is not always associated with a smooth bed (Rippin et al., 2011; Schroeder et al., 2014; Falcini et al., 2018).

The degree to which bed roughness can identify bed lithology and subglacial bedforms remains underexplored, and the quantification of bed roughness at scales where individual landforms can be resolved has been largely underutilized as a tool to infer bed conditions in lieu of using ice-sheet surface inversions (Taylor et al., 2004; Bingham et al., 2017). While the orientation of elevation transects has been previously considered (Rippin et al., 2014; Bingham et al. 2017; Falcini et al. 2018, 2021; Cooper et al., 2019), not many studies have explored the impact that different elevation detrending scales have on bed roughness at small horizontal scales ($10^{1\text{-}2}$ m) where local topography is resolved. This is especially problematic as roughness analyses are inconsistently calculated, and are varied in roughness scales of interest across different studies (Smith et al., 2014).

The acquisition of bathymetric data over the deglaciated seafloor around Antarctica presents the opportunity to explore former subglacial bed conditions at higher resolutions and with greater spatial coverage than beneath contemporary ice streams. The seafloor of the Amundsen Sea Embayment (ASE) records the Last Glacial Maximum (LGM) and post-LGM glacial history of the formerly merged ice stream sourced from Pine Island Glacier (PIG) and Thwaites Glacier (TG) (Graham et al., 2016; Figure 2.1). During the Quaternary period, these glaciers excavated a trough extending over 500 km in length, while the ice sheet is believed to have reached the shelf edge (Graham et al., 2010). Seismic profiles along the trough indicate that the inner shelf, close to the modern grounding line, predominantly consists of crystalline bedrock, whereas the middle and outer shelf exhibit a younger and unlithified sedimentary substrate (Lowe and Anderson, 2002). On the inner shelf, streamlined bedforms are prevalent in areas of thin sediment cover, though some sediment-filled depressions are also observed near the modern ice shelf front (Figure 2.1B; Nitsche et al., 2013). Moving towards the middle shelf, the topography becomes more rugged, with shallow sills and a network of subglacial meltwater channels cutting into the bedrock (Figure 2.1C,D; Nitsche et al., 2013; Kirkham et al., 2019). The paleo-ice stream beds of PIG and TG converge in the middle shelf, where streamlined bedforms are abundant (Figure 2.1D; Graham et al., 2016). Further downstream from the convergence, drumlinized bedforms evolve into mega-scale glacial lineations (MSGLs) at the transition of crystalline bedrock to sedimentary substrate (Figure 2.1E; Wellner et al., 2001; Lowe and Anderson, 2002).

Recent gravity-derived bathymetry beneath the Thwaites ice shelf and ice tongue reveals similarly complex topography with relief comparable to the study sites located in the middle-shelf of Pine Island Bay (PIB; Jordan et al., 2020). Hogan et al. (2020) show that high-resolution bathymetry is necessary to capture the spatial variability of bed topography on the inner shelf just offshore of PIG and TG. These two glaciers were responsible for >30% of the annual discharge from the West Antarctic Ice Sheet (WAIS) between 2009 and 2017 (Rignot et al., 2019), and assessing the variability of bed topography and roughness offshore of these glaciers can provide an analog for the subglacial environment of contemporary glaciers and ice streams.

Through high-resolution bathymetry offshore of Pine Island and Thwaites glaciers, as well as the inclusion of elevation models derived from swath-radar underneath TG, this study compares bed roughness results between different methods, orientations, and detrending scales to determine the influence of each of these parameters on bed roughness results and the implications for ice behavior. We then compare results from high-resolution elevation models to the coarser BedMachine dataset to assess any potential roughness signatures that might be misrepresented when bed topography is not available at a high spatial resolution. The BedMachine dataset uses a mass conservation method and incorporates various data sources to fill data gaps and provide compatibility with numerical models (Morlighem et al., 2017, 2020). Lastly, we incorporate roughness results from bed topography data obtained from geostatistical simulations conducted on Jakobshavn Glacier by MacKie et al. (2021). This allows us to compare roughness statistics between direct observations in the ASE and stochastically simulated topography.

2.2 Methods

A total of six study sites were used for analysis where a compilation of multibeam echosounder bathymetry data in the eastern ASE was used to produce the gridded 50-m bathymetric dataset used for analysis of sites 1-4 (Figure 2.1A; Nitsche et al., 2013). Elevation data for the bed of TG (sites 5-6) comes from swath-radar published by Holschuh et al., 2020. The study sites were selected to assess the relationship between topography and the formerly expanded PIG-TG system during and following the LGM (Graham et al., 2010; Nitsche et al., 2013). The diverse set of glacial landforms across the sites allows us to assess and compare roughness values across different relief, bed slopes, and geologies. Topographic realizations used for statistical analysis are from simulations by MacKie et al., 2021 (Figure A2.1).

The site grids were drawn where there was continuous data coverage to ensure that missing data would not impact the roughness results. For each grid, transects oriented parallel and orthogonal to paleo-ice flow direction were inferred from streamlined subglacial landforms, such as grooves and glacial lineations (Figure 2.1B-G). Based on the width of streamlined features observed in the ASE, the spacing between transects was set to 500 m, which also corresponds to the spatial resolution of BedMachine Antarctica (Morlighem et al., 2020). Elevation values were extracted every 50 m along each transect, to match the horizontal resolution of multibeam bathymetry (Figure 2.2). To assess how the configuration of basins and channels may impact roughness measurements, we created a 500 m buffer around the subglacial channels mapped by Kirkham et al. (2019) that fell within our study sites in PIB. This buffer was used to compare the roughness values associated with subglacial channels to the roughness of the surrounding area. Once grids for all sites were constructed, a workflow to compare roughness results between different orientations, detrending techniques, and scales was implemented (Figure 2.3A). Elevation transects were detrended using two methods to remove long-wavelengths components (Taylor et al., 2004): 1) a linear detrend of the entire transect using least-squares regression to assess regional-scale topography and 2) subtracting the mean elevation of a 1.6-km moving window to match the minimum moving window used in the Fast Fourier Transform (FFT) analysis discussed below, which we use to characterize local, kilometer-scale topography. By quantifying roughness at both regional and local scales, we assess the sensitivity of roughness measurements to different detrending methods.

Roughness was calculated using a standard deviation (SD) method and a Fast Fourier Transform (FFT) method. The SD method provides a metric for the variation of amplitudes in elevation in a straightforward manner, which can be quickly applied to numerous transects with little computational power. SD is commonly used to measure roughness in the Earth Sciences (Smith, 2014), though it is unable to capture the horizontal frequency of undulations. Fourier transformations were introduced in some of the earliest studies on ice sliding over sinusoidal (i.e., idealized) topography, where it was proposed that bed roughness could be described in terms of the power spectrum of the bed elevation (Kamb, 1970; Nye, 1970). FFT analysis converts bed elevations into a wavelength spectrum to calculate the amplitude and the spatial frequency of undulations present in the bed; the methodology for the FFT calculations used in this analysis follows Li et al. (2010). We present a basal roughness index (ξ), which reflects the magnitude of vertical deviations in the bed and is calculated by taking the integral of the spectral power density, *S(k)*, over the moving window (Equation 1).

$$\xi = S(k)dk \qquad \text{Eqn. 2.1}$$

To perform FFT calculations, the convention is to use a minimum of n = 32 data points in each moving window (Taylor et al., 2004); therefore, given the 50-m horizontal resolution of the bathymetry data, a moving window of 1.6 km (50 m x 32) was used to calculate roughness. Both the SD and FFT methods were used to quantify roughness at the local (1.6 km) and regional (20-50 km) scales defined earlier using the two methods of elevation detrending.

To determine the impact of transect orientation on roughness measurements, the directionality of roughness was assessed by comparing parallel- ($R_{\parallel}$) and orthogonal-roughness ($R_{\perp}$) values where transects intersect. By implementing the anisotropy ratio introduced by Smith et al. (2006; Equation 2),

$$\Omega = \frac{R\parallel - R\perp}{R\parallel + R\perp} \qquad \text{Eqn. 2.2}$$

where R represents the roughness values obtained from the SD and FFT methods, the directionality of roughness values can be compared across sites and methods. Values approaching 1 suggest $R_{\parallel} >> R_{\perp}$ and values approaching -1 indicate $R_{\parallel} << R_{\perp}$, and where $\Omega = 0$, suggests an isotropic surface which can represent a smooth or truly random landscape (Falcini et al., 2021). Output results for the analysis are point data, which we use to interpolate and generate raster products containing roughness and anisotropy values.

The same conditions for the SD method were applied to the BedMachine dataset (Morlighem et al., 2017, 2020) to investigate where roughness values may be under- or over-estimated depending on the spatial resolution of the elevation raster used. Roughness results derived from high-resolution datasets were subtracted from BedMachine results to generate rasters showing where and by how much BedMachine results differ from the "true" roughness of resolvable landforms. We also applied the SD method to one of the 250 topographic realizations from MacKie et al. (2021) as well as the corresponding elevation dataset from Greenland BedMachine (Morlighem et al., 2017). The main channel is present in both elevation datasets (Figure A2.1), but the BedMachine dataset more closely resembles the average of all topographic realizations from MacKie et al., 2021. The outliers discussed in the results and discussion

sections are defined as roughness values exceeding +/- 1.5 * IQR / √n, where IQR is the interquartile range.

2.3 Results

At site 1, on the inner continental shelf closest to the contemporary Pine Island calving line (Figure 2.1B), roughness is relatively consistent at both the local and regional scales (10^1-10^2 m, 10^2 m^2) for both methods used. The lowest roughness measurements (<5 m) from the SD method are found where multichannel seismic data over the deepest water depths of 950-1050 m reveal a basin infilled with >300 m of unconsolidated sediments (Nitsche et al., 2013) with and without the presence of small-amplitude (<5 m) lineations (Figure 2.4A). High roughness values from the SD method (>30 m) are found on the slopes of streamlined landforms such as crag-and-tails and whaleback ridges that taper in the direction of paleo-ice flow, previously identified by Nitsche et al. (2013). Other high roughness values (20-30m) are found within the channel buffer particularly in the orthogonal orientation, where the mean roughness of the channel buffer is 5 m greater than the mean of the site (Table A2.1). Roughness values of 45-60 m are found where channels have a cross sectional area >35,000 m^2 as mapped by Kirkham et al. (2019) and where relief between channel thalweg and surrounding bedrock is >250m. While the spatial pattern for FFT results is similar to the SD method, areas of extreme relief in the orthogonal orientation create outliers (>7,000 m^2) that are over two orders of magnitude greater than the median (72 m^2; Table A2.2). Roughness ranges and medians for all transects in the parallel orientation are consistently lower than the orthogonal transects for both spatial scales and roughness calculation methods (Figures 2.5, A2.2A, Table A2.2).

Downstream (i.e., seaward) of site 1, exposed crystalline bedrock at site 2 becomes more prevalent and streamlined landforms are less common. The topography is rugged with water depths between 500 and 1500 m and several deeply incised channels (Figure 2.1C). The upstream section of site 2 is characterized by parallel crag-and-tails and drumlins (Nitsche et al., 2013), while a deep basin floored by streamlined landforms is located downstream and is flanked by steep slopes (Figure 2.1C). The magnitude of median roughness for site 2 is nearly double that of site 1 when using the SD method and nearly three times higher in the parallel orientation. When using the FFT method, the medians for site 2 increased by a factor of 5 and 12 for the orthogonal and parallel orientations respectively (Figure 2.5, Table A2.2). High outliers (>60 m) from the SD method are concentrated along the length of the walls flanking channels inferred as subglacial in origin and with a cross sectional area >35,000 m^2. Conversely, the lowest values (<8 m) are present in areas of shallow topography on top of bedrock highs and in deep areas identified by Kirkham et al. (2019) as relict subglacial lakes, where no glacial landforms are observed. The FFT method produced high roughness values, but they were not as widespread as those produced by the SD method. Instead, outliers (>6,000 m^2) are found in areas where the relief associated with subglacial meltwater channels is greater than 250 m (Figures 2.4B, A2.2B).

Site 3, where the paleo-ice streams of Pine Island and Thwaites glaciers merged during the LGM (Larter et al., 2014), has the greatest relief among the sites studied, with water depths between 375 and 1650 m, dominated by deep basins that are up to 300 m below the surrounding seafloor (Nitsche et al., 2013) and a central flat topographic high. The steep slopes at the edges of the basin and the large meltwater channels that connect them generate the highest roughness values across all sites, particularly at the regional scale where values are 2-3 times greater than at

the local scale (Table A2.1, A2.2). These channels are mostly found in the upstream region of site 3, have a cross sectional area >35,000 m^2 and have SD roughness values of 30-80 m. Conversely, the streamlined seafloor of the central topographic high, which is cross-cut by geological structures (Graham et al., 2016), records the lowest roughness values of this site in all methods, orientations, and scales. Similar to site 2, outliers in the SD-based roughness are located along the walls of the deep basins, while FFT-based roughness outliers are spatially isolated (Figures 2.4C, A2.2C).

Site 4 has gentle relief and marks the transition between exposed crystalline bedrock in the middle-shelf to an unlithified sedimentary substrate in the outer-shelf (Wellner et al., 2001; Lowe and Anderson, 2002). Drumlinized bedforms are absent downstream of the transition, and the landscape in this site is dominated by MSGLs, which are not observed in any of the other sites in the ASE. Site 4 has the lowest median roughness values of all sites (Table A2.2), and the high roughness values in site 4 coincide with the presence of drumlinized features in the upstream region. These SD values are comparable in magnitude to the ones produced by the low-amplitude streamlined landforms found in sites 1 and 3 at the local scale (10-30 m). The lowest roughness values across all sites are found in the downstream region of site 4 (<1 m), where unconsolidated sediments blanket the sea floor and relief is minimal (Figures 2.4D, A2.2D). These roughness values are comparable to the ones seen in the sediment-filled basin present in site 1.

Sites 5 and 6 are located in the subglacial environment of TG and are comprised of MSGLs and crag-and-tails similar to those found in sites 1 and 4. The upstream region of site 5 is dominated by elongated bedforms thought to be the tails of crag-and-tails (Alley et al., 2021) which transition into bedrock protrusions downstream (Figure 2.1F**)**. At the local scale, high roughness values (>30 m) are found where these protrusions generate relief and where MSGLs terminate in moats, as described by Holschuh et al. (2020). Low roughness values are present in the sedimentary basin where MSGLs are present, particularly in the parallel orientation (Figure A2.3A). Site 6 is dominated by large bedrock protrusions or ridges, with lineations present upstream and downstream from said ridges. High roughness values (>30 m) are concentrated where the ridges generate relief (<300 m) in both orientations and in the stoss side of the crag-and-tails present downstream of the topographic high. Low roughness values (<5 m) are found where lineations are present in areas of low elevation (Figures 2.1G, A2.3).

Roughness results obtained from the topographic simulations conducted by Mackie et al. (2021) exhibit similar patterns to those observed in our study sites: roughness is higher in the orthogonal orientation and at the regional scale (Figure A2.4). When comparing a single realization to the average of all realizations, the former displayed higher roughness values and had higher mean values than any of our study sites, regardless of scale. Meanwhile, the mean value derived from the average of all topographic realizations, aligns closely with our study sites at both scales. The topographic realizations are dominated by a 70 km-long, 4 km-wide, slightly meandering channel oriented in the direction of ice flow. Roughness measurements from the local scale are insufficient to capture the roughness signature generated by the wide channel. Nevertheless, local-scale roughness measurements still indicate values as high as 180 m, exceeding the maximum roughness observed in our study sites at that scale (Figures 2.4, 2.5). In contrast, the regional scale is capable of encompassing the entire channel width, offering a more comprehensive depiction of the roughness associated with the channel. Roughness values at the regional scale can reach up to 450 m, significantly exceeding the maximum value of 295 m observed in our study sites at the same scale. The average of all realizations also exhibits

significant roughness associated with the channel, albeit to a lesser extent (375 m). However, it is important to note that this approach introduces artifacts that create spikes in roughness values and generates smoother terrain outside the channel, potentially obscuring the presence of other smaller tributaries (Mackie et al., 2021).

2.4 Discussion

2.4.1 Impact of methodology employed

The spatial distribution of high and low roughness measurements remains largely consistent between the SD and FFT methods across all sites, similar to results presented by Falcini et al. (2018). Yet, there are important differences when comparing the effectiveness of detrending methods in capturing regional and local roughness (Figures 2.4, 2.5, A2.2). Both the FFT and SD methods yield right-skewed roughness distributions, meaning most roughness values are on the lower end, with a few larger values on the higher side. Notably, in the context of this analysis, we specifically consider high outliers. The FFT method produces more outliers due to the significantly greater magnitude and range of roughness values (Figure 2.5B, Table A2.2), as previously noted by Rippin et al. (2014). On average, the percentage of data points considered outliers is higher for the FFT method (11%) than for the SD method (5.8%). The number of outliers in the FFT method remains relatively constant across the two detrending scales considered (0.2% change), while the number of outliers in the SD method increases by an average of 19% when using the regional detrend (i.e., detrending across the whole elevation profile) compared to the local detrend of 1.6 km. The increase in outliers when using the SD method is particularly noticeable at sites 1-3, which have high relief and exposed crystalline bedrock (Lowe and Anderson, 2002). However, at site 4, the most downstream site in the ASE, where gentle relief and streamlining of soft sediments are observed (Figure 2.2G-H), the number of outliers decreases by 17.5%. Contrary to the expectation that using a regional detrend would increase roughness variability, large depositional environments typically found at the downstream ends of paleo-ice stream beds, may exhibit decreased variability and roughness signatures may be dominated by sediment accumulation and drowning of antecedent topography.

While the spatial distribution of roughness values is similar between the local and regional scales across all sites, the regional scale exhibits greater magnitude (Figure 2.5), due to the nature of the detrending method, where the range of detrended elevations is considerably greater (Figure 2.3B). The local scale effectively provides roughness characterization for smaller-scale (<1.6 km) features and the regional scale considers larger features (i.e. deep basins and meltwater channels) while still removing long-wavelength trends. The choice of scale for detrending and the moving window used to calculate roughness has a direct impact on roughness results. As such, their interpretation requires careful consideration and should not be directly compared with studies that use different scales (Smith, 2014). When comparing results between the two different scales, we found that the spatial distribution of high roughness values showed minimal variation when the FFT method was used. Specifically, when the regional detrend was applied, the average median roughness increased by 14% with the FFT method, compared to a 64% increase using the SD method. The increase in outliers observed with the SD method when the regional detrend was applied coincides with a more widespread distribution of high roughness values across all sites (Figures 2.4, A2.2). The SD method detected a greater spatial coverage of high roughness values than the FFT method.

Ultimately, the FFT method is less susceptible, but still impacted, by the scale used to calculate roughness. Although the SD method is more susceptible to the scale used, it can detect roughness at local scales more effectively than the FFT method. Using the SD method on the local scale, high roughness values are typically observed along the length or width of a specific landform, whereas on a regional scale, high roughness values tend to extend beyond landform boundaries and encompass landform assemblages (Figures 2.4, A2.2). The FFT method yields similar spatial distributions of high roughness values at both scales, making the distinction less clear. The size of the moving window used to detrend elevation profiles was ultimately dependent on the spatial resolution of the elevation products available, the method employed, and the size of landforms present within the study area. Importantly, the SD method is not limited by the 32 sample points required for FFT analysis and can be implemented over even smaller windows. Although the SD method can quantify roughness using a smaller moving window, we opted to use a 1.6 km window in order to make direct comparisons between the SD and FFT methods. Since bathymetric datasets are available for various sectors of Antarctica at a spatial resolution of 50m or finer, the 1.6 km moving window used in this study can be used as a local scale to compare SD and FFT methods in other deglaciated regions. However, the SD method may be preferred due to its ease of use and ability to detect roughness patterns at scales smaller than 1.6 km without the extreme variation in results associated with the FFT method. To ensure comparability, it is crucial that roughness studies report the scale used to detrend elevation profiles, and the moving window used to calculate roughness, and keep these consistent across study areas, when possible.

2.4.2 Anisotropy Measurements

Measurements across all sites reveal that mean roughness values in the orthogonal orientation are higher than those in the along-flow orientation across all sites, scales, and methods (Figures 2.4, 2.5). This pattern is expected because landforms constructed in the subglacial environment will be preferentially oriented in the along-flow orientation, with the resulting changes in landform amplitude yielding higher roughness in the orthogonal orientation as demonstrated by earlier roughness studies (Rippin et al., 2014; Bingham et al., 2017; Falcini et al., 2018, 2022; Cooper et al., 2019). On average, the anisotropy ratio was higher when the local scale was used, especially in sites 1 and 4, where small-scale streamlined landforms are abundant (Figure 2.1B,E) and their topographic variability is better represented in smaller moving windows. The heavily skewed distribution of roughness values for the FFT method described earlier is also observed here, as the mean anisotropy ratio is 77% higher than the mean ratio from the SD method (Figure 2.6, Table 2.1). Since the SD method is unit preserving, and deemed an appropriate measure for directionality analysis (Rippin et al., 2014; Falcini et al., 2021), only the anisotropy ratio from the SD method will be described henceforth.

Sites 1 (Figure 2.6A) and 4, where drumlinoid features and MSGLs dominate, are the most anisotropic landscapes, with a mean anisotropy ratio of -0.27 for the two sites. The high anisotropy values observed in site 4, downstream of the convergence between PIG and TG, support the idea that the increased flow velocity resulting from the convergence led to landforms with higher elongation ratios (Nitsche et al., 2013), which correspond to more anisotropic landscapes. A similar value for an area dominated by MSGLs is reported by Falcini et al. (2022), though it is important to note that the window size used in their analysis differs from ours and, therefore, results between the studies are not directly comparable. Also worth noting is that

artifacts present over the MSGLs in the bathymetry of site 4 bring the overall anisotropy ratio closer to zero by introducing roughness noise in the parallel orientation (Figure 2.4D).

While the presence of meltwater channels creates a more rugged topography at site 2 (Figure 2.1C), the orientation of streamlined landforms observed is fairly consistent and yields an average anisotropy ratio of -0.13. Alternatively, the mean anisotropy ratio for site 3, approaches zero (-0.05) in both scales and methods used (Figure 2.6B). The isotropic nature of this site can be attributed to several factors, including the irregular alignment of streamlined landforms and a flat topographic high where the Pine Island and Thwaites paleo-ice streams merged (Figure 2.1D). The presence of large sinuous meltwater channels, thought to have formed by pressurized subglacial meltwater (Lowe and Anderson, 2002; Nitsche et al., 2013), typically lead to random or isotropic landscapes. Alternatively, we observe anisotropic patterns where the lack of channels suggest a dry bed, allowing glacial sedimentary processes to take place. In such areas, it is possible to identify landforms, such as glacial lineations, irrespective of the method or scale used. This highlights the usefulness of this approach for determining patterns of streaming ice flow.

A distinct decrease in roughness values is evident following the transition from crystalline bedrock to sedimentary strata. This change in roughness, coupled with the subsequent increase in anisotropy downstream, attributed to the presence of MSGLs, enables the identification of geological variation with the ASE.

2.4.3 Comparisons with BedMachine

As widely used elevation products in ice-sheet models, we evaluate the performance of BedMachine Antarctica in the ASE, and underneath TG, as well as BedMachine Greenland at Jakobshavn Glacier. We specifically assess the impact of using a coarser resolution dataset on the accuracy of roughness results compared to high resolution data. While BedMachine is a downsampled version of the high-resolution bathymetry used in this analysis, its lower spatial resolution limits its ability to account for roughness derived from small-scale landforms (<500 m in Antarctica and <150 m in Greenland), resulting in misrepresentation of roughness values across all sites. The biggest discrepancies in roughness occur at the local scale, particularly in areas of sharp relief, like the stoss- and lee-sides of streamlined landforms, the steep walls flanking meltwater channels, and where multiple landforms are in close proximity (Figure 2.7, A2.5). The misrepresentation of SD roughness is as high as 150 m around deep meltwater channels and is more evident in the inner- and middle-shelf of PIB where relief is greater than in sites 5 and 6 underneath TG. In sites 1-4, the mean roughness differences between elevation datasets are relatively small, with an average of 0.7 m. Differences are higher in sites 5 and 6 at 8.7 and 3.9 m, respectively (Table A2.2). In contrast, areas of low relief, such as the sediment-filled basin in site 1, the flat topographic high in site 3, and where MSGLs are present in sites 5-6 show good agreement in roughness values between the two elevation datasets used. The average difference of 32.4 m in SD roughness between BedMachine Greenland and the topographic simulation from Mackie et al., 2021 is much greater than what we observe in the ASE, with SD roughness being underestimated by as much as 300 m in the walls of the main channel (Figure S5, Table S3). Indicating that the interpolation used to generate elevation datasets from radar measurements along limited track lines results in greater roughness discrepancies, compared to downsampled versions of 2D bathymetric sets.

The directionality of roughness is not captured by BedMachine, as evidenced by the noisy distribution of anisotropy values (Figure A2.6). Mean anisotropy values for the ASE sites are closer to zero (Table 2.1), indicating that BedMachine cannot accurately capture the anisotropy of these sites and thus misses roughness deviations in different orientations. Furthermore, while site 3 is in fact isotropic, the anisotropy ratio derived from BedMachine in site 4 is close to zero, despite it being the most anisotropic site of all. These discrepancies highlight the limitations of BedMachine in capturing MSGLs in soft sediments and providing insights into basal ice-sheet flow and organization. The similarity in mean roughness values in sites 1-4, despite the coarser resolution of BedMachine, can be explained by the use of a downsampled version of the ASE bathymetry being incorporated into the International Bathymetric Chart of the Southern Ocean (IBCSO), which was used in the creation of the BedMachine dataset. While the average roughness difference between the bathymetry and BedMachine elevation datasets in the ASE is minimal, there are notable discrepancies around key features known to influence ice dynamics. As a result, BedMachine fails to capture the roughness signature of features that are important in determining basal conditions. The elevation datasets for sites 5 and 6 are not included in BedMachine, therefore any roughness measurements derived from BedMachine, or any other continent-wide elevation dataset, in the modern subglacial environment are subject to interpolation, leading to smooth and unrealistic topography at the scales considered (MacKie et al., 2021). We do not draw any geomorphic interpretations from the results derived from BedMachine, but instead, we highlight the limitations that arise when an elevation dataset fails to resolve landforms that are useful for constraining ice dynamics (Greenwood et al., 2021).

2.4.4 Subglacial conditions inferred from bed roughness

Work by Siegert et al. (2005) established that subglacial bed roughness is dependent on four factors: (1) the direction of ice flow, (2) ice dynamics, (3) lithology, and (4) geological structure. Transect orientation with respect to ice-flow proved to be one of the biggest controls in roughness results across all sites tested in the paleo-ice stream bed of PIG and TG. Glacial sedimentary processes (erosion and/or deposition) play a crucial role in modulating topography in the along-flow orientation. These processes contribute to the creation and modification of landforms that exhibit a distinct alignment with the direction of ice flow. These patterns of preferential alignment reflect the cumulative effects of multiple glaciation cycles known to have taken place in the ASE (Graham et al., 2016), and highlight the significant role of glacial sedimentary processes in shaping the landscape.

Low roughness values (<10 m) are observed in regions of observed sediment cover in sites 1 and 4, as well as on top of the topographic high in site 3, where the two paleo-ice streams merged (Figure 2.4). This finding highlights that low roughness does not always signify the presence of thick sediment cover and bed lithology cannot be inferred from roughness alone. Consequently, low roughness values can imply two different lithologies. Firstly, it can indicate the presence of unconsolidated sediment, which reduces basal shear stress and facilitates ice flow. Alternatively, low roughness can also indicate exposed crystalline bedrock, where ice dynamics over such a hard substrate would suggest increased basal shear stress and slow ice flow (Bell et al., 1998; Wellner et al., 2001). Despite this, the presence of widespread grooves around the topographic high indicates efficient erosion (Bennet and Glasser, 1996; Nitsche et al., 2013), suggesting the merging of the paleo-ice streams was enough to overcome the basal shear stress

and erode the bedrock to create a smooth terrain. In this case, the increase in ice flow velocity is attributed to the merging of the ice streams, rather than the transition from crystalline bedrock to a sedimentary substrate further downstream. The merging of the ice streams, combined with the network of subglacial meltwater channels upstream, would have increased the supply of basal meltwater, reducing skin drag and facilitating ice flow. The association of low roughness values with both fast and slow ice flow suggests that skin drag, particularly influenced by the availability of basal meltwater in this context, exerts a direct influence on ice dynamics. These observations suggest that form drag alone should not be a key determinant in the sliding law, emphasizing the importance of understanding the complex interaction between basal meltwater, sediment properties, and ice flow behavior.

The boundary of geological structures, such as bedrock protrusions in site 1 (Figure 2.4A), subglacial meltwater channels in sites 2 and 3 (Figure 2.4B,C) and the boundary between crystalline bedrock and unconsolidated sediments in site 4 (Figure 2.4D) all cause a roughness spike and change in anisotropy in both methods and scales tested (Figure 2.6). The complex topography of PIB suggests two possible explanations for these roughness spikes. First, the increase in basal shear stress associated with rugged topography and the presence of bedforms is reflected in the increase of roughness values. Second, roughness spikes of even greater magnitude are predominantly associated with the presence of subglacial meltwater channels. These large channels would have lubricated the bed in certain instances (Nitsche et al., 2013), resulting in enhanced ice flow rather than increased basal shear stress. The formation of these channels is believed to be linked to episodic outburst floods from subglacial lakes during previous glacial periods (Kirkham et al., 2019). It is inferred that the largest and deepest channels likely developed over multiple glaciation cycles and required abundant meltwater. Specifically, the highest roughness values observed in PIB can be attributed to large episodic drainage events and it is likely that these channels increased in size progressively, leading to increases in elevated roughness values.

Roughness analysis from swath radar data show similarities between the geologies of sites 1-4 in PIB and sites 5-6 underneath TG. The widespread streamlining observed in the bed underneath TG, and their associated SD roughness values (<5 m) are analogous to the thick sediment pockets present in site 1 and the MSGLs present in site 4. The elongated bedforms observed in site 5, described as the tails of crag-and-tails (Alley et al., 2021; Figure 2.1F) exhibit the same geomorphic characteristics as the crag-and-tails present in PIB at the transition between crystalline bedrock and unconsolidated sediment (Graham et al., 2016; Figure 2.1E). In the parallel orientation, both sets of crag-and-tails have comparable SD roughness values. Upstream, the bedrock knobs exhibit roughness values of 20-25 m, whereas their downstream soft till tails display values of less than 5 m. Underneath TG, these tails have larger amplitudes (50-100 m) than the MSGLs offshore at site 4 (5-25 m). As a result, orthogonal roughness values for these features are 20-25 m greater than their PIB counterparts. Notably, the MSGLs in PIB have been in an open marine environment for at least ca. 10 cal. ka BP (Hillenbrand et al., 2013), where post-glacial sedimentation might have reduced their amplitude.

2.5 Conclusion

We quantified bed roughness at six different sites: four deglaciated sites offshore of Pine Island and Thwaites glaciers and two glaciated sites underneath contemporary Thwaites Glacier. By measuring roughness in different orientations relative to ice-flow, using different methods

and elevation datasets, and applying different detrending scales, we assess how various parameters influence roughness results. Transects in the orthogonal orientation consistently yield higher roughness values, the trends of which are obscured when using lower-resolution elevation products. The choice of scale at which roughness is assessed has a significant impact on the resulting roughness values and therefore requires careful consideration. Overall, the SD method provides a robust representation of bed roughness in several ways. The results obtained from the SD method accurately identify spatial patterns of roughness and anisotropy indicative of ice streaming. Additionally, the unit-preserving nature of the SD method allows for more reliable comparisons between different scales and locations, making it a useful tool for assessing bed roughness in deglaciated environments. The limitations of low-resolution topography are more apparent in the sites underneath contemporary Thwaites Glacier, compared to sites in PIB, suggesting that interpretations derived from bed roughness at ice-stream beds may not be entirely reliable and these uncertainties must be considered in any modeling work.

Table 2.1. Mean anisotropy from bathymetry and BedMachine (BM).

	SD		FFT		SD (BM)		FFT (BM)	
Site	Local	Regional	Local	Regional	Local	Regional	Local	Regional
1	-0.3	-0.25	-0.44	-0.42	-0.12	-0.13	-0.16	-0.14
2	-0.16	-0.1	-0.27	-0.24	-0.05	-0.05	-0.1	-0.08
3	-0.05	-0.02	-0.06	-0.05	-0.02	0	-0.01	0
4	-0.3	-0.18	-0.47	-0.45	0	0.02	0.02	-0.02

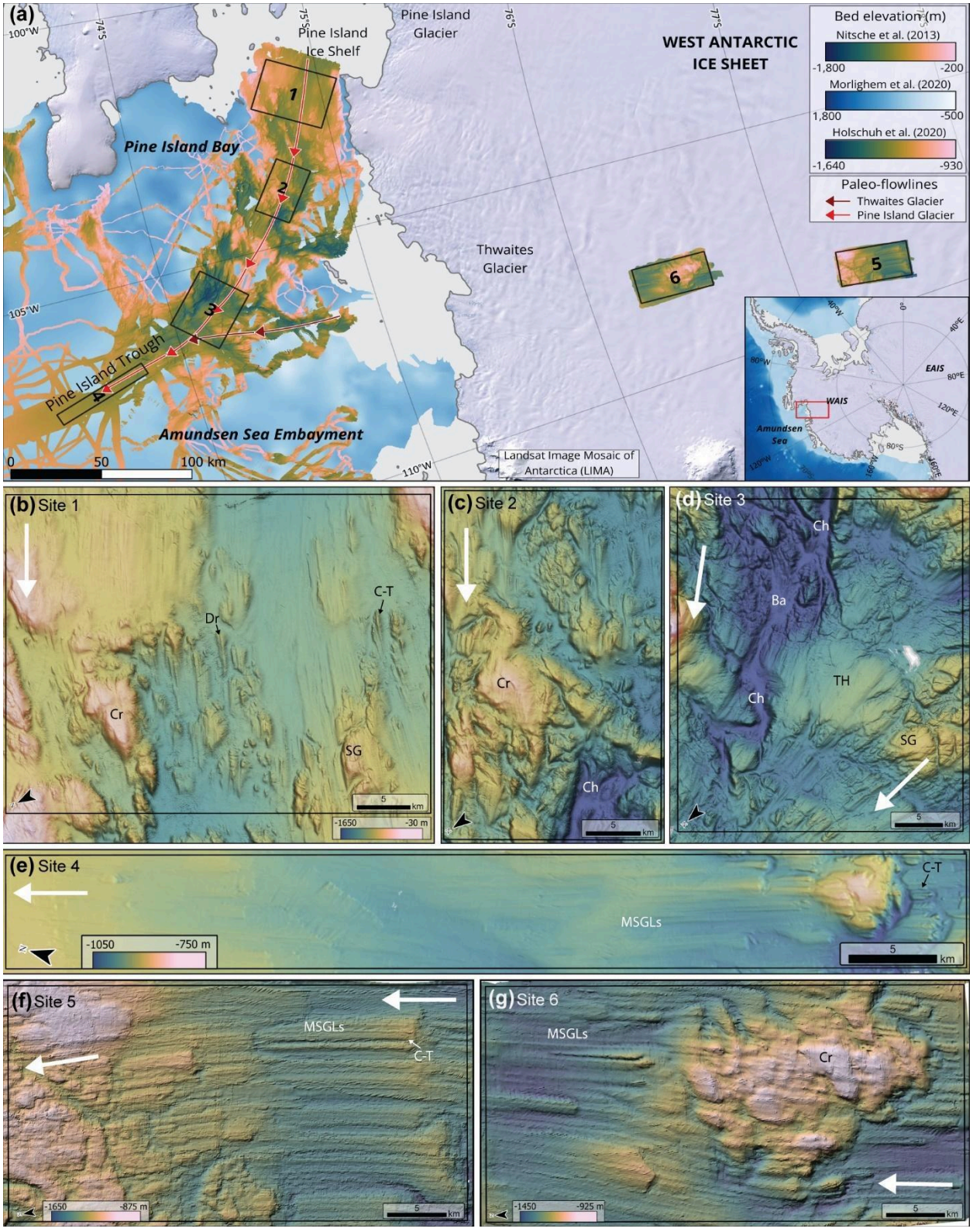

Figure 2.1. (A) Study sites in the Eastern Amundsen Sea and Thwaites Glacier marked by the black, numbered boxes. Arrows show the general direction of paleo-ice-flow for Pine Island and

Thwaites glaciers, which merged at site 3. **(B-E)** Multibeam bathymetry of sites in the Eastern Amundsen Sea. Grid cell sizes 35-50m, from Nitsche et al. (2013). **(B)** Ice-shelf proximal site consists of crystalline bedrock (Cr) mixed with deep pockets of unconsolidated sediment and linear bedforms, i.e. streamlined grooves (SG), crag-and-tails (C-T), and drumlinoid features (Dr). **(C)** Inner shelf site displaying crystalline bedrock, rugged topography, and sinuous channels (Ch). Color ramp as for **(B)**. **(D)** Site where the Pine Island and Thwaites paleo-ice streams merged, resulting in a change in ice flow direction. Presence of deep basins (Ba) and channels, a flat topographic high (TH), and grooved crystalline bedrock (SG). Color ramp as for **(B)**. **(E)** Transition between crystalline bedrock and unconsolidated sediment. **(F-G)** Swath-radar data from Holschuh and others (2020). **(F)** Upstream site of the Thwaites bed with MSGLs and bedrock protrusions at shallower depths. **(G)** Downstream site with streamlining and crag-and-tails either side of large exposed bedrock.

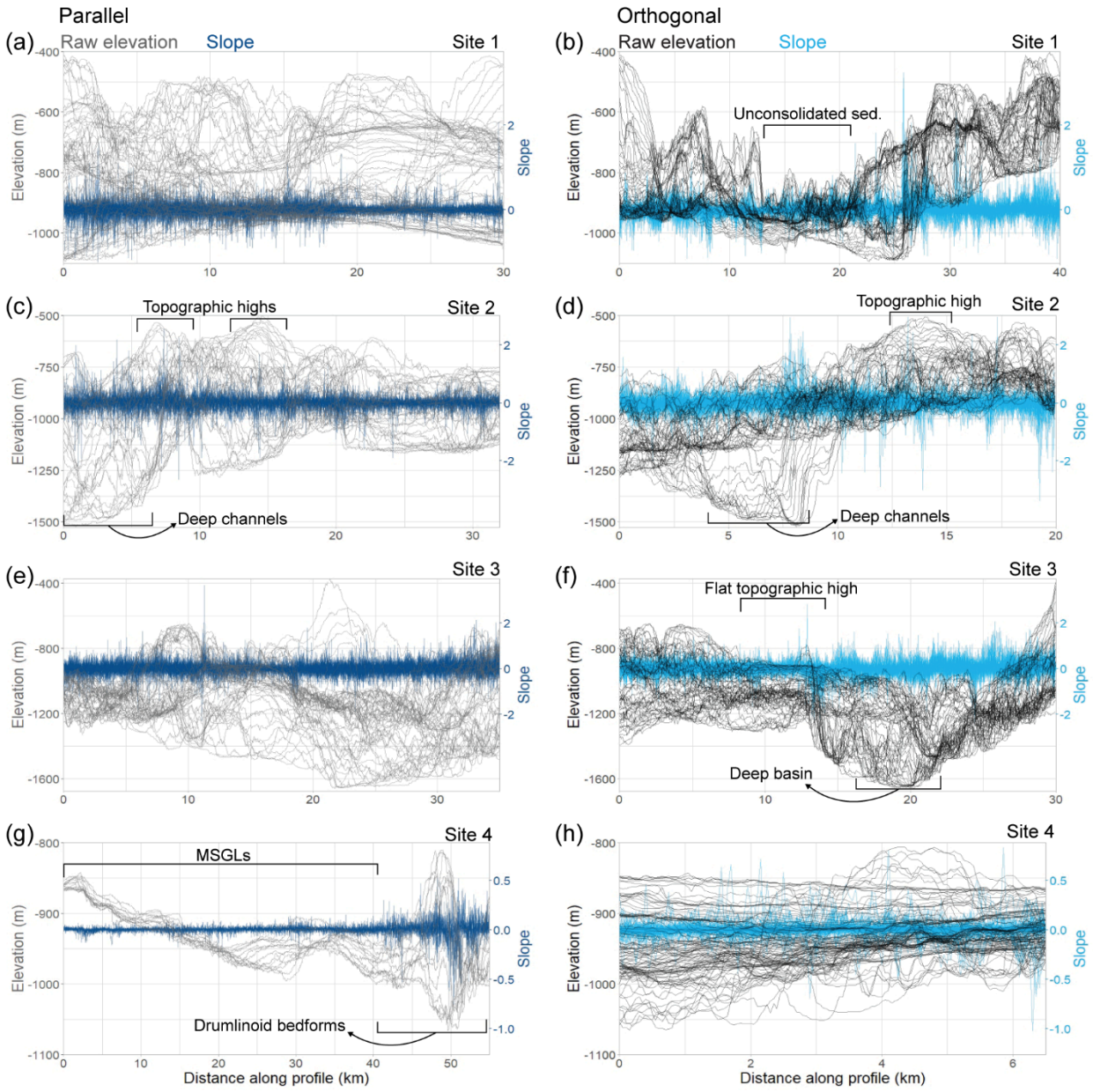

Figure 2.2. Raw elevation transects and calculated slope transects, both of which have data points at 50-m increments for East Amundsen Sea sites. Left and right columns show transects in the parallel and orthogonal orientations relative to paleo-ice flow direction, respectively. Slope is calculated as the dimensionless ratio of the vertical to horizontal change at every 50-m increment.

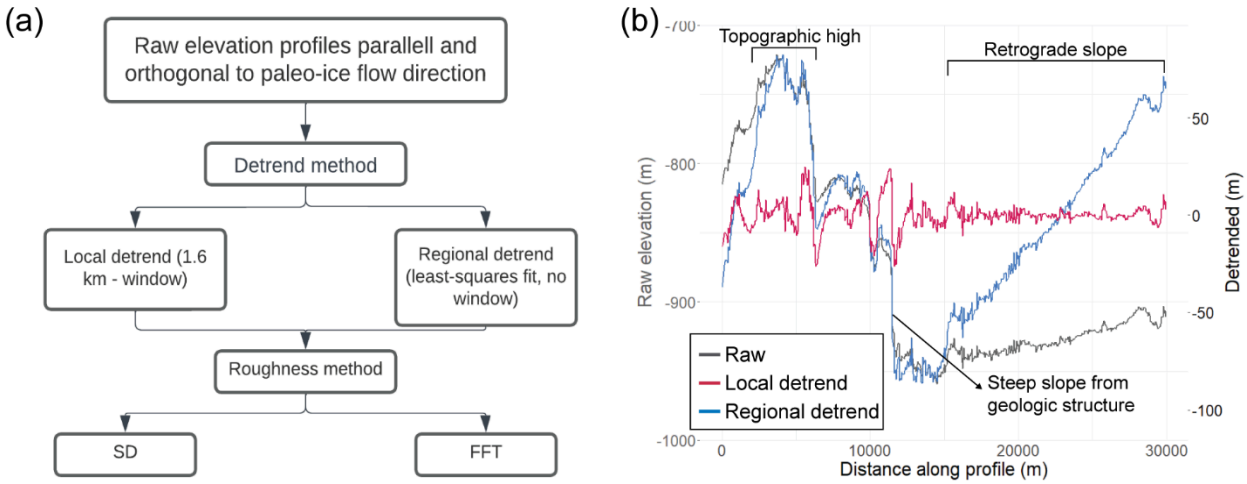

Figure 2.3. (A) Flow chart outlining the steps taken to calculate roughness using the SD and FFT methods described in the Methods section. **(B)** Example of a single raw elevation profile and corresponding detrended profiles using a local (red) and regional (blue) detrend method. Profile comes from Figure 2.2A.

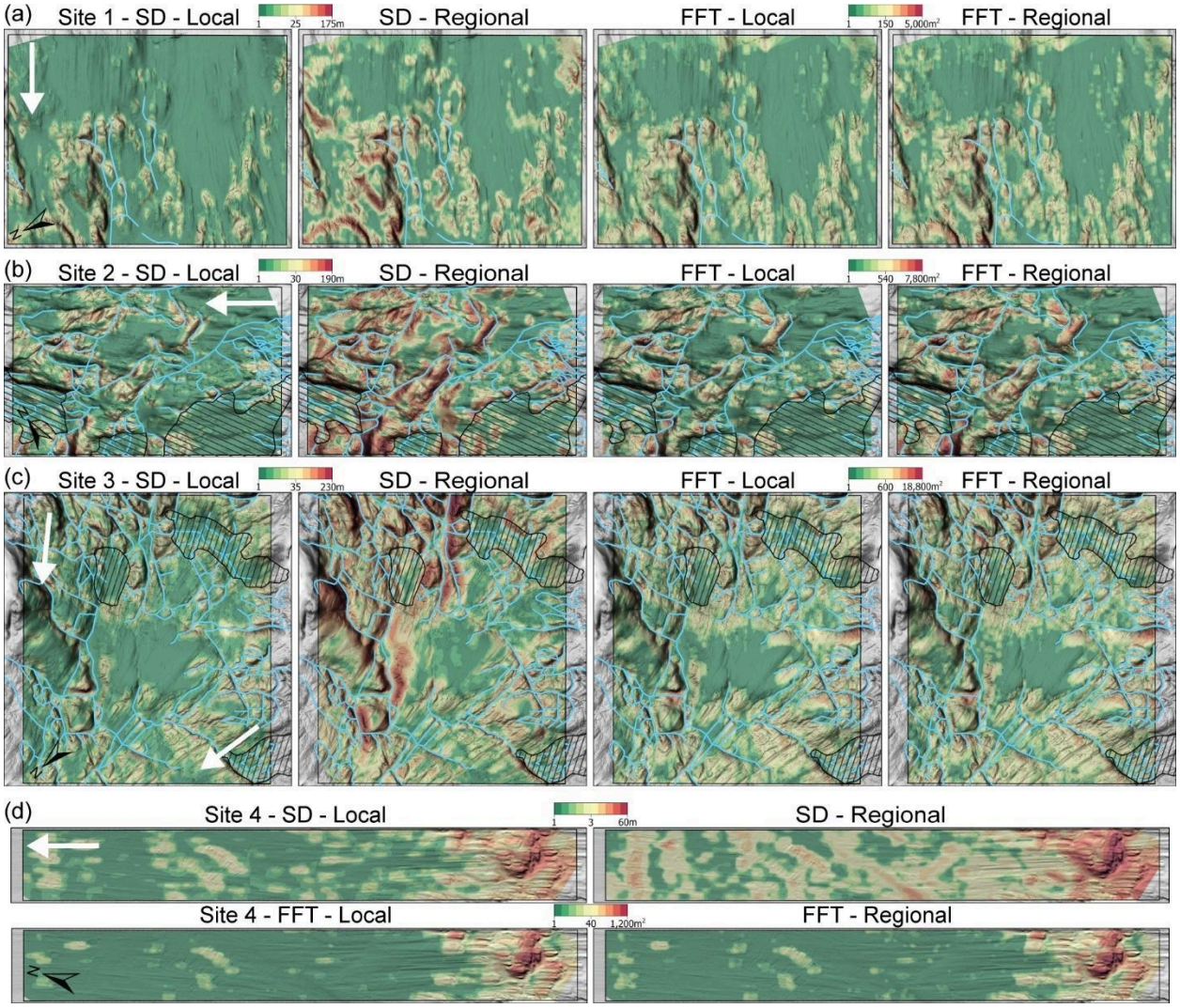

Figure 2.4. Absolute roughness measurements for parallel transects in sites 1-4 in the Eastern Amundsen Sea showing the difference in spatial distribution between scales and methods. Blue lines are subglacial meltwater channels and black, hatched polygons are relict subglacial lakes (Kirkham et al., 2019). White arrows indicate direction of paleo-ice flow.

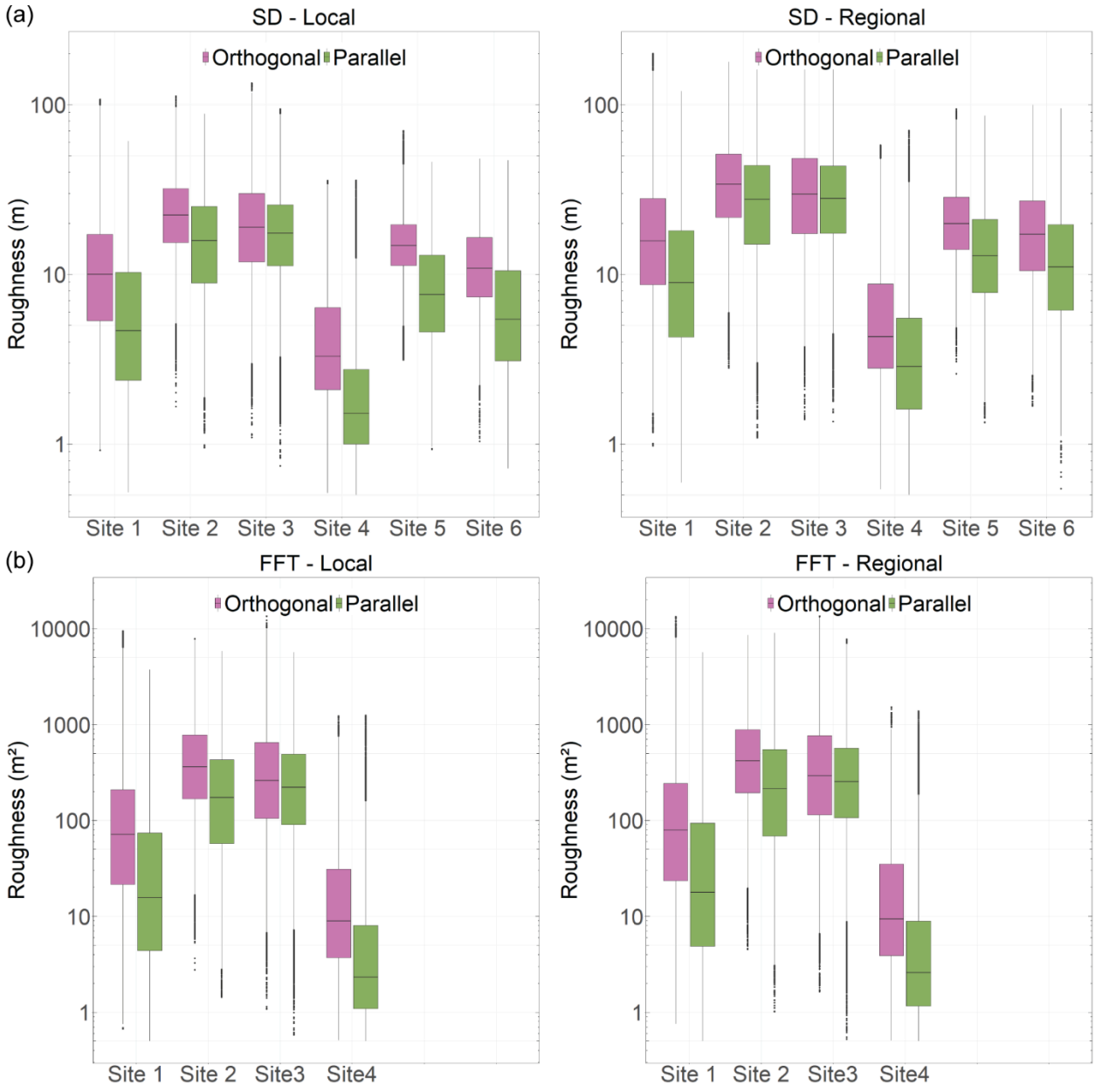

Figure 2.5. Distribution of the basal roughness parameter (ξ), employing a 1.6-km moving window across all sites. The boxes represent value points between the first and third quartiles (IQR), and the black horizontal bars indicate the median. Individual outliers are plotted where values exceed +/- 1.5 * IQR / √n **(A)** Distribution of values employing the SD method. **(B)** Distribution of values employing the FFT method, only applied to sites 1-4. Note use of logarithmic scale on the y-axis.

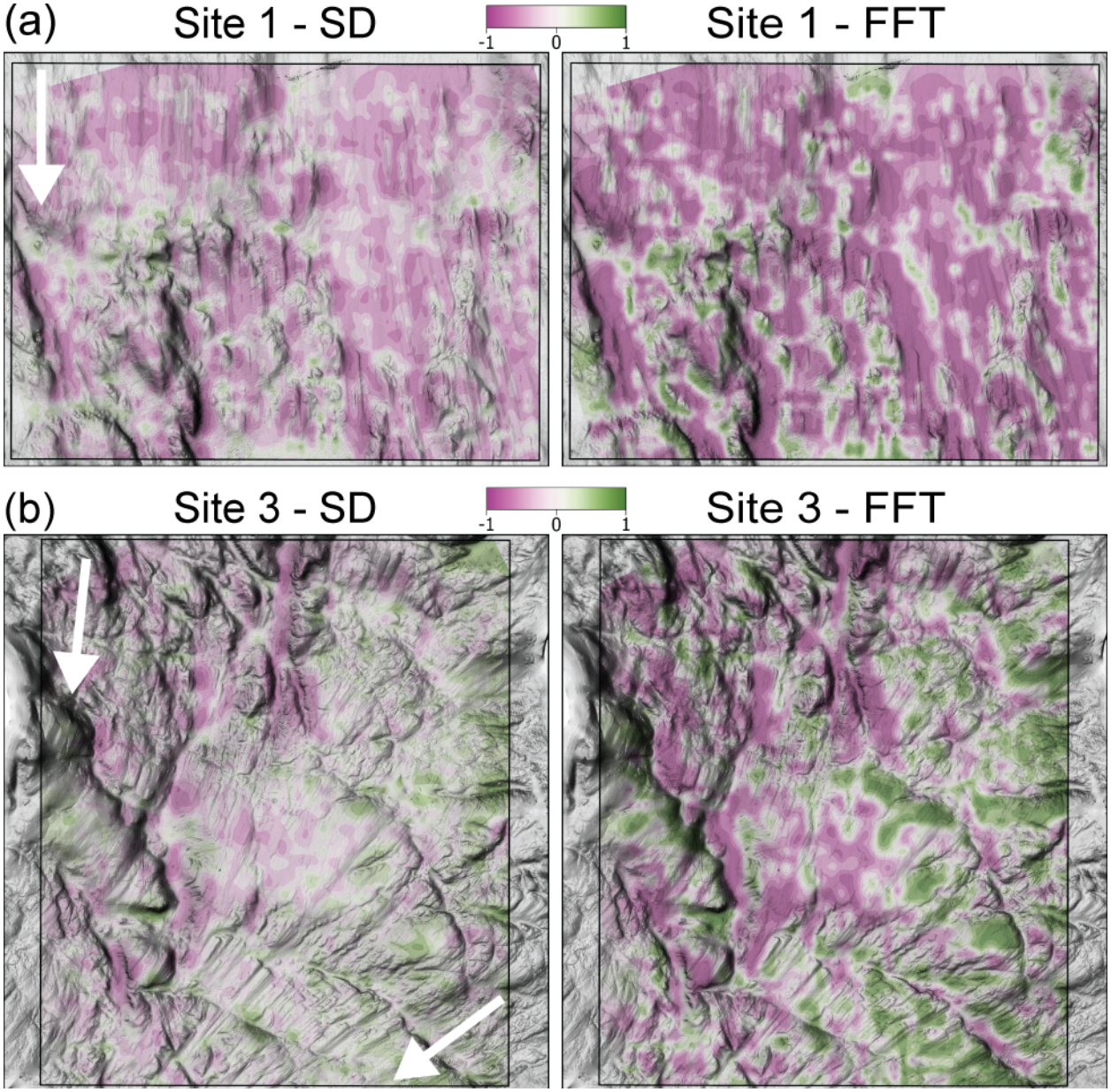

Figure 2.6. Anisotropy values calculated at every intersection point between parallel and orthogonal transects at sites 1 **(A)** and 3 **(B)** represent directionality of roughness measurements at the local scale. Orthogonal roughness dominates in the purple shades, parallel dominates in the green. White/gray shades indicate isotropic or random surfaces. White arrows indicate direction of paleo-ice flow.

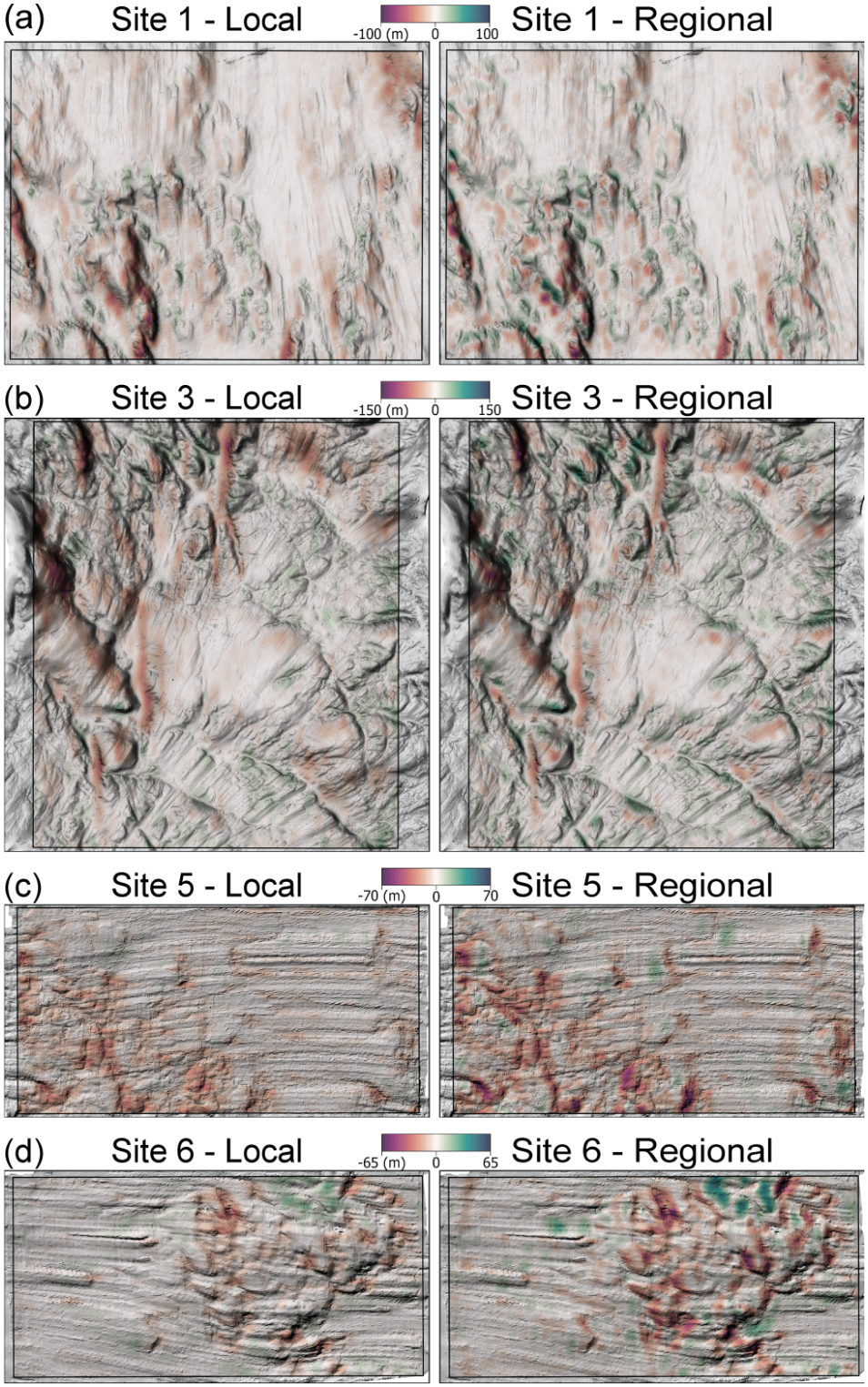

Figure 2.7. Difference in roughness measurements of parallel transects between high-resolution topography and BedMachine, showing where BedMachine under- and over-estimates roughness (red and green shades, respectively). Roughness for sites 1 and 3 **(A,B)** is derived from bathymetry; sites 5 and 6 **(C,D)** is from swath-radar (Holschuh et al., 2020).

Chapter 3: Insights on retreat patterns in the Western Ross Sea from morphometric analysis of small-scale ice-marginal landforms

Conducted with support from: Lauren E. Miller and. Marion Donald. A manuscript in preparation for submission to *The Cryosphere*.

3.1 Introduction

The identification and description of submarine landforms formed by glacial processes have been greatly facilitated by advances in marine-geophysical technologies, particularly acoustic methods deployed on high-latitude continental margins. The ability of these methods to image the seafloor at a higher resolution than would be possible from radar satellite altimetry of modern subglacial and ice-marginal environments make them particularly effective at studying and characterizing sediments on the deglaciated continental shelf. Sediments deposited below wave-base tend to be preserved in the Quaternary geological record due to reduced seafloor erosion and reworking compared to their subaerial counterparts (Dowdeswell et al., 2016). Similarly, submarine landforms unaffected by the cyclical advance and retreat of ice sheets since the Last Glacial Maximum (LGM) are well preserved and represent the last geomorphic imprint before ice-sheet retreat, offering valuable insights into the past extent of the ice sheet. The spatial distribution of landform assemblages spanning hundreds of kilometers of paleo-ice stream beds on the deglaciated continental shelf has facilitated the interpretation of the deglacial histories and ice dynamics of paleo-ice streams during landform formation. The increase in swath bathymetry and seismic surveys have furthered marine geological interpretations, revealing substantial spatiotemporal variability in ice-sheet retreat patterns across different sectors of the Antarctic Ice Sheet (AIS) since the LGM (Anderson et al., 2014).

Glacial landforms observed across the deglaciated continental shelf of Antarctica formed during the last glacial cycle, as evidenced by their positioning above the latest glacial unconformity (Shipp et al., 2002; Mosola and Anderson, 2006). These landforms are broadly defined within three categories: subglacial, ice-marginal, and proglacial landforms. The morphometrics of each landform category are highly dependent on the glacial processes that create them. Subglacial landforms, formed at the ice-bed interface, result from erosive forces and are mostly oriented parallel to the direction of ice flow. In contrast, ice-marginal landforms, created in part by the ability of glaciers to transport vast amounts of sediment from their interior to their margin, are typically oriented orthogonal to the direction of flow (Benn and Evans, 2010; Dowdeswell et al., 2016). Ice-marginal landforms are particularly useful for reconstructing the extent and behavior of glaciers since the LGM because they indicate former locations of the grounding line, the point where grounded ice loses contact with the bed and a freely floating ice shelf is possible. Geomorphological analysis of landforms in the Ross Sea of Antarctica has improved our understanding of its deglacial history as their interpretation helps identify possible paleo-ice sheet drainage pathways (Anderson et al., 2014), identify different retreat scenarios and potential physiographic controls (Halberstadt et al., 2016; Bart et al., 2017; Prothro et al., 2020), infer bed characteristics on the continental shelf (Halberstadt et al., 2018), differentiate glacimarine processes between the WAIS and EAIS (Prothro et al., 2018), and infer marine-based ice sheet instability by linking their morphology to perturbations at the grounding line (Simkins et al., 2018).

This work combines high-resolution bathymetry and an automated landform extraction method to identify hundreds of previously unrecognized small-scale ice-marginal landforms in the Western Ross Sea. By analyzing the morphometric properties of these landforms, we can infer their relative timing of formation, corresponding to periods of grounding line stability. The interpretation of landform morphometrics helps untangle the role of local topography and overall retreat patterns since the LGM, thereby linking topography to grounding line stability.

3.2 Deglacial history of the Ross Sea

Retreat of the Antarctic Ice Sheet (AIS) took place between the Last Glacial Maximum (LGM) and the late Holocene (Anderson et al., 2002). Studies of the AIS are typically considered in the context of its major sectors, the West Antarctic Ice Sheet (WAIS) and the East Antarctic Ice Sheet (EAIS), which have different characteristics and responses to environmental variables. The retreat between the WAIS and EAIS is believed to have followed different patterns. The WAIS sector, mostly grounded below sea level and currently experiencing faster retreat rates and enhanced melting, is thought to have reached the edge of the continental shelf in many areas (Anderson et al., 2002). In contrast, the EAIS, largely grounded above sea level and considered stable in many regions, is believed to have only reached the mid-shelf position in many locations, while other LGM margins are close to the modern grounding line positions (Anderson et al., 2002).

Interpreting the deglacial history of the Ross Sea is complex in part due to the convergence of ice streams from both the WAIS and EAIS, which account for approximately 25% of all AIS drainage and make the Ross Sea the largest drainage basin in Antarctica. The central and eastern Ross Sea sectors primarily draw ice from the WAIS interior through ice streams that act as major conduits, while geomorphological evidence supports significant drainage of the EAIS into the western Ross Sea (Shipp et al., 1999; Mosola and Anderson, 2006; Greenwood et al., 2012; Anderson et al., 2014). There are significant differences in the large-scale topography between the eastern and western Ross Seas, the former is dominated by subdued glacial troughs while high relief banks in the western Ross Sea acted as pinning points to stabilize the grounding line (Halberstadt et al., 2016). Additionally, the geology in the eastern Ross Sea, consisting of unconsolidated Plio-Pleistocene sediments that thicken towards the shelf edge (Alonso et al., 1992; De Santis, 1999), is associated with fast flow, supported by the presence of mega-scale glacial lineations (MSGLs) formed subglacially by ice streams. The presence of widespread large-scale grounding zone wedges (GZWs) near the shelf edge confirms the ice sheet was grounded at the shelf break in the eastern Ross Sea. In contrast, the geology in the western Ross Sea is more variable and composed of older, more consolidated substrate, which inhibits fast ice flow (Stokes and Clark, 2003; Winsborrow et al., 2010). Analysis of sediment facies to determine whether sediments were deposited subglacially or proximal to the grounding zone confirms contrasting differences in the glacimarine processes taking place in the two sectors of the Ross Sea (Prothro et al., 2018). Linear features in the western Ross Sea are sparse, making the determination of paleo-grounding line extent dependent on the interpretation of ice-marginal landforms. A combination of sedimentological and geomorphological works agree that the western Ross Sea underwent small-scale, yet frequent grounding line retreat, while the eastern Ross Sea experienced an episodic style of retreat characterized by long periods of grounding line stability (Halberstadt et al., 2016; Prothro et al., 2018; Simkins et al. 2018).

Halberstadt et al., (2016) utilized high-resolution bathymetry to propose that the large-scale pattern of retreat in the Ross Sea is more complex than had been previously suggested, highlighting topography as an important control on ice-sheet drainage and indicating asynchronous retreat between glacial troughs. Similarly, Simkins et al., (2018) mapped and grouped ice-marginal landforms into two distinct groups based on their morphologies: moraines and GZWs. In this study, we dine landforms with an amplitude of less than 10 meters as small-scale. Small-scale recessional moraines, which are symmetric in shape, suggest a steady, small-magnitude, and more controlled style of retreat. Small-scale grounding zone wedges are asymmetric in shape, indicate an episodic style of retreat, where the grounding line remained stable for longer, allowing for the accumulation of sediment at the grounding line, and even promoting grounding line advance by reducing the water depth required to offset the buoyancy associated with retreat on a reverse bed slope (Alley et al., 2007). Current inventories of GZWs in the high-latitudes report amplitudes of 20 to 200 m, yet Simkins et al., 2018 reported landforms that follow the conventional description of GZWs, but at smaller-scales, which are not found in other inventories of GZWs. Simkins et al., demonstrated that the difference in metrics of ice-marginal landforms found in the Ross Sea is enough to differentiate them into groups representing recessional moraines and GZWs. Here, we perform additional morphometrics analysis of the hundreds of landforms found in the Ross Sea.

3.3 Methods

Legacy multibeam data used for morphometric analysis was collected aboard the RVIB Nathaniel B. Palmer. Detailed information about collection and processing methods is described in Halberstadt et al. (2016). Elevation transects used for analysis were aligned with the inferred direction of ice flow, based on landform orientations. Transects were designed to capture as many ice-marginal landforms as possible within a field of similar landforms and were classified into the two morphotypes described by Simkins et al. (2018): moraines and GZWs. A total of 14 transects were drawn for moraines (n=997) and 11 transects for GZWs (n=631). The length of each transect was determined by the presence of identified landforms and adjusted for gaps or artifacts in the bathymetry (Figure 3.1). Slope values for each transect were calculated by extracting start and end elevation values from high-resolution (50 m) bathymetry to account for localized changes in slope. Elevation transects were processed using a minimum amplitude threshold of 0.6 m, approximating the expected resolution of identifiable landform features given the vertical resolution of the bathymetry data (50 cm) and anticipated noise levels along trackline and the center-beam fringes, and a minimum width threshold of 15 m for landform identification. Maximum width thresholds were set at 200 m for moraines transects and 2,000 m for GZW transects. These thresholds were chosen to match manually mapped landforms and to exclude small-scale roughness in the bed topography unrelated to ice-marginal landforms.

The extracted morphometric properties included amplitude, width (or along-flow length), cross-sectional area, spacing, and a width-to-amplitude ratio (Figure 3.2, 3.3; GZW example in Figure A3.1). Outliers were removed from each morphotype population by excluding values that fell significantly outside the typical range of the distributions using the criteria (Q1 – (3 * IQR)) and (Q3 + (3 * IQR)), where Q1 and Q3 are the first and third quartiles, and IQR is the interquartile range. Statistical analyses were conducted by transect and morphotype population to explore correlations between morphometrics, spacing, slope, and water depth. Slope was calculated for each individual landform within a transect and was determined using Equation 1,

$$m = \frac{y2-y1}{x2-x1} \quad \text{Eqn. 3.1}$$

where, *y2* and *y1* are the elevations of consecutive landforms and *x2* and *x1* are their respective distances along the transect. This was done to introduce and test a local slope between adjacent landforms, rather than assuming a constant slope for an entire transect. To assess the relationship between morphometric properties and the local slope, Spearman's rank correlation coefficients were computed for each property against slope. Spearman's rank correlation was chosen to measure the strength and direction of the monotonic relationship between two variables, suitable for our non-parametric data.

3.4 Results

Using the defined threshold, a total of 997 individual landforms were identified in moraine transects and 631 in GZW transects. The length of elevation transects varied from 4 to 25 km. In some cases, the transect length was limited by the width of the multibeam track, and so there are cases where fields of landforms are not fully captured due to gaps in the bathymetry. Most transects contained largely uninterrupted sequences of landforms, with the number of landforms ranging from 18 to a maximum of 184 per transect. The total number of landforms identified (n = 1,628) through the automatic extraction using predefined morphometric thresholds is significantly higher than those manually mapped using hillshading techniques (n = 646). This discrepancy is particularly evident in GZW transects, where hundreds low-amplitude features were identified between GZWs. This pattern was consistent across all GZW transects, suggesting that it may be incorrect to assume that GZWs are the sole type of landform present in these fields and instead.

Descriptive statistics of morphometric properties of identified landforms are presented in Table 3.1 for both moraine and GZWs transect populations. The distributions of the morphometric properties for both populations are heavily right-skewed (Figure 3.4). We found statistically significant differences in amplitude, width, and cross-sectional area between the two populations, but no significant differences in the width-to-amplitude ratio.

Based on ANOVA results, significant variance was observed within the moraines population for width and amplitude between transects, with width-to-amplitude ratio and spacing showing the greatest variation between transects. In contrast, the GZWs population exhibited significant differences only in the amplitude, the width-to-amplitude to ratio, and spacing (Table 3.2).

For both moraines and GZW populations, there is a notable negative correlation between the amplitude, width, cross-sectional area of a given landform and the local bed slope between adjacent landforms. However, the correlation with spacing is notably weak (Table 3.3). This analysis assumes that all landforms along a transect were formed during a single period of ice sheet retreat with no subsequent re-advances reworking the landforms, which is a reasonable assumption given the landform assemblage relationships. To gain a more detailed understanding of these relationships, the analysis was conducted for each transect, with the results presented in a correlation matrix (Figure 3.5).

The distribution of the spacing is heavily right-skewed. The spacing between landforms is remarkably consistent, around 150 m, across transects in both populations (Figure 3.6). The interquartile range for spacing is between 75 and 175 m for both populations, and statistical tests

reveal no significant difference between them. While the relationships between morphometric properties and spacing are less consistent compared to those observed with slope, the correlation matrix generally indicates a positive correlation across most transects, indicating that larger landforms tend to be spaced further apart (Figure 3.7).

3.5 Discussion

3.5.1 Advantages of automatic landform identification

Based on statistical analysis of hundreds of ice-marginal landforms that form at paleo-grounding lines, the metrics of the landforms are challenging to fully categorize into distinct morphotypes. From the transects selected for the study, 485 landforms were initially mapped as moraines and 161 as GZWs using traditional visual-based hillshading techniques. The use of automatic landform extraction has significantly increased these numbers, identifying 997 landforms in moraine transects and 631 in GZW transects.

The disparity between the number of landforms identified through automatic extraction (n = 1,581) and those manually mapped using hillshading techniques (n = 646) highlights several factors that favor automated methods. Manual mapping relies heavily on the use of hillshades, which are generated by simulating artificial illumination sources from specific angles. This approach can be limited by the angle of illumination. Incorrect azimuth angles or the lack of a multidirectional hillshade can obscure certain landforms, leading to their potential omission and identification. Additionally, some landforms, particularly those with insufficient amplitude, may not cast discernible shadows under hillshade techniques, making them difficult to detect manually. In contrast, automated landform extraction methods analyze elevation profiles with consistent and objective criteria, resulting in a more exhaustive identification process. However, a notable limitation of these methods is their reliance on one-dimensional transects, which restricts the analysis to a linear perspective.

3.5.2 Challenges in morphometric differentiation

We hypothesized that the width-to-amplitude ratio could distinguish between the two types of landforms by identifying features above a certain threshold. However, the distribution of this ratio is strikingly similar between the two populations. We attribute this similarity to the high number of newly identified landforms, which significantly impact the distributions of the morphometric properties extracted. These small-scale landforms, often found between previously identified GZWs, display low values for both width and amplitude. The width-to-amplitude ratio follows a heavily right-skewed distribution, indicating that the majority of landforms identified have lower ratio values and therefore exhibit morphometric characteristics more akin to symmetric moraines rather than typically asymmetric GZWs. The abundance of small-scale landforms may explain the inability to establish a width-to-amplitude ratio threshold that differentiates between the two morphotypes.

Not only is it useful to use morphometrics to distinguish between moraines and grounding zone wedges, which we show here is challenging, it is also useful to be able to distinguish landforms that have different genetic controls, such as those formed by icebergs and in the subglacial environment. The amplitude range of the landforms identified in this study is lower compared to other small-scale landforms like mega-scale glacial lineations (MSGLs;

Spagnolo et al., 2014), which are erosional features associated with ice streaming. Instead, their amplitude range more closely resembles that of corrugation ridges (Graham et al., 2013; Dowdeswell et al., 2020), iceberg ploughmarks (Wise et al., 2017), and sub-ice shelf keel scours (Graham et al., 2010) observed on the Antarctic continental shelf. Although iceberg ploughmarks have been observed elsewhere in the Western Ross Sea, the absence of these curvilinear features near the transects suggest that the newly identified landforms are unlikely to be ploughmarks. Sub-ice shelf keel scours typically have an amplitude range of 1-10 meters, are often found on the surface of GZWs, and exhibit low parallel conformity (Smith et al., 2019). However, their typical widths and spacing exceed those observed in our dataset. Corrugation ridges, which are small-scale transverse ridges either within or on top linear scours formed by ice flow, require tidal lifting and settling of the ice shelf. While the description and amplitude of corrugation ridges closely match the newly identified landforms, these ridges also exhibit a high degree of cyclicity in their spacing due to the 14-day spring-to-neap cycle thought to drive their formation. Such cyclicity is not evident in the Ross Sea dataset, and this level of spacing detail has thus far only been observed through the deployment of underwater vehicles capable of imaging the seafloor at an exceptionally high spatial resolution (Graham et al., 2013; Dowdeswell et al., 2020). Therefore, it is unlikely that the observed landforms would be considered corrugation ridges as their spacing does not indicate tidal action.

3.5.3 Influence of local bed slope and spacing on morphometry

The strong correlation between local bed slope and both amplitude and width indicates that the slope immediately downstream of a landform significantly influences the amplitude and width of depositional landforms (Figure 3.5). Moraine amplitude is more negatively correlated with slope, suggesting that the sedimentological processes responsible for landform building are inhibited or reduced by higher slopes. Alternatively, other factors influencing the style of retreat on higher slopes may also be at play. A negative correlation between slope and both amplitude and width suggest that more negative slopes (reverse slopes), are associated with decreased landform amplitude and width. According to the marine ice sheet instability (MISI) theory, reverse slopes promote grounding line retreat, making it harder to achieve the environmental conditions necessary for grounding line stability (Schoof, 2007; Robel et al., 2019). This instability would hinder the accumulation of sediment at the grounding line, explaining the lower amplitudes and widths observed on reverse slopes. The negative correlation observed across most transects also indicates that very gentle slopes (values approaching zero) tend to result in higher amplitude and width values. In this scenario, MISI would not occur, and the grounding line is more likely to stabilize on gentle or normal slopes. The correlation between local bed slope and morphometric properties suggests that the immediate slope surrounding a landform (a previous grounding line position) controls the magnitude of the morphometric properties. Therefore, the local bed slope also influences the occupation time of the grounding line at a given location.

While both amplitude and width show negative correlations with local bed slope, the width-to-amplitude ratio exhibits a positive correlation with local bed slope. This difference in correlation direction can be explained by the proportional decrease of these two properties. The ratio increases if the amplitude decreases faster than the width. In other words, the positive correlation of the width-to-amplitude ratio with slope likely arises because the amplitude of the landform decreases more rapidly with increasing slope than the width does. This suggests that

steeper slopes inhibit vertical growth more than horizontal growth. This is consistent with ice dynamics theory, where steeper reverse slopes result in greater ice flow velocities, thereby reducing the likelihood of still-stands that would lead to vertical accumulation at the grounding line. Despite the varying strengths and directions of the correlations, results suggest that local bed slope significantly influences the morphometric properties of the identified landforms.

The distribution of spacing values and statistical tests reveal no significant difference between the moraine and GZW populations. Although it is generally understood that moraines and GZWs represent retreat styles, this finding might suggest otherwise. However, we do not favor this interpretation. The automatic extraction method is identifying many landforms with morphometric properties resembling moraines within the GZW transects. A more plausible explanation for the similarity in spacing between the moraine and GZW populations is that retreat styles often transition from steady to episodic. While the overall retreat pattern in all transects appears to be regular, characterized by frequent retreat events, there are locations where the retreat follows an episodic pattern. We hypothesized that there could be a relationship between spacing and local bed slope, where a steeper slope would correspond to greater spacing between landforms. However, our analysis did not reveal such a relationship between spacing and slope, or any other morphometric property considered, suggesting that there are other controls on landform spacing. It is important to note that the retreat patterns inferred from ice-marginal landforms since the LGM consider relatively short-term retreat rates and may not fully capture the complexities influencing glacier behavior on longer timescales. Recent observations highlight significant decadal fluctuations in Antarctic glacier climate forcing (Jenkins et al., 2018; Paolo et al., 2018; Robel et al., 2018), suggesting that long-term trends in climate forcing may introduce background variability in the retreat patterns observed in our dataset.

3.5.4 Inferred retreat patterns

The positioning of newly identified landforms between previously identified moraines and GZWs suggest they could be recessional moraines deposited during periods of steady retreat. This supports the idea that recessional moraines represent still-stands during overall glacial retreat, but over shorter timescales. Thus, recessional moraines could indicate steady retreat between periods of episodic retreat associated with longer periods of grounding line stability. In conclusion, small-scale ice-marginal landforms are dominated by landforms with morphometric properties typical of moraines. They are much more common and they are the de facto kind of landform that will be constructed unless other environmental forcings, which could not be determined through our analysis, promote longer periods of grounding line stability and therefore the construction of GZWs. It is to be expected then, that recessional moraines will be present in between GZWs. We typically describe the style of retreat as episodic whenever GZWs are observed. This interpretation is still valid in the sense that a long “episode” of grounding line stability is required to construct GZWs, but it does not necessarily mean that following a period of stability when a GZW is constructed, there is rapid retreat until the next period of grounding line stability leads to the creation of another GZW. But rather, we interpret it as: whenever retreat starts after the deposition of a GZW, a steady style of retreat will occur whereby small-scale recessional moraines are deposited until the next time the climate forcings force a longer period of stability which would lead to deposition of a GZW.

3.6 Conclusion

In conclusion, this work demonstrates the advantages of automatic landform identification methods over traditional visual-based techniques, as evidenced by the significantly higher number of landforms identified through automated extraction. Statistical analyses of morphometrics reveal that landforms in moraines and GZW transects are essentially indistinguishable, except when considering local bed slope and spacing. The local bed slope, known to impact grounding line dynamics, appears to have a larger control on landform morphology. Specifically, steeper slopes inhibit vertical growth more than horizontal growth, influencing landform amplitude and width. We interpret the retreat styles inferred from ice-marginal landforms to reflect a combination of steady and episodic retreat styles. Long-term climate trends may introduce climate variability in retreat patterns, contributing to the observed variability in our dataset. Overall, the study highlights the complexity of retreat patterns and the significant role of local bed slope in shaping the morphometrics properties of ice-marginal landforms.

Table 3.1. Descriptive statistics for landform amplitude, width, cross-sectional area, width-to-amplitude (W/A) ratio, and spacing between landforms, grouped by moraine and GZW populations. The p-values from non-parametric Mann-Whitney U test comparing morphometric properties between populations is also shown.

	Moraines				GZWs				
	Mean	Median	SD	Max	Mean	Median	SD	Max	p-value
Amplitude (m)	2.2	1.73	1.65	17.6	2.0	1.6	1.5	11.2	0.015
Width (m)	59	48	39	199	69	45	84	1001	0.200
Cross-sectional area (m^2)	157	81	227	3476	201	69	502	6443	0.023
W/A ratio	34	27	25	197	38	29	28	236	0.028
Spacing (m)	151	125	94	900	159	125	127	1475	0.940

Table 3.2. Results of ANOVA tests, measuring the variance between transect means relative to the variance within transects, for morphometric properties across different transects within the moraine and GZW populations.

	Moraines		GZWs	
	ANOVA F-stat	p-value	ANOVA F-stat	p-value
Amplitude (m)	4.61	$9.70e^{-08}$	1.58	$1.07e^{-01}$
Width (m)	3.60	$1.46e^{-05}$	4.45	$4.56e^{-06}$
Cross-sectional area (m^2)	2.01	$1.77e^{-02}$	3.25	$4.17e^{-04}$
W/A ratio	9.12	$6.03e^{-18}$	6.05	$8.27e^{-09}$
Spacing (m)	16.55	$1.23e-^{34}$	21.68	$9.72e^{-35}$

Table 3.3. Spearman rank correlation coefficients and corresponding p-values for the relationship between morphometric properties and local bed slope within the moraine and GZW transects.

	Moraines		GZWs	
	Correlation	p-value	Correlation	p-value
Amplitude	-0.250	$2.039e^{-15}$	-0.173	$1.478e^{-05}$
Width	-0.513	$3.444e^{-67}$	-0.412	$8.009e^{-27}$
CS area	-0.449	$6.472e^{-50}$	-0.344	$1.247e^{-18}$
W/A ratio	0.247	$3.941e^{-15}$	0.183	$4.628e^{-06}$
Spacing	-0.056	$8.210e-^{02}$	-0.044	$2.814e^{-01}$

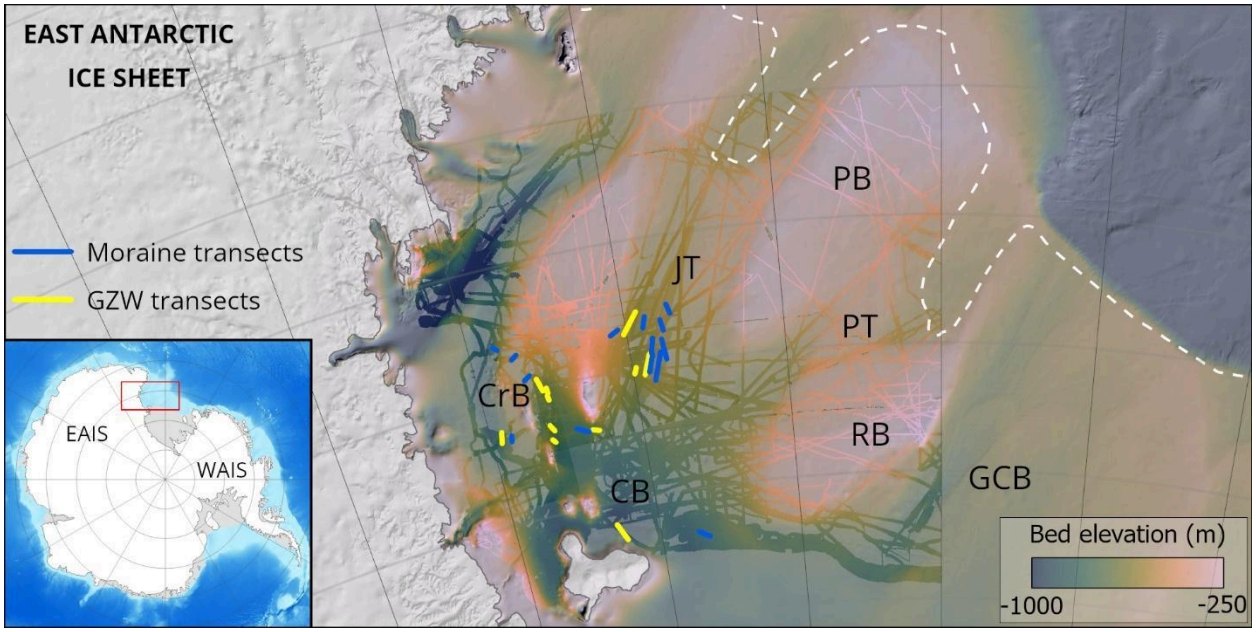

Figure 3.1. Location of moraine and GZW transects in the Western Ross Sea. Background bathymetry from Morlighem et al., 2020. Dashed white line indicates LGM ice extent. CrB (Crary Bank), CB (Central Basin), JT (JOIDES Trough), PB (Pennell Bank), PT (Pennell Trough), RB (Ross Bank), GCB (Glomar Challenger Basin).

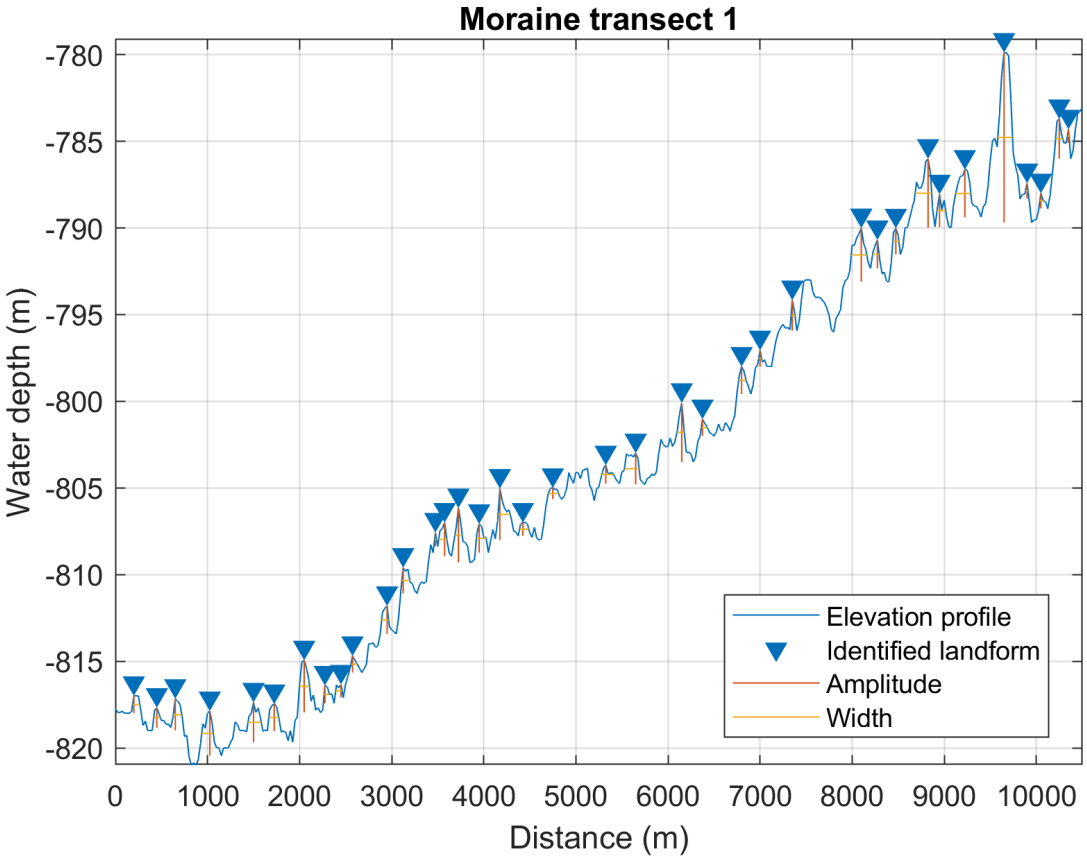

Figure 3.2. Example transect illustrating landforms identified along a moraine transect. Amplitude and width properties are denoted by the red and yellow lines, respectively. The cross-sectional area is computed by multiplying amplitude by width. Width-to-amplitude ratio is computed by dividing width by amplitude, with higher values signifying greater asymmetry.

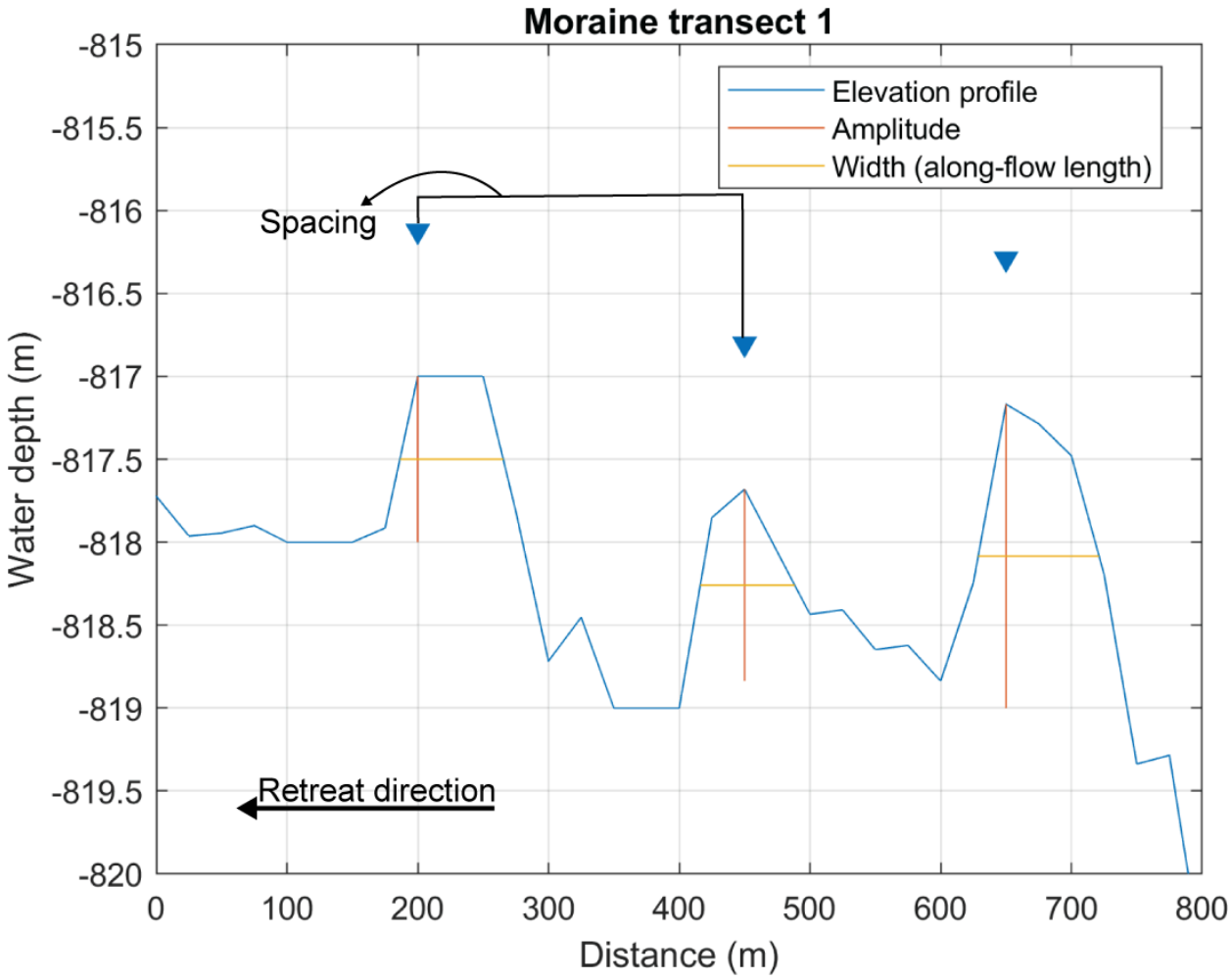

Figure 3.3. Zoomed in view of Figure 3.2, highlighting the spacing between landforms, as well as the amplitude and width (along-flow length) measured for each landform.

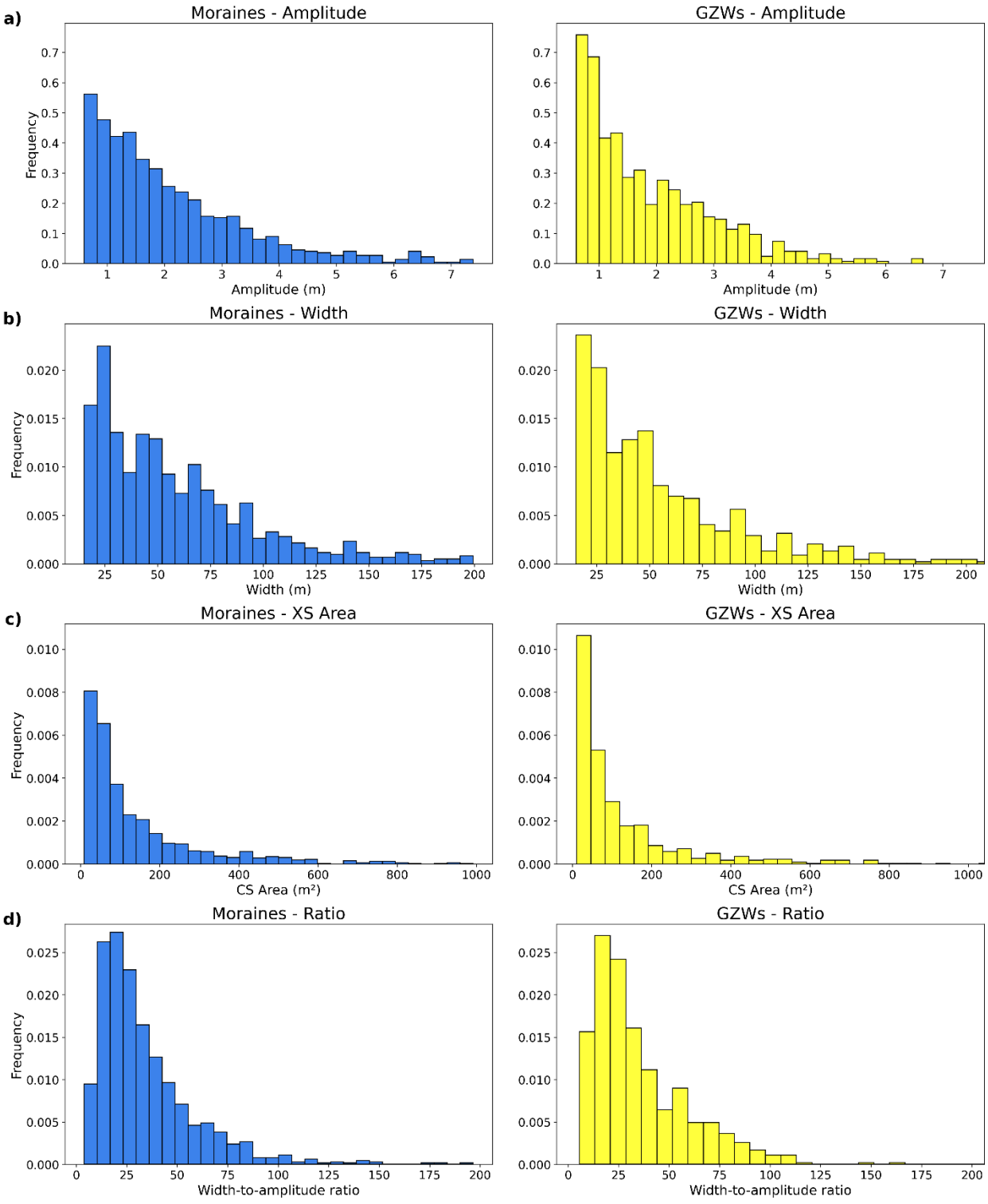

Figure 3.4. Frequency distribution of **(A)** amplitude, **(B)** width, **(C)** cross-sectional (XS) area, and **(D)** width-to-amplitude ratio of landforms identified.

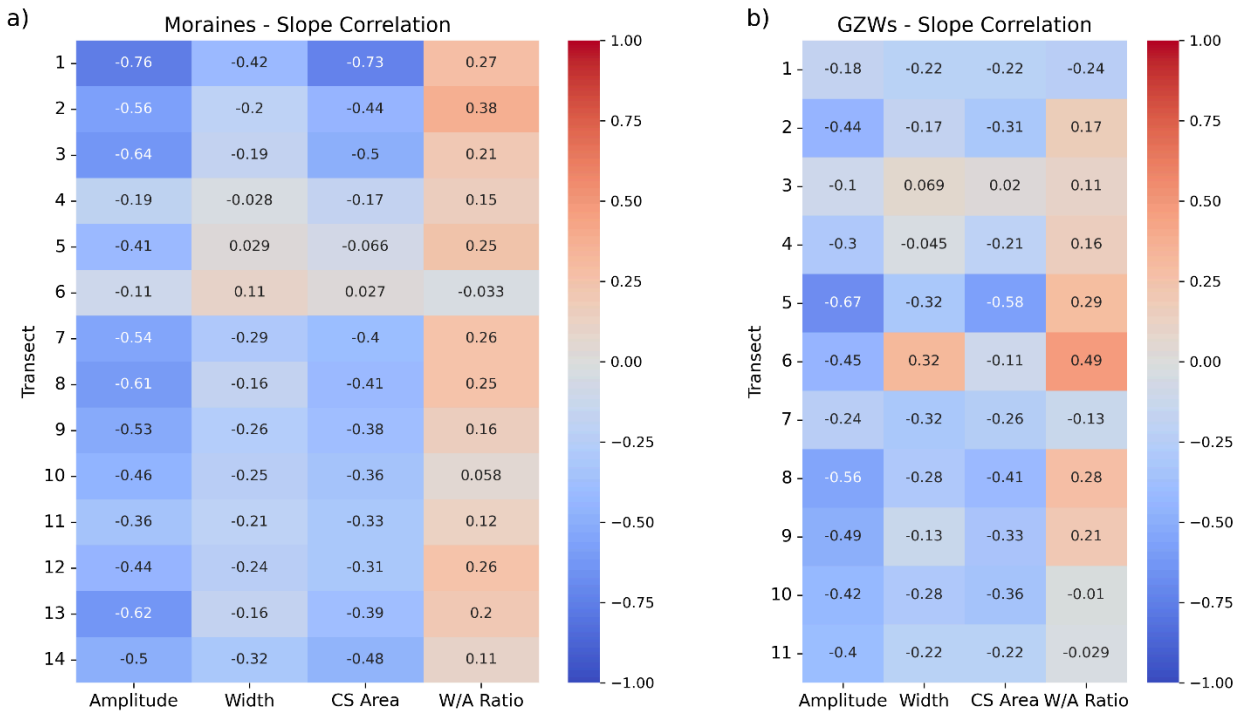

Figure 3.5. Heatmap of Pearson correlation coefficient between local bed slope and morphometric properties (width, amplitude, cross-sectional area, width-to-amplitude ratio) across individual transects for **(A)** moraines and **(B)** GZWs.

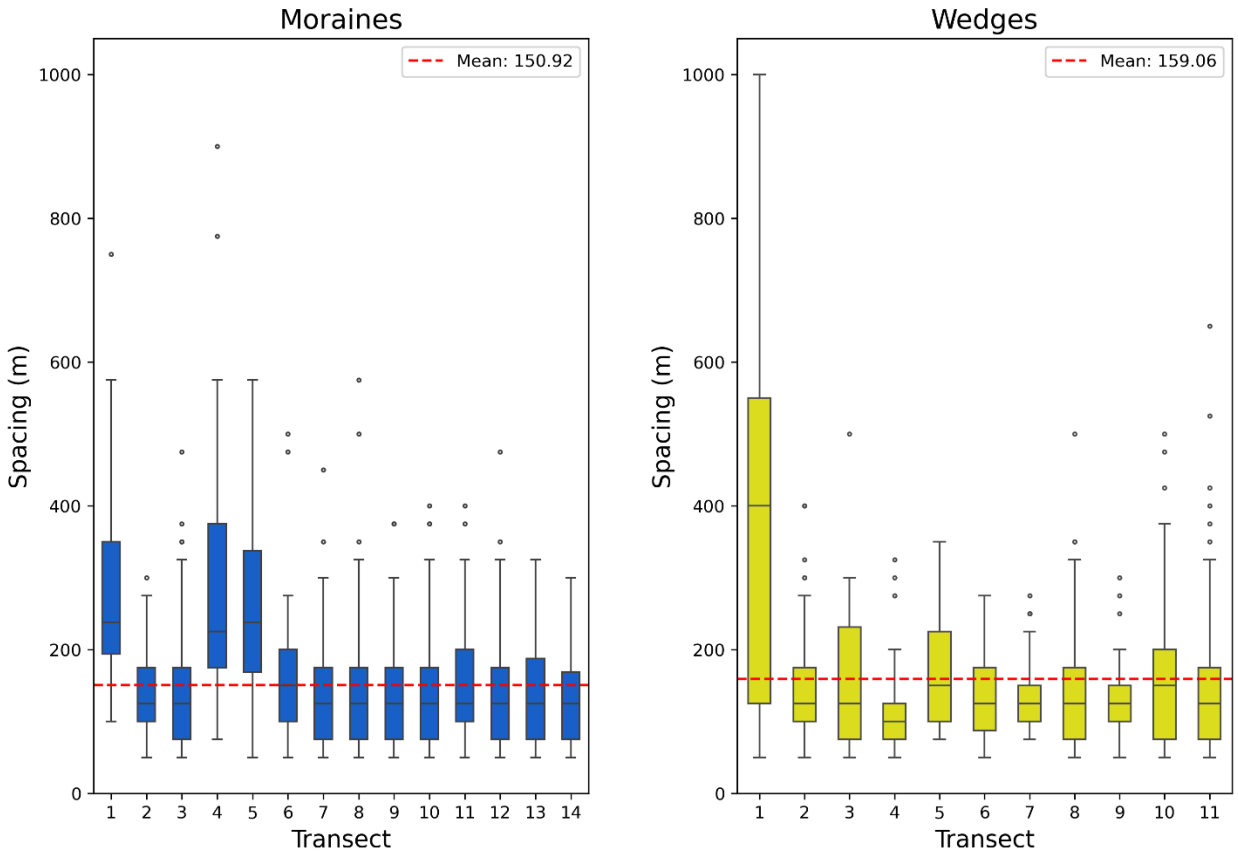

Figure 3.6. Distribution of landform spacing across different transects for moraine and GZWs. The red dashed line indicates average spacing for the respective population.

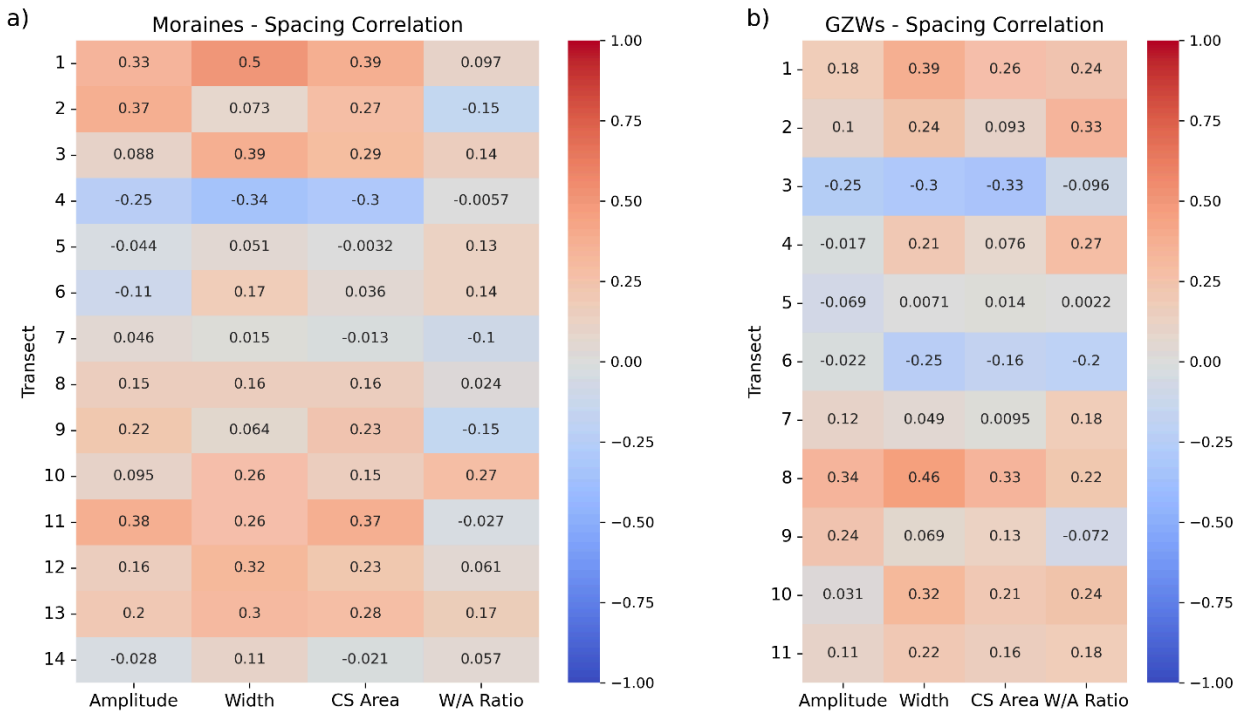

Figure 3.7. Heatmap of Pearson correlation coefficient between landform spacing and morphometric properties (width, amplitude, cross-sectional area, width-to-amplitude ratio) across individual transects for **(A)** moraines and **(B)** GZWs.

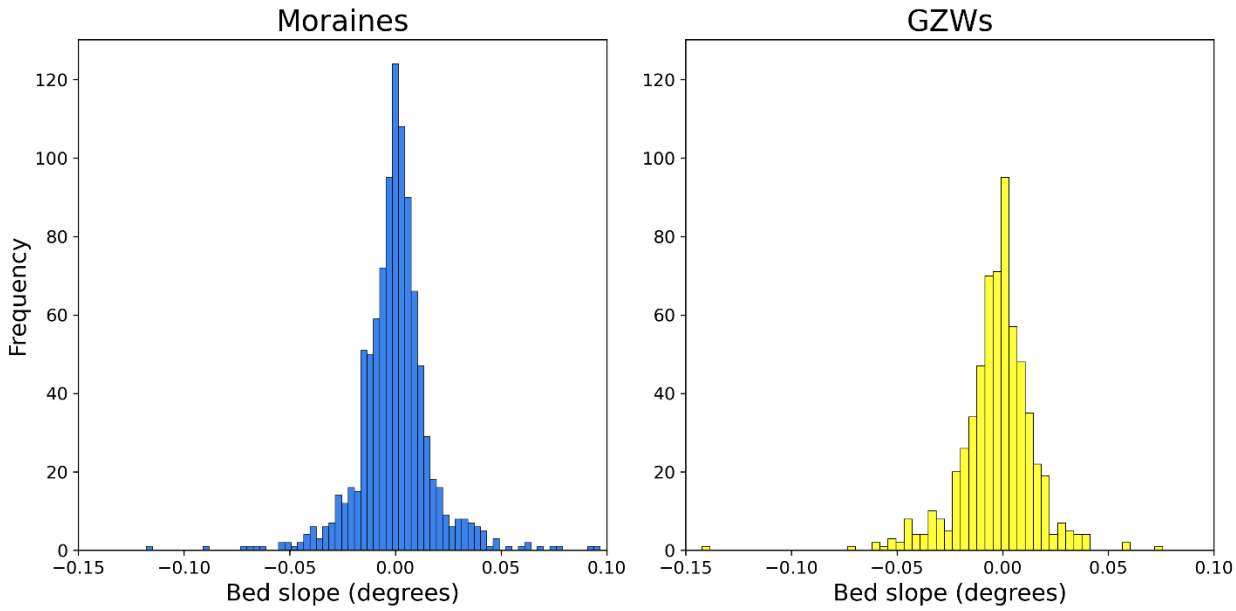

Figure 3.8. Frequency distribution of local bed slope and landforms identified.

Chapter 4: Investigating Grounding Zone Wedge Geometry Using a One-Dimensional Coulomb-Plastic Flow Model

Conducted with support from: John E. Christian, and Lauren E. Miller. A manuscript in preparation for submission to *Earth Surface Processes and Landforms*.

4.1 Introduction

Ice sheet stability and mass balance are heavily influenced by ice streams, which drain a substantial portion of the Antarctic and Greenland ice sheets, accounting for roughly 90% and 50%, respectively (Bamber et al., 2000). Satellite observations of contemporary ice streams reveal a high degree of dynamicity in ice stream dynamics on sub-decadal timescales, suggesting a strong influence on the spatiotemporal evolution of grounding line positions (Rignot, 2008). While direct observations of contemporary ice stream beds remain limited, the preserved landforms within paleo-ice stream beds, dating back to the Last Glacial Maximum (LGM), offer valuable insights into the ice dynamics at the time of their formation. Landform assemblages have been used to reconstruct the deglacial histories of numerous paleo ice-streams across Antarctica (Livingstone et al., 2012). These histories reveal an asynchronous retreat which has resulted in diverse sets of landforms across paleo ice-streams troughs. The interpretation of these landforms not only provides insights into the style of retreat but also sheds light on how the underlying bed topography influences ice dynamics.

Among these landforms, grounding zone wedges (GZWs) are described as wedge-shaped deposits that are formed by rapid sediment delivery to the grounding zone of ice streams during retreat. Understanding the mechanisms that give rise to GZWs is particularly important since they occur in regions of fast-flowing ice, such as cross-shelf troughs and fjords systems (Batchelor and Dowdeswell, 2015). By reconstructing the formation of GZWs and the corresponding ice dynamics, we can more effectively predict the behavior of fast-flowing regions under similar conditions, thus improving our ability to manage and mitigate the effects of climate change on ice sheets.

Identifying depocenters, such as GZWs, in the geological record allows us to infer the dynamics of previous ice sheets and determine the location of grounding line still-stands or re-advances (Dowdeswell et al., 2008). However, the specific location, as well as the morphometric and stratigraphical characteristics of GZWs are still not fully understood, leading to uncertainty about what conditions differentiate them from other constructional landforms (Powell, 1981; King et al., 1991; Batchelor and Dowdeswell, 2015). Although GZWs have been suggested to promote grounding line stability, their initial formation is complex and influenced by various factors such as sediment flux, ice thinning rate, and the geometry of the continental shelf (Batchelor and Dowdeswell., 2015). Examining sediment sorting can provide indications about the prevailing climatic conditions during GZW formation. Sorted sediment from subglacial meltwater could suggest that ice-sheet mass loss was dominated by meltwater runoff rather than iceberg calving (Dowdeswell and Fugelli, 2012; Bjarnadóttir et al., 2013).

Despite their significance, a comprehensive synthesis of GZW locations, and their morphological and stratigraphical characteristics is currently lacking, leading to uncertainty about what conditions differentiate them from other depositional landforms. The presence of GZWs on the seafloor indicates that ice-sheet retreat was episodic and punctuated by still-stands in the position of the grounding line. These still-stands lasted for decades to centuries, or even

millennia as some studies have found (Bart et al., 2017), suggesting that ice sheets were relatively stable during this time. Although geophysical observations have characterized the volume of submarine landforms, the time required for their development remains largely unknown (Dowdeswell et al., 2016).

Given the occurrence of GZWs within paleo-ice stream troughs, and considering the critical roles of ice deformation, basal sliding, and subglacial deformation in controlling ice flow velocities (Boulton, 1986), as highlighted by the discovery of weak and saturated sediments beneath Whillans Ice Stream (Alley et al., 1986, 1987; Blankenship et al., 1987), it follows that beds comprised of unconsolidated sediment can deform under relatively low stressed imposed by overlying ice during ice streaming. Based on this principle, we use a one-dimensional numerical ice-sheet model to simulate the processes of sediment deposition at the grounding line which results in the construction of GZWs, with the goal of recreating GZWs that exhibit the morphometrics of observed GZWs in the geologic record. The dimensions of GZWs are controlled by the flux of sediments to the grounding line, the duration of the still-stand, the width of the paleo-ice stream, and the shape of the sub-ice shelf cavity (Alley et al., 2007; Dowdeswell and Fugelli, 2012). The first two controls can be explicitly tested in the model. The Coulomb-slip mode is adopted in the model for the region near the grounding zone because Coulomb-plastic behavior does a good job of representing the reduction of till strength and increased sliding speed when water pressure is high (Kavanaugh and Clarke, 2006), and accounts for the fact that basal shear stress decreases as the ice nears flotation.

Till deposits undergo both plastic and elastic deformation in response to applied stress. Initially, the till deforms elastically, meaning that it can return to its original shape when the stress is removed. However, as the shear stress increases, the till will eventually undergo plastic deformation, where it will not return to its original shape upon stress removal. During Coulomb-plastic deformation, the applied stress exceeds the yield strength, causing the till to experience permanent strain and deformation (Tulaczyk et al., 2000). This behavior is crucial for accurately modeling the dynamics near the grounding zone and understanding the formation of GZWs, because at this point, the ice can slide over the till. Consequently, sliding is no longer controlled by the local properties of the till but rather by sources of resistance on the bed.

By simulating the process of sediment accumulation at the grounding during glacial retreat that results in the construction of GZWs over time, this chapter explores the effects of varying sediment fluxes and stoss angles on the geometry of the constructed GZWs and the time required for them to be constructed under different ice dynamics, something that has not been attempted at this scale and resolution. This serves as a test of the feasibility of this model in identifying the environmental variables or controls required to stabilize a retreating glacier.

4.2 Model description

We use a one-dimensional ice-sheet model based on the shallow-shelf approximation (SSA), developed by Schoof (2007). The SSA model assumes that ice flow is dominated by longitudinal stretching and basal sliding. This model, while simple, can effectively resolve both vertical and longitudinal stress components (Equation 1; Schoof, 2007).

$$\rho_i g h \frac{\delta s}{\delta x} = \frac{\delta}{\delta x}\left(2hA^{-\frac{1}{n}}\left|\frac{\delta u}{\delta x}\right|^{\frac{1}{n}-1}\frac{\delta u}{\delta x}\right) - \tau_b \qquad \text{Eqn. 4.1}$$

The stress balance is represented as the balance between the driving stress and the combined effects of longitudinal stretching and basal drag. On the left-hand side of the equation, the driving stress is defined, where ρ_i denotes ice density, g is the gravitational acceleration, h is ice thickness, and $\delta s \delta x$ represents the surface slope. The right-hand side includes two terms: longitudinal stretching and basal drag. Here, u is the horizontal ice flow velocity, A is the Glen flow coefficient and n is its exponent. The basal drag term, τ_b, is determined by the sliding relation.

The model used in this study was enhanced by Christian et al. (in prep) to include a frontal ablation term, allowing for the parameterization of internal climate variability observed in natural processes. More importantly, the improved model simulates the Coulomb-plastic deformation of sediments and accounts for horizontal sediment flux and evolving sediment thickness. This capability enables the model to consider sediment accumulation at the grounding line and the evolution of the upper sedimentary layer underneath ice streams, which transports sediment from the ice sheet interior to the marine environment, facilitating the deposition of sediment at the grounding line and contributing to the development of GZWs (Alley et al., 1986, 1989; Anandakrishnan et al., 2007).

This alternative model centers on Coulomb-plastic deformation as the primary mechanism for subglacial sediment transport. The model is based on the premise that the deformation of weak basal sediments is the main driver of rapid slip in modern West Antarctic ice streams, as suggested by landforms formed by paleo-ice streams (Alley et al., 1986). The model adopts a hybrid slip relation approach described by Tsai et al. (2015), where the bed supports the lesser of the two shear stresses: one corresponding to power-law slip over a hard bed substrate and the other to Coulomb-plastic failure of sediment. The effective pressure increases inland, governing the transition from power-law sliding to sediment deformation once basal shear stress exceeds the yield strength of subglacial sediment. In other words, the model treats the most inland regions of the ice stream profile as sliding over a hard bed substrate and it treats the region around the grounding line as a zone of Coulomb sliding (Figure 4.1).

To initialize a model run, we first establish a steady-state profile. Parameters that can be modified during this step include ice thickness, profile length, and the background slope on which the ice rests. This steady-state provides the necessary thickness and velocity conditions for the coupled ice-sediment model. Parameters tested include the stoss angle, the depth of the deformable sediment layer, and varying ice dynamics. The depth of the deformable layer is used as a direct way to control the sediment flux in the system (Equation 2). The characterization of sediment flux includes setting the depth of the deforming layer as well as its strain profile and how it is coupled with the overriding ice. The depth of the deformable layer is a significant unknown in modeling the evolution of depositional landforms as estimates range from centimeters to meters. Similarly, there are no data-based estimates for paleo-sediment flux for paleo-ice streams in West Antarctica (Bart et al., 2017). Following laboratory experiments, the model assumes the ice-sediment coupling is strongest at the ice-bed interface and drops off at a low effective pressure (Hansen and Zoet, 2022). This coupling refers to the ratio of sediment velocity to ice velocity, where a weak coupling value indicates glacier slip at the ice-bed interface. The sediment flux is defined as

$$Q_s = h_d s_p u_{sed} \qquad \text{Eqn. 4.2}$$

where h_d is the depth of the deformable layer that is used to control sediment flux to the grounding line, *sf* is a shape factor representing the depth-average velocity within the deforming later, and used is the horizontal velocity of sediment. The shape factor is introduced to simulate the decrease in sediment velocity with depth (Alley et al., 1986).

4.3 Model experiments and results

To test the effect of the stoss angle on the resulting GZW geometry, we ran the model under consistent initial conditions, maintaining ice thickness and ice velocity profiles, as well as the depth of the deformable layer constant across model runs. The adjustment of the stoss angle parameter determines when slumping on the ice-distal side begins; in other words, it controls the point at which the surface slope exceeds the stoss angle being tested. Initial model runs show that the stoss angle influences the overall geometry of GZWs, with an impact on both amplitude and width, with width referring to the along-flow length. As the stoss angle increases, the amplitude of the GZWs decreases, and the width increases (Figure 4.2). A linear regression of angles tested suggests that for every 0.01 degree increase in the stoss angle, the amplitude of the GZWs decreases by 1.06 meters, while the width increases by 220.00 meters. The relationships between the stoss angle and both amplitude and width demonstrate strong linear correlations, with R^2 values of 0.914 for amplitude and 0.834 for width.

The depth of the subglacial deformable layer, which has a direct effect on sediment flux, proved a significant control on the overall geometry of the constructed GZWs. As sediment flux increases, both the amplitude and the width of the GZWs exhibit a clear and substantial increase (Figure 4.3). Specifically, for every 10 centimeters increase in the depth of the deformable layer, the amplitude of the GZWs increases by 3.18 meters, and the width increases by 769.35 meters. The depth range tested extends from 5 cm to 100 cm, and the relationship between the depth of the deformable later and both amplitude and width demonstrates a close-to-linear correlation, with R^2 values of 0.914 and 0.974 for amplitude and width, respectively.

A third set of experiments focused on investigating the influence of varying ice dynamics on GZW formation while keeping the depth of the deformable layer and stoss angle constant. To achieve this, the model was initialized in a steady-state configuration on a gently sloping, retrograde bed. Retreat was then initiated, and sediment deposition was activated at various stages of this retreat process. This experimental design allowed for an assessment of how changing grounding line velocities, resulting from progressive retreat, impacted GZW geometry and the potential for grounding line stabilization. By varying the timing of sediment deposition, we aimed to determine the critical ice dynamics conditions necessary for GZW formation under these idealized settings, which would allow for the determination of a threshold at which runaway retreat precluded sediment accumulation and landform development.

We find that ice dynamics also influence GZW geometry, though their impact is significantly less pronounced than that of the sediment-related parameters described above. Grounding line velocity exhibits a modest positive correlation with GZW amplitude, increasing approximately 20 cm for every 10 m/yr increase. The width of constructed GZWs remains largely unaffected by changes in ice dynamics within the modeled parameters space. Critically, the model demonstrates the threshold beyond which rapid ice retreat, characterized by grounding line velocities exceeding approximately 670 m/yr, prevents meaningful sediment accumulation and therefore inhibits GZW formation (Figure 4.4). Under these conditions, sediment is dispersed over a wider area rather than accumulating to form a distinct landform (Figure 4.5).

These findings underscore the complex interplay between ice dynamics and sediment processes in controlling GZW development.

4.4 Discussion and future work

The model simulates GZW formation through the gradual deposition of sediment on the ice-distal side, consistent with horizontal and seaward expansion of GZWs observed in seismic data. Adjusting the stoss angle in our experiments allows for an investigation into how variations in sediment characteristics affect the geometry and timing of GZW construction. The stoss angle, influenced by factors such as grain shape and cohesion (Willibald et al., 2020), can be linked to subglacial hydrology may be further elucidated by examining sediment cores over GZWs and by directly comparing metrics with previously published GZWs in the high-latitudes (Batchelor & Dowdeswell, 2015).

Model results underscore the pivotal role of the depth of the deformable layer in shaping GZW geometry. A strong relationship was observed between GZW dimensions, sediment flux, and the timing of stability, with the grounding line advancing slowly over the constructed GZWs (Figure 4.3). The depth of the deformable layer emerged as a primary driver of sediment flux, significantly influencing the overall geometry of the GZWs. Our findings indicate that the formation of large-scale GZWs requires more than just stability, a sufficient thickness of the deformable layer is necessary to accommodate the substantial sediment accumulation required for GZW development.

Some limitations of the model include its omission of sediment delivery through subglacial and englacial channels, which may underestimate the importance of a robust subglacial hydrological system in transporting sufficient sediment to the grounding line. Additionally, the current version of the model does not account for the sub-ice shelf melt-out of subglacial debris, which has been suggested as a significant sediment input for the formation of some GZWs (Batchelor & Dowdeswell, 2015; Jones et al., 2021). Furthermore, due to the one-dimensional nature of the model, it does not consider the width of the troughs in which GZWs are observed. As a result, it cannot account for the influence of trough width on grounding line stability, despite the role of confined troughs in providing lateral drag that promotes stability (Jamieson et al., 2014).

Initial results from our model are promising, demonstrating its utility in assessing local factors, such as slope and height of the deformable layer, on GZW geometry. The model successfully recreated the characteristic asymmetric shape of GZWs, featuring a gently landward-dipping topset and a more steeply seaward-dipping foreset, with adjustable degrees of slumping failure. While this is effective on a local scale, integrating this model with three-dimensional models across larger portions of Antarctica remains a challenge. Future work should aim to incorporate more environmental variables and climate forcings to better understand the variability of factors influencing landform geometry and ice stream stability.

The model runs are based on idealized settings, not specific ice streams, aiming to examine observable GZW characteristics such as amplitude, width, stoss angle, and local bed slope. Yet, even idealized topography and glaciology are useful in understanding processes and responses such as those of Robel et al., (2022) showing the role of slight changes in bed slope as an important factor in determining grounding line ice flux. The lack of measurements for the depth of the deformable layer and sediment fluxes for paleo-ice streams means the model serves as an inversion method. Rather than inputting specific parameters to predict GZW geometry, the

model tests various parameters to match observed geometries, inferring potential controls and providing estimates for unknown factors like sediment flux and ice dynamics during landform formation. The derived sediment fluxes help estimate occupation time and provide further insights into the controls that can stabilize glaciers and the consequent construction of landforms.

Constraining the ages of individual groundings remains problematic, requiring detailed stratigraphic analyses due to the difficulty in acquiring radiocarbon-rich material from key paleo-ice stream locations (Bart et al., 2017). The inventory of large-scale GZWs provided by Batchelor and Dowdeswell (2015) shows inconsistencies in the reported dimensions. Further work is needed to assemble a complete inventory that allows for direct comparison of GZW dimensions and the factors influencing their formation.

Once a complete inventory is achieved, the duration of a standstill can be calculated by inferring sediment flux across the grounding line and the volume of the GZW, both based on the model. Alternatively, with a known volume and duration of stability, we could deduce sediment flux at the grounding line. The sediment flux will depend on factors such as sediment type, water depth, and ice dynamics, requiring tuning for different locations.

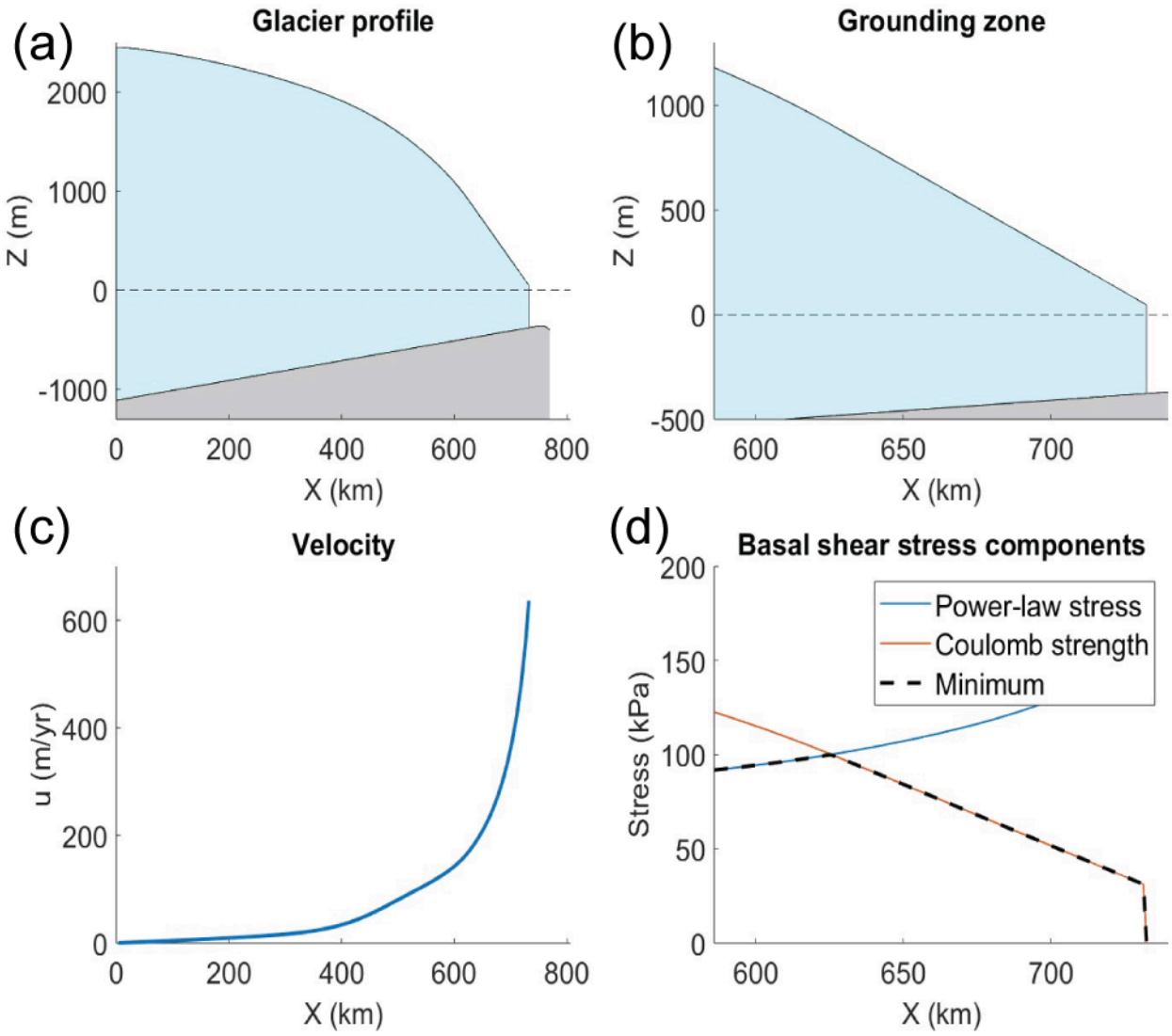

Figure 4.1. (A) Steady-state ice stream profile, **(B)** zoomed-in at the grounding zone. **(C)** Horizontal ice velocity profile. **(D)** Transition from power-law inland to Coulomb-plastic near the grounding zone.

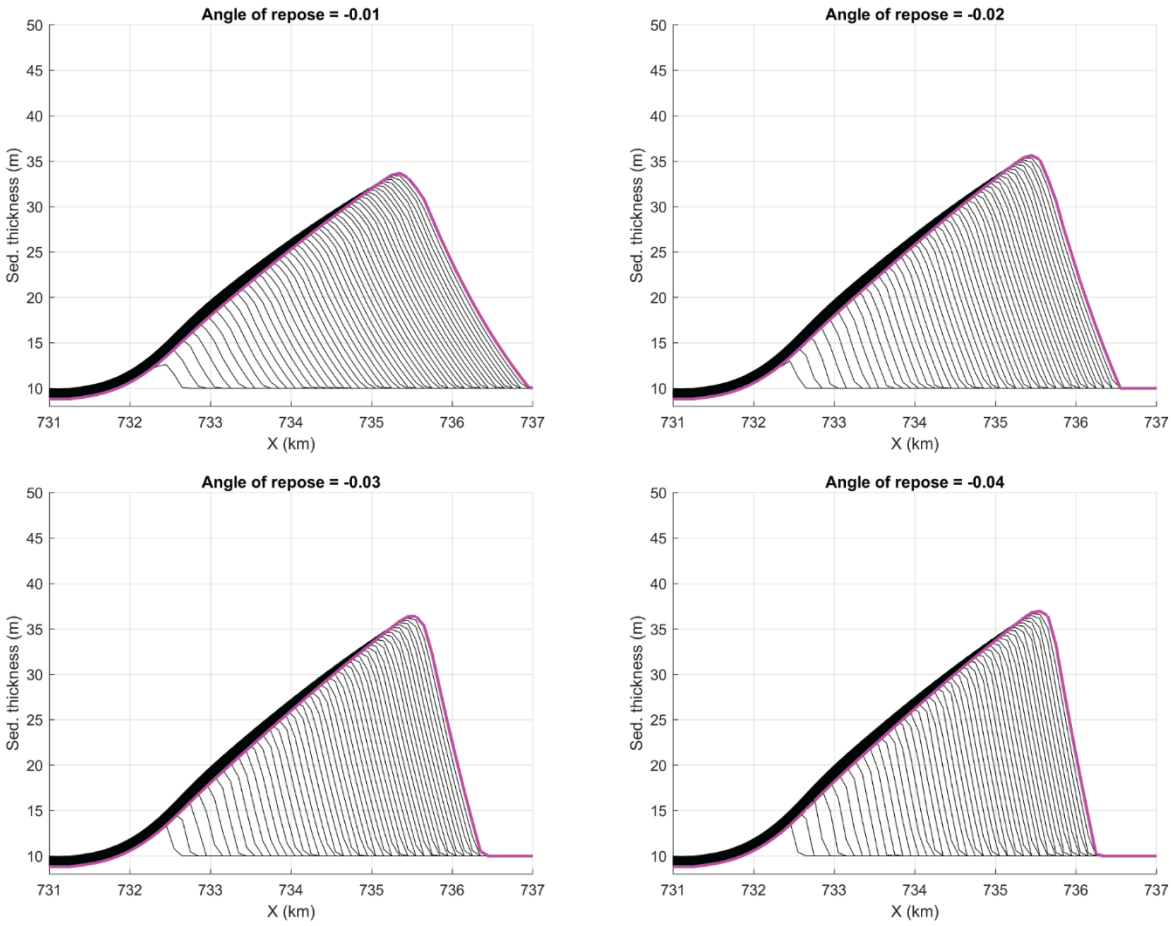

Figure 4.2. Plots illustrating the size difference of the constructed GZW based on varying stoss angles **(A)** -0.01 degrees **(B)** -0.02 degrees, **(C)** -0.03 degrees, **(D)** -0.04 degrees. Ice dynamics, bed slope, and depth of deformable layer (25 cm) held constant. Model ran for 1 kyr at 10 yr time steps. 20 yr increments shown in plots as successive black lines.

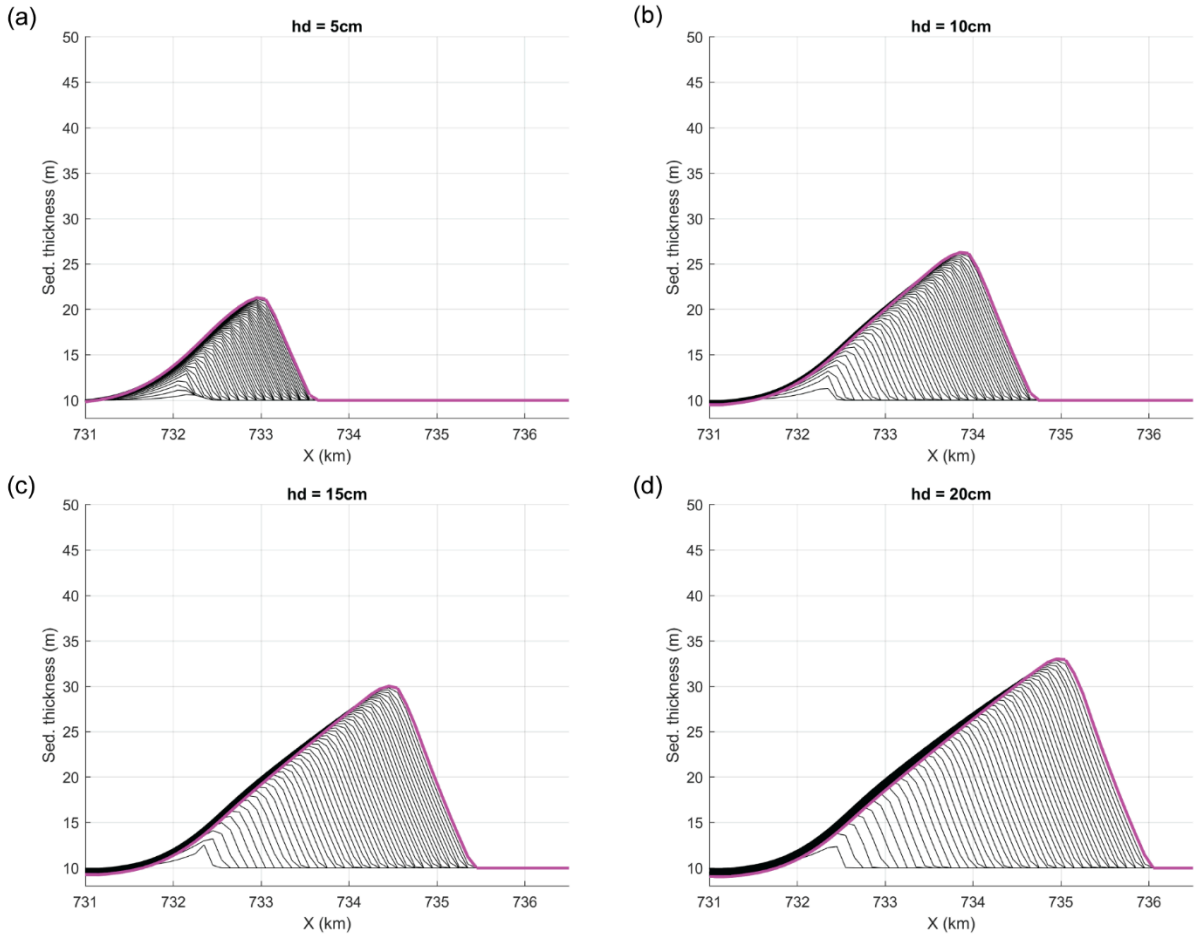

Figure 4.3. Plots illustrating the size difference of the constructed GZW based on the depth of the deformable layer parameter. **(A)** 5 cm, **(B)** 10 cm, **(C)** 15 cm, **(D)** 20 cm. Ice dynamics, bed slope, and stoss angle (0.02) held constant. Model ran for 1 thousand years at 10 year time steps. 20 year increments shown in plots as successive black lines.

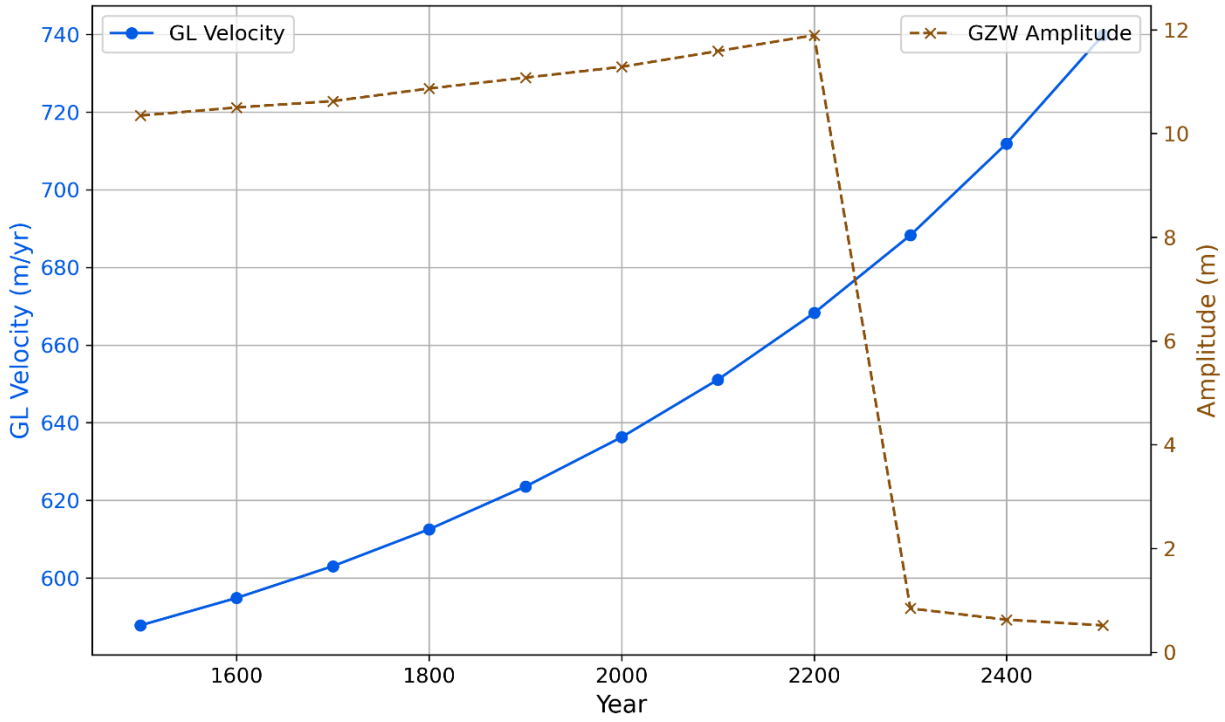

Figure 4.4. Impact of grounding line velocity on GZW formation. The blue line indicates the evolution of grounding line velocity (m/yr; shown on the left y-axis) over time as retreat advances. Brown line depicts amplitude (m; shown on the right y-axis) of constructed GZW.

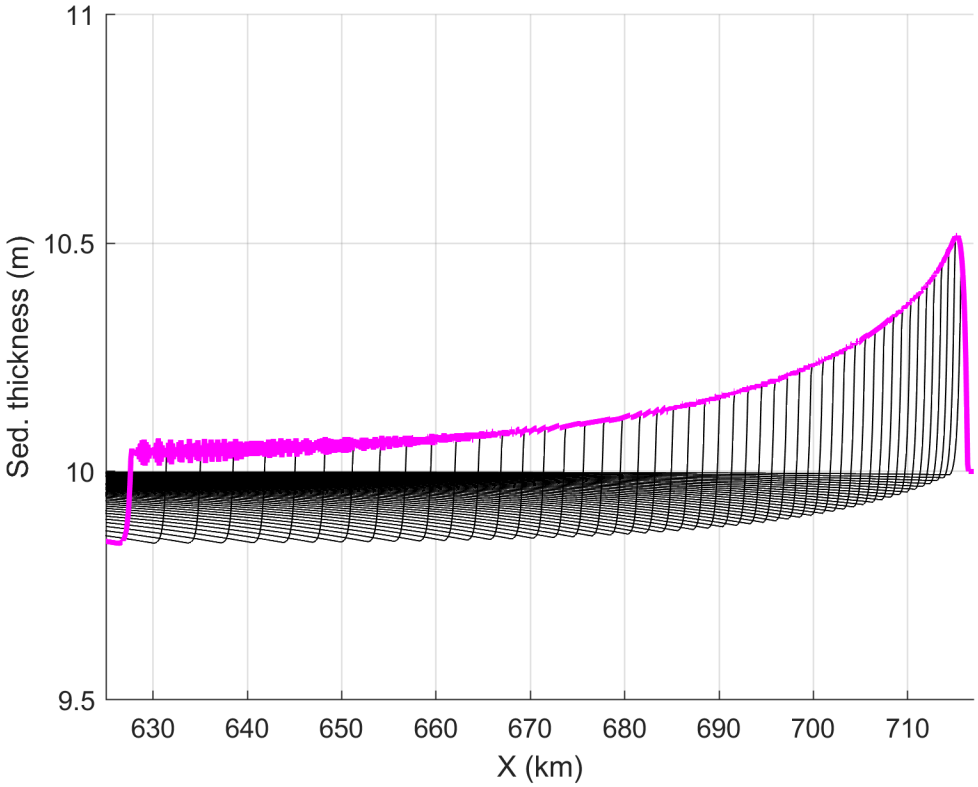

Figure 4.5. Model run for time step 22 kyr after retreat from steady state, illustrating example of complete instability, where high grounding line velocities do not allow the vertical deposition of sediment. Note differences in ranges for x- and y-axes compared to Figures 4.2 and 4.3.

Chapter 5: Concluding Remarks

5.1 Dissertation summary

This dissertation provides novel insights into the complex interplay between ice dynamics, subglacial processes, and landform evolution in paleo-ice stream environments. By leveraging high-resolution bathymetry, this study offers a unique perspective on local-scale controls that have been largely overlooked. The integrated approach of landforms analysis, morphometric characterization, and process-based modeling advances our understanding of ice sheet behavior and stability. These findings contribute to the development of more accurate ice sheet models, ultimately improving prediction of future sea-level rise.

Chapter 2 investigates the complex relationship between subglacial bed roughness, ice dynamics, and geological processes. By analyzing bed roughness across diverse glacial and deglaciated environments, this study highlights the significant influence of methodology, scale, and subglacial landforms in roughness quantification. The standard deviations method proves effective in revealing spatial patterns of bed roughness, crucial for interpreting ice stream behavior. However, limitation due to low-resolution topography especially in glaciated regions, underscore the challenges in accurately evaluating subglacial bed roughness and potential misrepresentation of basal motion in numerical ice sheet models. Key findings include the dominant role of ice flow direction in shaping bed roughness patterns, the complex relationship between low roughness values and assumed ice dynamics, and the strong correlation between roughness spikes and geological structures. This study reveals that while subglacial meltwater channels contribute to elevated roughness, they also facilitate ice flow, complicating the relationship between roughness and basal shear stress. Comparisons between paleo-ice stream beds in Amundsen Sea Embayment demonstrate the impact of sedimentary processes on bedform development and roughness characteristics.

High-resolution bathymetry is once again used in Chapter 3 to demonstrate the efficacy of automated landform identification in characterizing subglacial bed morphology and inferring glacial retreat patterns. Through the analysis of a large-dataset of ice-marginal landforms, the study reveals a strong correlation between local bed slope and landform morphology, suggesting that steeper slopes inhibit sediment accumulation and promote grounding line instability. While the presence of both moraines and grounding zone wedges (GZWs) indicates a complex retreat history, the predominance of moraine-like features suggests a more frequency occurrence of steady retreat. Key findings include the significant influence of local bed slope on landform dimension and the potential role of long-term climate variability in controlling the spacing between landforms. This work challenges the view of GZWs as exclusive indicators of episodic retreat, proposing a more nuanced interpretation that incorporates periods of steady retreat characterized by the formation of recessional moraines. These results contribute to a deeper understanding of ice-marginal landform formation and the dynamics of grounding line retreat.

Building upon the detailed analysis of small-scale ice-marginal landforms in Chapter 3, Chapter 4 shifts focus to a process-based model to investigate the formation of large-scale GZWs. The novel model introduced in this chapter investigates the interplay between local factors, ice dynamics, and sediment processes. The model successfully reproduces the characteristic asymmetric shape of GZWs and highlights the critical role of local bed slope, sediment flux, and ice dynamics in controlling GZW geometry and formation time. To further explore the controls on GZW geometry, the model was used to investigate the impact of

sediment stoss angle, the depth of the deformable layer, and ice dynamics in the form of grounding line velocity at the time of landform formation. Results indicate that the depth of the subglacial deformable layer, a proxy for sediment flux, strongly impacts GZW geometry, with deeper layers resulting in larger GZWs. Ice dynamics also influence GZW formation, but their role is more complex. Extreme grounding line velocities can entirely prevent sediment accumulation, hindering GZW development. Further research is needed to identify the specific conditions that allow for grounding line stabilization and subsequent GZW formation amidst rapid retreat. Results from this work emphasize the importance of a robust subglacial hydrology system in delivering sufficient sediment to the grounding line for GZW construction.

5.2 Future directions

5.2.1 Integrating Bed Roughness Observations to Constrain Ice Flow Modeling and Landform Analysis

Findings from Chapter 2 serve as a critical building block for the subsequent chapters, providing methodologies and insights into the role of bed roughness in glacial systems. By combining the findings from all three chapters, we can develop a more comprehensive understanding of the processes controlling ice-marginal landform formation and evolution. Importantly, the methodology developed in Chapter 2 to quantify bed roughness at multiple scales can be directly applied to the automated landform identification process in Chapter 3. The fractal nature of bed topography necessitates careful consideration of scale when defining landform boundaries and calculating morphometric properties. By drawing on the insights from Chapter 2, we can optimize the scale at which bed slope is measured, thereby enhancing the accuracy and robustness of the relationship between local bed slope and landform morphology established in Chapter 3.

Additionally, Chapter 2 revealed the critical influence of bedrock composition on bed roughness and, consequently, ice dynamics. The presence of features such as deep pockets of unconsolidated sediments, subglacial meltwater channels, or eroded crystalline bedrock significantly impacts roughness values and basal shear stress. The strong correlation between bed roughness and geological structures observed in Chapter 2 further emphasizes the importance of incorporating detailed rheological information into the model described in Chapter 4 to accurately represent subglacial conditions. By considering the diverse geological characteristics of the subglacial environment, including bed topography composition and structure, we can improve the ability of the model to predict sediment, landform formation, and ultimately retreat rates.

5.2.2 From Inferred Retreat Styles to Quantifiable Retreat Rates

While the morphometric analysis of Chapter 3 provides valuable insights into retreat patterns, a more comprehensive understanding would benefit from incorporating the ice dynamics of the individual-paleo ice streams that deposited the ice-marginal landforms considered. A critical limitation in reconstructing the deglacial history of paleo-ice streams in Antarctica is the lack of reliable, datable material due to factors such as poor carbonate preservation and contamination from glacially recycled carbon (Prothro et al., 2020). Consequently, precisely determining the formation timing of landforms remains difficult.

However, sediment core data from the western Ross Sea (Prothro et al., 2020; Figure A5.1) offers potential age constraints. Although sparse, these ages can be interpolated to estimate time of deposition, and retreat rates for the transects analyzed in Chapter 3. While a broader-scale analysis is needed, compared to our morphometric work, the established relationships between slope, spacing, and landform morphology can be leveraged to infer potential retreat rates for the paleo-ice streams in the western Ross Sea. This approach could shed light on the range of more frequent, localized retreat rate variations responsible for transitions between steady and episodic retreat styles, ultimately leading to the formation of the small-scale ice-marginal landforms identified in Chapter 3. These findings complement existing knowledge of larger-scale retreat patterns inferred from large-scale GZWs observed in deglaciated environments (Dowdeswell et al., 2016; Halberstadt et al., 2016).

5.2.3 Leveraging Morphometric Analysis for Improved Ice Flow Modeling

Similarly, a key next step in the development of Chapter 4 is to compile a comprehensive inventory of large-scale GZWs observed in the deglaciated continental shelf of Antarctica. We have found inconsistencies in the dimensions reported for GZWs in existing datasets, while many GZWs lack reported dimensions altogether. By utilizing-high resolution bathymetry, we can accurately measure GZW dimensions and determine the bed slope for each feature. This inventory will serve as a critical dataset for model testing, enabling us to simulate the formation of observed GZWs under varying paleo-ice stream conditions. By comparing simulated and observed GZW geometries, we can gain valuable insights into the factors controlling grounding line stability and occupation time.

The insights gained from the detailed analysis of ice-marginal landforms in Chapter 3 provide a crucial foundation for the process-based modeling described in Chapter 4. By establishing a robust correlation between local bed slope and landform morphology, we have identified a key control on sediment accumulation and grounding line stability. These findings can be directly incorporated into the model by parameterizing the relationship between bed slope, retreat rate, and landform morphology. Moreover, the emphasis on the complex interplay between moraines and GZWs highlights the need for a model capable of simulating both landform types under varying retreat scenarios. By incorporating the observed influence of long-term climate variability on landform spacing, the model can be further refined to capture the dynamic nature of ice-marginal environments.

Ultimately, the integration of these empirical observations into the model will enhance its predictive capabilities and allow for more realistic simulations of GZW formation and evolution under different paleo-ice stream conditions.

Appendix A2.

Table A2.1. Roughness values for channel features vs overall site.

Site	Method	Scale	Orientation	Channel mean	Site mean	Difference
1	SD	Local	Parallel	9 m	8 m	1 m
			Orthogonal	18 m	13 m	5 m
1	SD	Regional	Parallel	14 m	14 m	0 m
			Orthogonal	27 m	22 m	5 m
2	SD	Local	Parallel	20 m	18 m	2 m
			Orthogonal	27 m	25 m	2 m
2	SD	Regional	Parallel	34 m	33 m	1 m
			Orthogonal	39 m	40 m	-1 m
3	SD	Local	Parallel	22 m	20 m	2 m
			Orthogonal	25 m	23 m	2 m
3	SD	Regional	Parallel	34 m	33 m	1 m
			Orthogonal	39 m	38 m	1 m

Table A2.2. Comparison of roughness values between high-resolution bathymetry and BedMachine (BM).

Site	Method	Scale	Orientation	Range	Median	Range (BM)	Median (BM)
1	SD	Local	Parallel	61 m	5 m	120 m	8 m
			Orthogonal	110 m	10 m	100 m	10 m
1	SD	Regional	Parallel	120 m	9 m	140 m	11 m
			Orthogonal	200 m	15 m	160 m	14 m
1	FFT	Local	Parallel	3,700 m²	15 m²	16,100 m²	51 m²
			Orthogonal	9,500 m²	72 m²	9,900 m²	88 m²
1	FFT	Regional	Parallel	5,700 m²	18 m²	17,300 m²	52 m²
			Orthogonal	13,300 m²	80 m²	12,000 m²	85 m²
2	SD	Local	Parallel	87 m	16 m	150 m	19 m
			Orthogonal	85 m	22 m	130 m	21 m
2	SD	Regional	Parallel	190 m	28 m	190 m	26 m
			Orthogonal	180 m	34 m	220 m	29 m
2	FFT	Local	Parallel	5,810 m²	170 m²	22,000 m²	290 m²
			Orthogonal	7,830 m²	360 m²	15,900 m²	380 m²
2	FFT	Regional	Parallel	9,020 m²	210 m²	23,600 m²	310 m²
			Orthogonal	8,520 m²	420 m²	18,300 m²	400 m²
3	SD	Local	Parallel	74 m	17 m	160 m	19 m
			Orthogonal	130 m	19 m	160 m	21 m
3	SD	Regional	Parallel	160 m	28 m	180 m	27 m
			Orthogonal	240 m	29 m	250 m	28 m
3	FFT	Local	Parallel	5,600 m²	220 m²	28,200 m²	320 m²
			Orthogonal	16,700 m²	290 m²	22,900 m²	360 m²
3	FFT	Regional	Parallel	7,700 m²	250 m²	33,800 m²	330 m²
			Orthogonal	23,900 m²	290 m²	25,900 m²	360 m²
4	SD	Local	Parallel	35 m	2 m	39 m	3 m
			Orthogonal	35 m	3 m	46 m	3 m
4	SD	Regional	Parallel	70 m	3 m	55 m	4 m
			Orthogonal	57 m	4 m	62 m	4 m
4	FFT	Local	Parallel	1,200 m²	2 m²	1,600 m²	7 m²
			Orthogonal	1,200 m²	9 m²	2,200 m²	7 m²
4	FFT	Regional	Parallel	1,400 m²	2 m²	1,500 m²	7 m²
			Orthogonal	1,500 m²	9 m²	2,300 m²	7 m²

Table A2.3. Misrepresentation of BedMachine-derived roughness.

Site	Scale	Orientation	Mean (m)	Min (m)	Max (m)	Range (m)
1	Local	Parallel	4.4	-27	79	106
		Orthogonal	1.4	-47	72	119
1	Regional	Parallel	0.2	-100	120	220
		Orthogonal	-1.5	-101	73	174
2	Local	Parallel	4.9	-49	128	177
		Orthogonal	0.6	-74	100	174
2	Regional	Parallel	-0.3	-82	115	197
		Orthogonal	-4.1	-103	142	245
3	Local	Parallel	4.7	-54	119	173
		Orthogonal	3.2	-67	105	172
3	Regional	Parallel	0.2	-100	120	220
		Orthogonal	-2.3	-154	130	284
4	Local	Parallel	1.3	-18	25	43
		Orthogonal	-0.4	-14	27	41
4	Regional	Parallel	0.3	-34	38	73
		Orthogonal	-0.9	-23	30	53
5	Local	Parallel	5.4	-10	42	52
		Orthogonal	11.4	-7	55	62
5	Regional	Parallel	6.4	-31	70	101
		Orthogonal	11.7	-20	76	96
6	Local	Parallel	1.6	-27	36	63
		Orthogonal	5.9	-30	36	66
6	Regional	Parallel	3.2	-52	67	119
		Orthogonal	5	-87	64	150

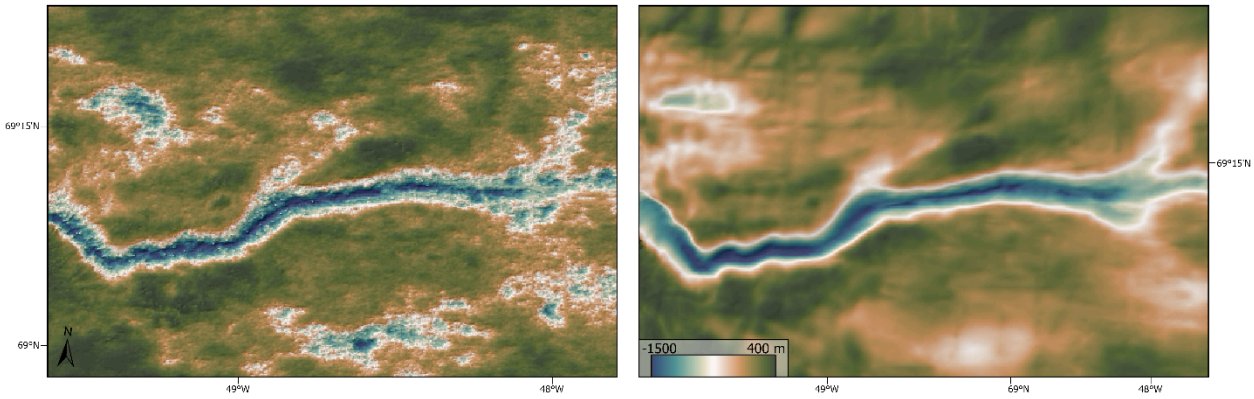

Figure A2.1. Elevation datasets at Jakobshavn Glacier. **(A)** First topographic realization from MacKie et al. (2021). **(B)** BedMachine (Morlighem et al., 2017).

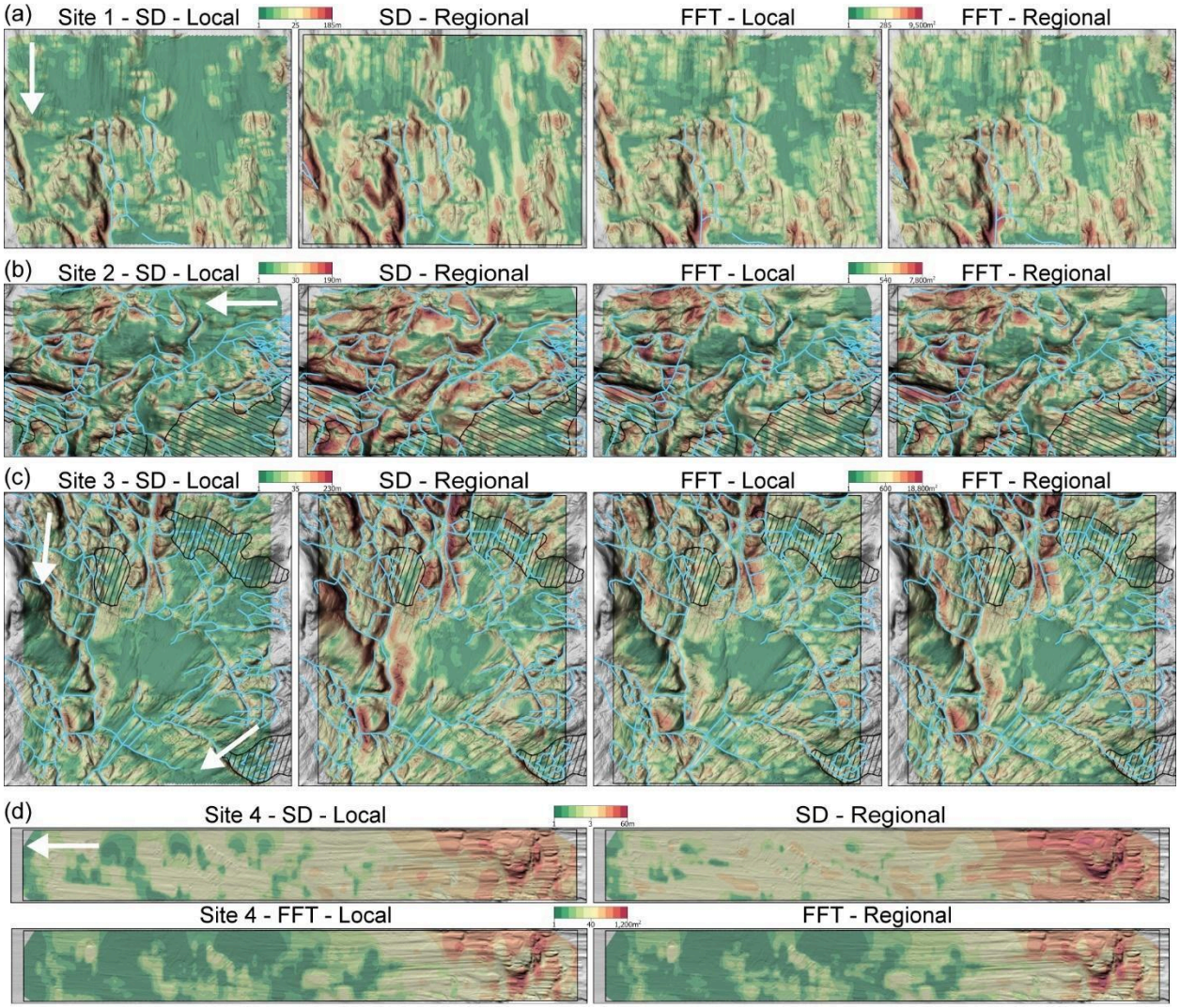

Figure A2.2. Absolute roughness measurements for orthogonal transects in sites 1-4 showing the difference in spatial distribution between scales and methods. White arrows indicate direction of paleo ice-flow.

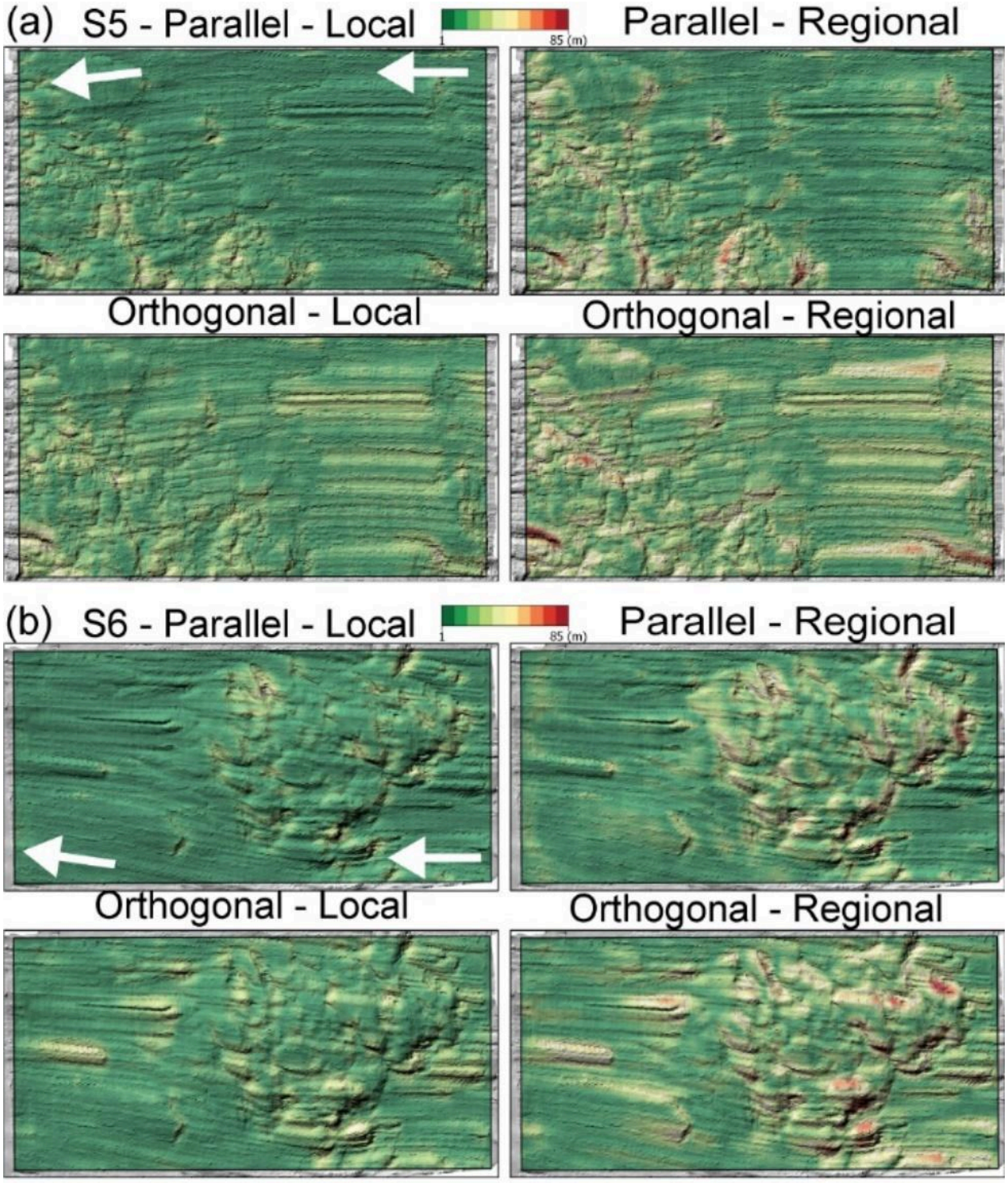

Figure A2.3. Absolute roughness measurements for parallel and orthogonal transects in sites 5-6 showing the difference in spatial distribution between scales. White arrows indicate direction of paleo-ice flow.

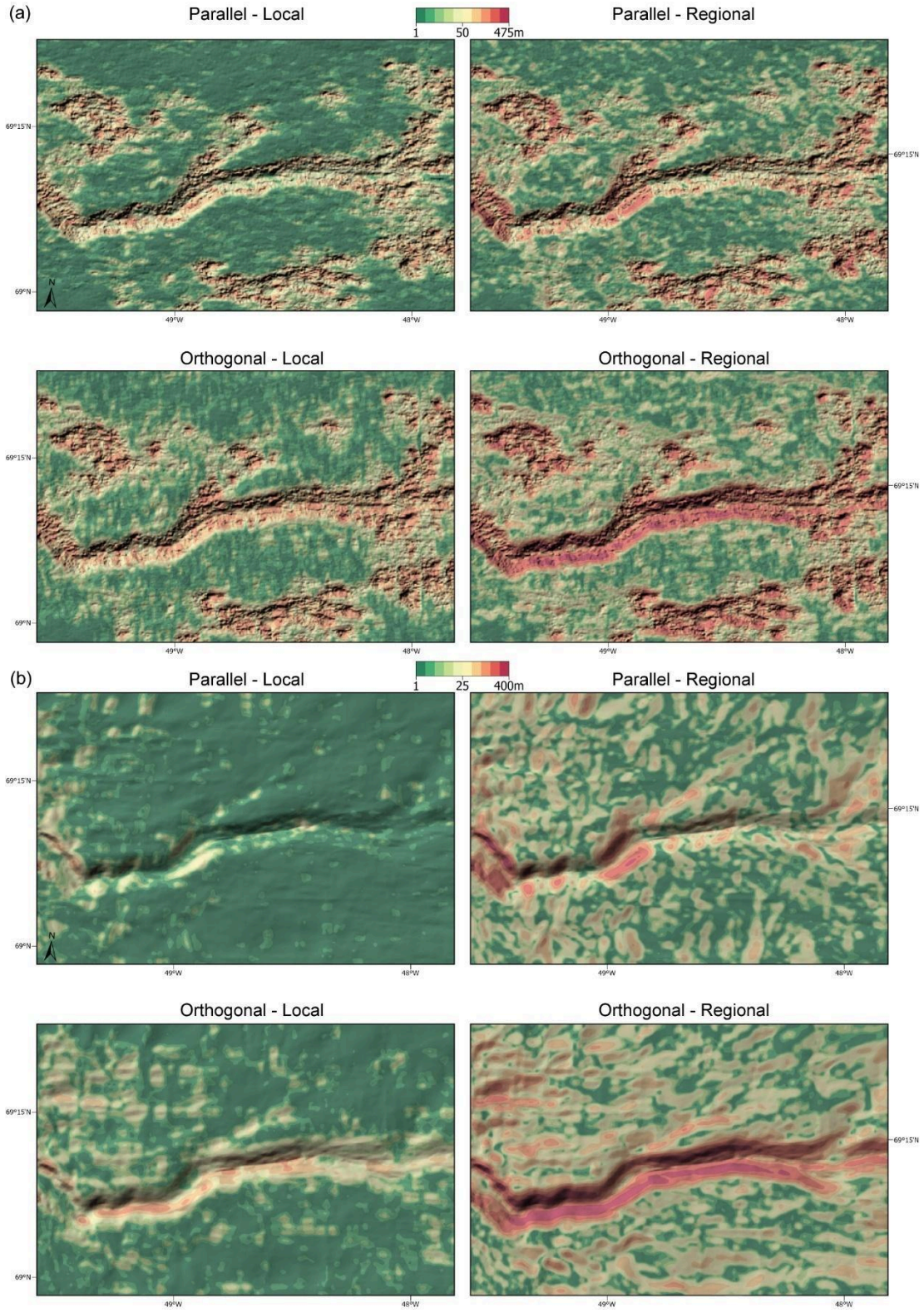

Figure A2.4. Absolute roughness measurements. **(A)** First topographic realization from Mackie et al. (2021), SD method. **(B)** SD Roughness from BedMachine dataset (Morlighem et al., 2017).

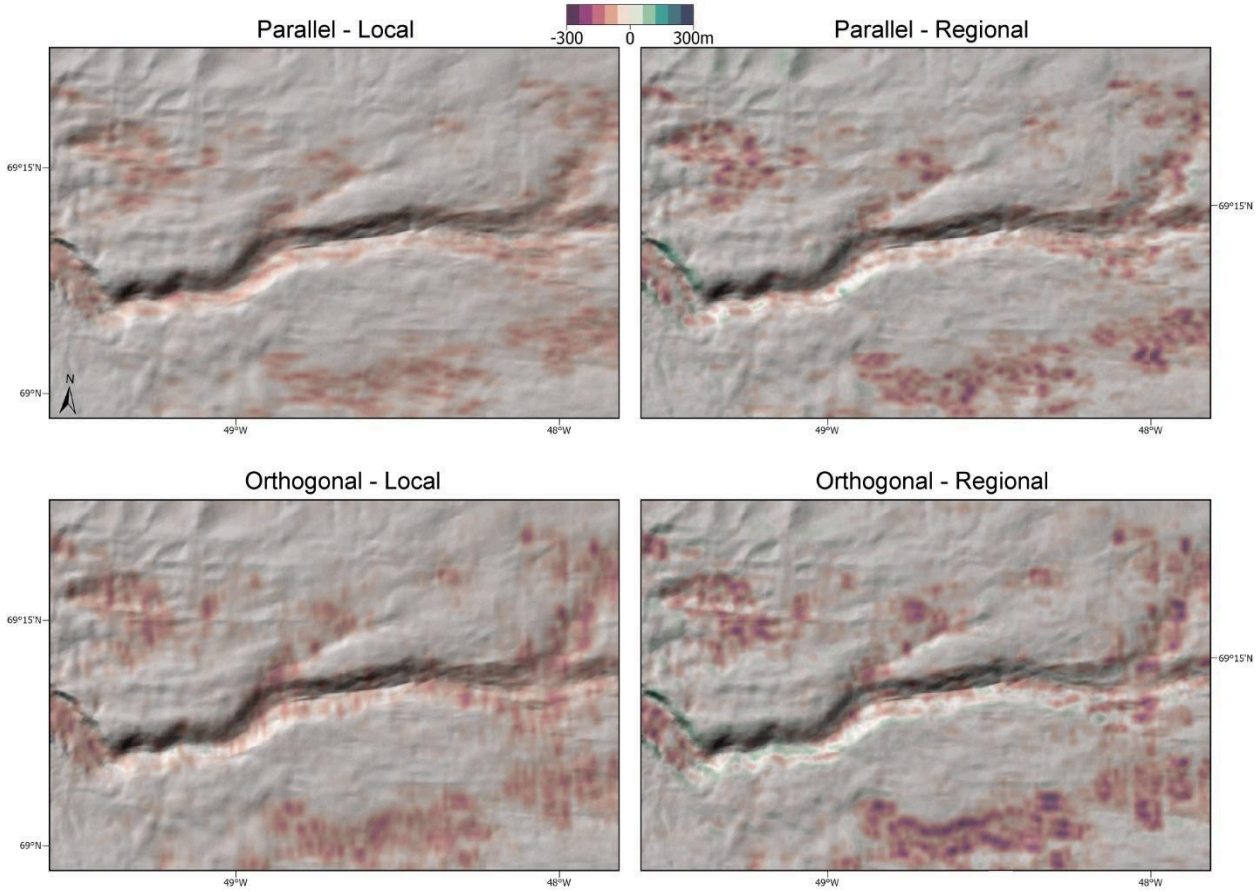

Figure A2.5. Difference in roughness measurements between topographic realization from Mackie et al. (2021) and BedMachine (Morlighem et al., 2017). BedMachine under-represents roughness in green-shaded areas.

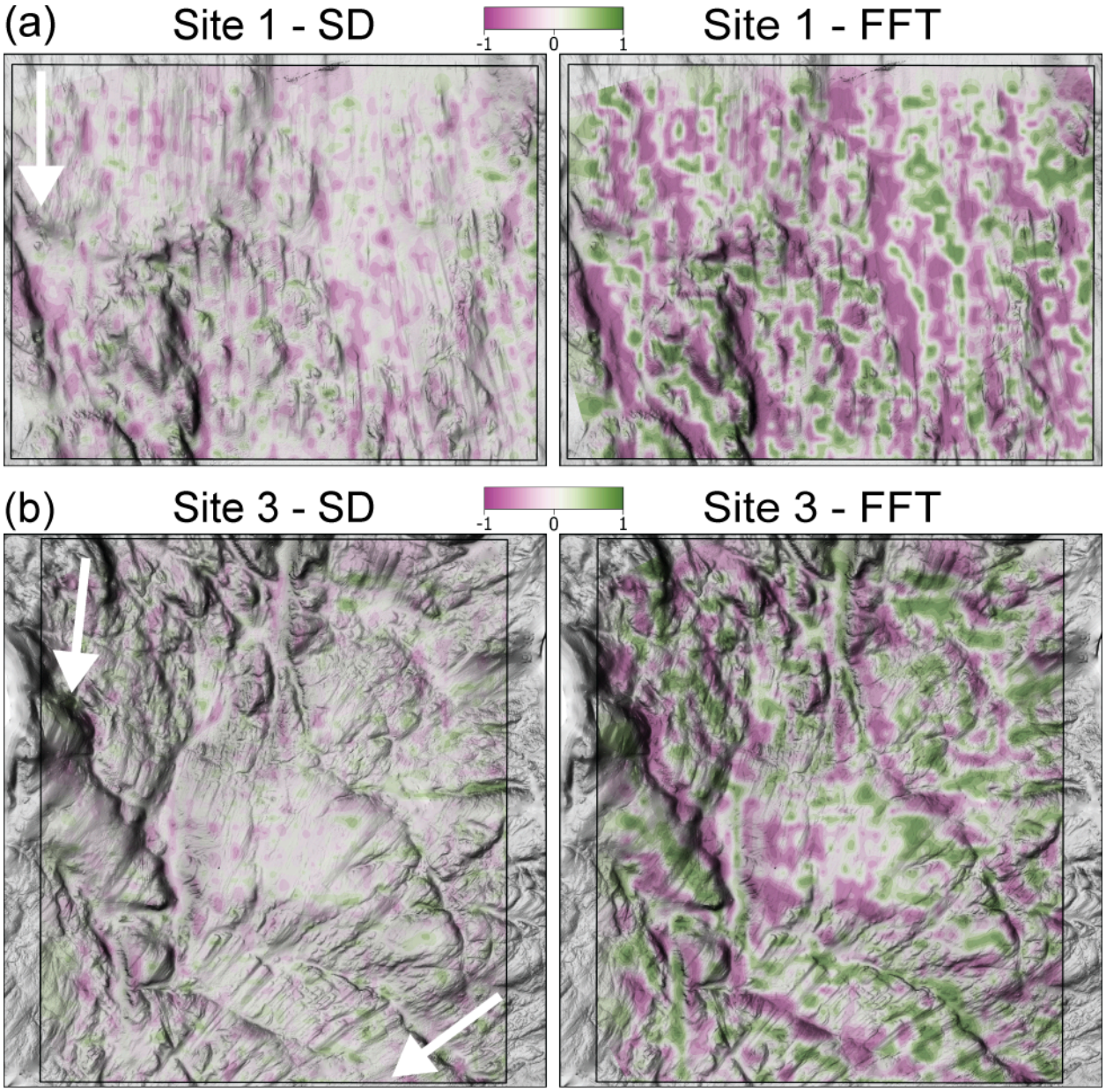

Figure A2.6. Anisotropy values calculated from the BedMachine dataset at every intersection point between parallel and orthogonal transects at site 1 **(A)** and site 3 **(B)** represent directionality of roughness measurements at the local scale. Orthogonal roughness dominates in the purple shades, parallel dominates in the green. White indicate isotropic or random surfaces.

Appendix A3

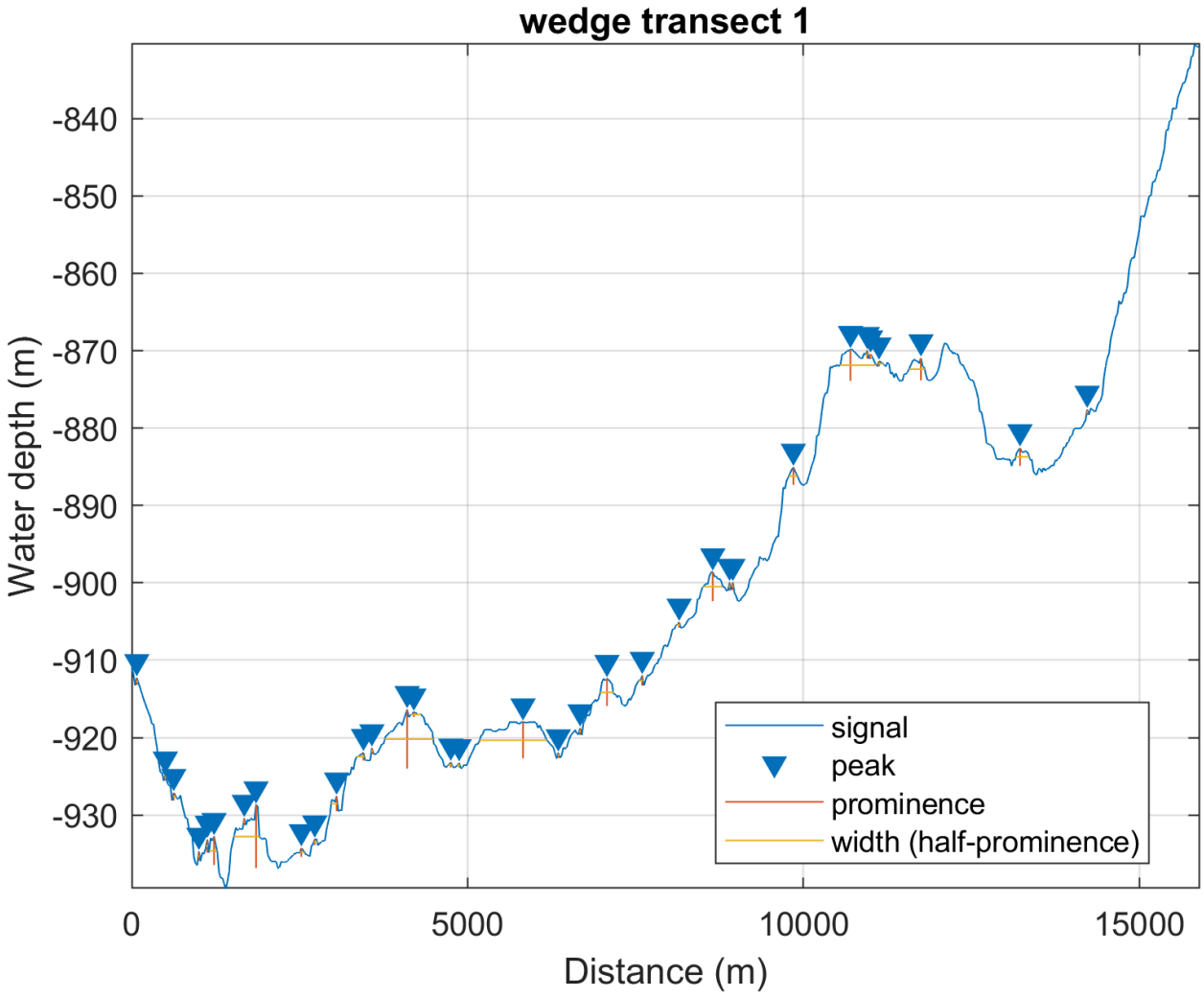

Figure A3.1. Example transect illustrating landforms identified along a GZW transect. Amplitude and width properties are denoted by the red and yellow lines, respectively. The cross-sectional area is computed by multiplying amplitude by width. Width-to-amplitude ratio is computed by dividing width by amplitude, with higher values signifying greater asymmetry.

Appendix A5

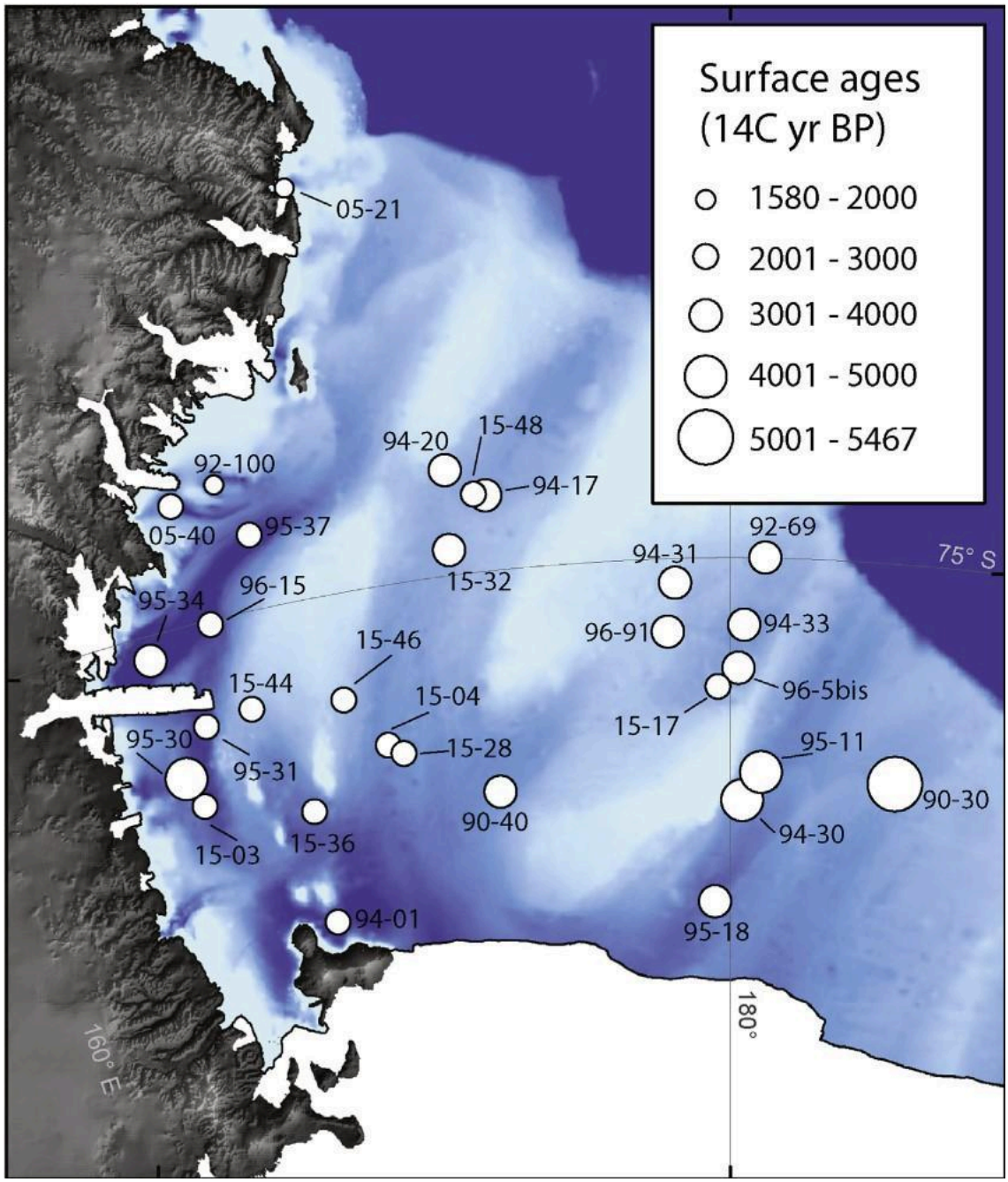

Figure A5.1. Figure from Prothro et al. (2020) showing the distribution of surface ages. Relative ages are represented by the size of core marker.

References

Alley, R. B., Blankenship, D. D., Bentley, C. R., & Rooney, S. T. (1986). Deformation of till beneath ice stream B, West Antarctica. *Nature*, 322(6074), 57–59. https://doi.org/10.1038/322057a0

Alley, R. B., Blankenship, D. D., Bentley, C. R., & Rooney, S. T. (1987). Till beneath ice stream B: 3. Till deformation: Evidence and implications. *Journal of Geophysical Research: Solid Earth*, 92(B9), 8921–8929. https://doi.org/10.1029/jb092ib09p08921

Alley, R. B. (1989). Water-pressure coupling of sliding and bed deformation: II. Velocity-depth profiles. *Journal of Glaciology*, 35(119), 119–129. https://doi.org/10.3189/002214389793701518

Alley, R. B., Anandakrishnan, S., Dupont, T. K., Parizek, B. R., & Pollard, D. (2007). Effect of sedimentation on ice-sheet grounding-line stability. *Science, 315*(5820), 1838–1841. https://doi.org/10.1126/science.1138396

Alley, R. B., Holschuh, N., MacAyeal, D. R., Parizek, B. R., Zoet, L., Riverman, K., Muto, A., Christianson, K., Clyne, E., Anandakrishnan, S., Stevens, N., & GHOST Collaboration. (2021). Bedforms of Thwaites Glacier, West Antarctica: Character and origin. *Journal of Geophysical Research: Earth Surface*, 126, e2021JF006339. https://doi.org/10.1029/2021JF006339

Alonso, B., Anderson, J. B., Díaz, J. I., & Bartek, L. R. (1992). Pliocene-Pleistocene seismic stratigraphy of the Ross Sea: Evidence for multiple ice sheet grounding episodes. In *Contributions to Antarctic Research III* (pp. 93–103). American Geophysical Union. https://doi.org/10.1029/ar057p0093

Anandakrishnan, S., Catania, G. A., Alley, R. B., & Horgan, H. J. (2007). Discovery of Till Deposition at the Grounding Line of Whillans Ice Stream. *Science*, 315(5820), 1835–1838. https://doi.org/10.1126/science.1138393

Anderson, J. B., Shipp, S. S., Lowe, A. L., Wellner, J. S., & Mosola, A. B. (2002). The Antarctic Ice Sheet during the Last Glacial Maximum and its subsequent retreat history: a review. *Quaternary Science Reviews, 21*(1–3), 49–70. https://doi.org/10.1016/s0277-3791(01)00083-x

Anderson, J. B., Simkins, L. M., Bart, P. J., De Santis, L., Halberstadt, A. R. W., Olivo, E., & Greenwood, S. L. (2018). Seismic and geomorphic records of Antarctic Ice Sheet evolution in the Ross Sea and controlling factors in its behaviour. *Geological Society, London, Special Publications, 475*(1), 223–240. https://doi.org/10.1144/sp475.5

Arthern, R. J., Hindmarsh, R. C. A., & Williams, C. R. (2015). Flow speed within the Antarctic ice sheet and its controls inferred from satellite observations. *Journal of Geophysical Research: Earth Surface, 120*(7), 1171-1188. https://doi.org/10.1002/2014JF003239

Bamber, J. L., Vaughan, D. G., & Joughin, I. (2000). Widespread complex flow in the interior of the Antarctic Ice Sheet. *Science, 287*(5456), 1248–1250. https://doi.org/10.1126/science.287.5456.1248

Bamber, J., Oppenheimer, M., Kopp, R., Aspinall, W., & Cooke, R. M. (2019). Ice sheet contributions to future sea-level rise from structured expert judgment. *Proceedings of the National Academy of Sciences, 116*(23), 11195-11200. https://doi.org/10.1073/pnas.1817205116

Bart, P. J., Krogmeier, B. J., Bart, M. P., & Tulaczyk, S. (2017). The paradox of a long grounding during West Antarctic Ice Sheet retreat in Ross Sea. *Scientific Reports, 7*, 1262. https://doi.org/10.1038/s41598-017-01329-8

Batchelor, C. L., & Dowdeswell, J. A. (2015). Ice-sheet grounding-zone wedges (GZWs) on high-latitude continental margins. *Marine Geology, 363*, 65–92. https://doi.org/10.1016/j.margeo.2015.02.001

Bell, R. E., Blankenship, D. D., Finn, C. A., Morse, D. L., Scambos, T. A., Brozena, J. M., & Hodge, S. M. (1998). Influence of subglacial geology on the onset of a West Antarctic ice stream from aero-geophysical observations. *Nature, 394*, 58-62. https://doi.org/10.1038/27883

Benn, D., & Evans, D. J. A. (2014). *Glaciers and Glaciation* (2nd ed.). Routledge. https://doi.org/10.4324/9780203785010

Bennet, M. R., & Glasser, N. F. (1996). *Glacial geology: Ice sheets and landforms*. John Wiley & Sons Ltd., Chichester, UK, 153.

Bennett, M. R. (2003). Ice streams as the arteries of an ice sheet: their mechanics, stability and significance. *Earth-Science Reviews, 61*(3–4), 309–339. https://doi.org/10.1016/S0012-8252(02)00130-7

Bingham, R. G., & Siegert, M. J. (2007). Radar-derived bed roughness characterization of Institute and Möller ice streams, West Antarctica, and comparison with Siple Coast ice streams. *Geophysical Research Letters, 34*(21). https://doi.org/10.1029/2007GL031483

Bingham, R. G., & Siegert, M. J. (2009). Quantifying subglacial bed roughness in Antarctica: Implications for ice-sheet dynamics and history. *Quaternary Science Reviews, 28*(3-4), 223-236. https://doi.org/10.1016/j.quascirev.2008.10.014

Bingham, R. G., Vaughan, D. G., King, E. C., Davies, D., Cornford, S. L., Smith, A. M., Arthern, R. J., Brisbourne, A. M., De Rydt, J., Graham, A. G. C., Spagnolo, M., Marsh, O. J., & Shean, D. E. (2017). Diverse landscapes beneath Pine Island Glacier influence ice flow. *Nature Communications, 8*, 1618. https://doi.org/10.1038/s41467-017-01597-y

Bjarnadóttir, L. R., Rüther, D. C., Winsborrow, M. C. M., & Andreassen, K. (2012). Grounding-line dynamics during the last deglaciation of Kveithola, W Barents Sea, as revealed by seabed geomorphology and shallow seismic stratigraphy. *Boreas*. https://doi.org/10.1111/j.1502-3885.2012.00273.x

Blankenship, D. D., Bentley, C. R., Rooney, S. T., & Alley, R. B. (1987). Till beneath ice stream B: 1. Properties derived from seismic travel times. *Journal of Geophysical Research: Solid Earth*, 92(B9), 8903–8911. https://doi.org/10.1029/jb092ib09p08903

Boulton, G. (1986). Geophysics: A paradigm shift in glaciology?. *Nature*, 322, 18. https://doi.org/10.1038/322018a0

Boulton, G. S. (1996). The origin of till sequences by subglacial sediment deformation beneath mid-latitude ice sheets. *Annals of Glaciology*, 22, 75–84. https://doi.org/10.3189/1996AoG22-1-75-84

Christian, J. E., Catania, G., Munevar Garcia, S., Robel, A., Miller, L., & Stearns, L. (in prep). Experiments with a coupled ice-flow and sediment-transport model: Grounding-zone wedge formation and effects on ice-stream stability.

Cooper, M. A., Jordan, T. M., Schroeder, D. M., Siegert, M. J., Williams, C. N., & Bamber, J. L. (2019). Subglacial roughness of the Greenland Ice Sheet: Relationship with contemporary ice velocity and geology. *The Cryosphere, 13*, 3093-3115. https://doi.org/10.5194/tc-13-3093-2019

De Angelis, H., & Skvarca, P. (2003). Glacier surge after ice shelf collapse. *Science, 299*, 1560-1562. doi: 10.1126/science.1077987

DeConto, R. M., Pollard, D., Alley, R. B., Velicogna, I., Gasson, E., Gomez, N., Sadai, S., Condron, A., Gilford, D. M., Ashe, E. L., Kopp, R. E., Li, D., & Dutton, A. (2021). The Paris Climate Agreement and future sea-level rise from Antarctica. *Nature, 593*, 83-89. https://doi.org/10.1038/s41586-021-03427-0

De Santis, L. (1999). The Eastern Ross Sea continental shelf during the Cenozoic: implications for the West Antarctic ice sheet development. In Global and Planetary Change (Vol. 23, Issues 1–4, pp. 173–196). Elsevier BV. https://doi.org/10.1016/s0921-8181(99)00056-9

Dowdeswell, J. A., Ottesen, D., Evans, J., Ó Cofaigh, C., & Anderson, J. B. (2008). Submarine glacial landforms and rates of ice-stream collapse. *Geology, 36*(10), 819. https://doi.org/10.1130/g24808a.1

Dowdeswell, J. A., & Fugelli, E. M. G. (2012). The seismic architecture and geometry of grounding-zone wedges formed at the marine margins of past ice sheets. *Geological Society of America Bulletin, 124*(11–12), 1750–1761. https://doi.org/10.1130/b30628.1

Dowdeswell, J. A., Canals, M., Jakobsson, M., Todd, B. J., Dowdeswell, E. K., & Hogan, K. A. (2016). Introduction: an atlas of submarine glacial landforms. *Geological Society, London, Memoirs, 46*(1), 3–14. https://doi.org/10.1144/m46.171

Dowdeswell, J. A., Batchelor, C. L., Montelli, A., Ottesen, D., Christie, F. D. W., Dowdeswell, E. K., & Evans, J. (2020). Delicate seafloor landforms reveal past Antarctic grounding-line retreat of kilometers per year. In Science (Vol. 368, Issue 6494, pp. 1020–1024). American Association for the Advancement of Science (AAAS). https://doi.org/10.1126/science.aaz3059

Falcini, F. A. M., Rippin, D. M., Krabbendam, M., & Selby, K. A. (2018). Quantifying bed roughness beneath contemporary and palaeo-ice streams. *Journal of Glaciology, 64*(247), 822-834. https://doi.org/10.1017/jog.2018.71

Falcini, F. A. M., Krabbendam, M., Selby, K. A., & Rippin, D. M. (2021). Using bed-roughness signatures to characterise glacial landform assemblages beneath palaeo-ice sheets. *Journal of Glaciology, 68*(269), 518-532. https://doi.org/10.1017/jog.2021.122

Favier, L., Gagliardini, O., Durand, G., & Zwinger, T. (2012). A three-dimensional full Stokes model of the grounding line dynamics: effect of a pinning point beneath the ice shelf. *The Cryosphere, 6*(1), 101–112. https://doi.org/10.5194/tc-6-101-2012

Favier, L., Durand, G., Cornford, S. L., Gudmundsson, G. H., Gagliardini, O., Gillet-Chaulet, F., Zwinger, T., Payne, A. J., & Le Brocq, A. M. (2014). Retreat of Pine Island Glacier controlled by marine ice-sheet instability. *Nature Climate Change, 4*(2), 117-121. https://doi.org/10.1038/nclimate2094

Favier, L., Pattyn, F., Berger, S., & Drews, R. (2016). Dynamic influence of pinning points on marine ice-sheet stability: A numerical study in Dronning Maud Land, East Antarctica. *The Cryosphere, 10*, 2623–2635. https://doi.org/10.5194/tc-10-2623-2016

Graham, A. G. C., Larter, R. D., Gohl, K., Dowdeswell, J. A., Hillenbrand, C.-D., Smith, J. A., Evans, J., Kuhn, G., & Deen, T. (2010). Flow and retreat of the Late Quaternary Pine Island-Thwaites palaeo-ice stream, West Antarctica. *Journal of Geophysical Research: Earth Surface, 115*, F03025. https://doi.org/10.1029/2009JF001482

Graham, A. G. C., Dutrieux, P., Vaughan, D. G., Nitsche, F. O., Gyllencreutz, R., Greenwood, S. L., Larter, R. D., & Jenkins, A. (2013). Seabed corrugations beneath an Antarctic ice shelf revealed by autonomous underwater vehicle survey: Origin and implications for the

history of Pine Island Glacier. *Journal of Geophysical Research: Earth Surface, 118*, 1356–1366. https://doi.org/10.1002/jgrf.20087

Graham, A. G. C., Jakobsson, M., Nitsche, F. O., Larter, R. D., Anderson, J. B., Hillenbrand, C.-D., Gohl, K., Klages, J. P., Smith, J. A., & Jenkins, A. (2016). Submarine glacial-landform distribution across the West Antarctic margin, from grounding line to slope: The Pine Island-Thwaites ice-stream system. *Geological Society, London, Memoirs, 46*, 493-500. https://doi.org/10.1144/M46.173

Graham, A. G. C., Wåhlin, A., Hogan, K. A., Nitsche, F. O., Heywood, K. J., Totten, R. L., Smith, J. A., Hillenbrand, C.-D., Simkins, L. M., Anderson, J. B., Wellner, J. S., & Larter, R. D. (2022). Rapid retreat of Thwaites Glacier in the pre-satellite era. In Nature Geoscience (Vol. 15, Issue 9, pp. 706–713). Springer Science and Business Media LLC. https://doi.org/10.1038/s41561-022-01019-9

Greenwood, S. L., Gyllencreutz, R., Jakobsson, M., & Anderson, J. B. (2012). Ice-flow switching and East/West Antarctic Ice Sheet roles in glaciation of the western Ross Sea. *Geological Society of America Bulletin, 124*(11–12), 1736–1749. https://doi.org/10.1130/b30643.1

Greenwood, S. L., Simkins, L. M., Winsborrow, M. C. M., & Bjarnadóttir, L. R. (2021). Exceptions to bed-controlled ice sheet flow and retreat from glaciated continental margins worldwide. *Science Advances, 7*(3). https://doi.org/10.1126/sciadv.abb6291

Gudlaugsson, E., Humbert, A., Winsborrow, M., & Andreassen, K. (2013). Subglacial roughness of the former Barents Sea ice sheet. *Journal of Geophysical Research: Earth Surface*, 118, 2546–2556. https://doi.org/10.1002/2013JF002714

Halberstadt, A. R. W., Simkins, L. M., Greenwood, S. L., & Anderson, J. B. (2016). Past ice-sheet behaviour: retreat scenarios and changing controls in the Ross Sea, Antarctica. *The Cryosphere, 10*, 1003–1020. https://doi.org/10.5194/tc-10-1003-2016

Halberstadt, A. R. W., Simkins, L. M., Anderson, J. B., Prothro, L. O., & Bart, P. J. (2018). Characteristics of the deforming bed: Till properties on the deglaciated Antarctic continental shelf. *Journal of Glaciology, 64*(248), 1014–1027. https://doi.org/10.1017/jog.2018.92

Hansen, D. D., & Zoet, L. K. (2022). Characterizing Sediment Flux of Deforming Glacier Beds. *Journal of Geophysical Research: Earth Surface*, 127. https://doi.org/10.1029/2021JF006544

Hogan, K. A., Larter, R. D., Graham, A. G. C., Arthern, R., Kirkham, J. D., Totten, R. L., Jordan, T. A., Clark, R., Fitzgerald, V., Wåhlin, A. K., Anderson, J. B., Hillenbrand, C.-D., Nitsche, F. O., Simkins, L., Smith, J. A., Gohl, K., Arndt, J. E., Hong, J., & Wellner, J. (2020). Revealing the former bed of Thwaites Glacier using sea-floor bathymetry: Implications for warm-water routing and bed controls on ice flow and buttressing. *The Cryosphere, 14*(9), 2883-2908. https://doi.org/10.5194/tc-14-2883-2020

Holschuh, N., Christianson, K., Paden, J., Alley, R. B., & Anandakrishnan, S. (2020). Linking postglacial landscapes to glacier dynamics using swath radar at Thwaites Glacier, Antarctica. *Geology, 48*(3), 268-272. https://doi.org/10.1130/G46772.1

Iverson, N. R., & Zoet, L. K. (2015). Experiments on the dynamics and sedimentary products of glacier slip. *Geomorphology, 244*, 121-134. https://doi.org/10.1016/j.geomorph.2015.03.027

Jamieson, S. S. R., Vieli, A., Ó Cofaigh, C., Stokes, C. R., Livingstone, S. J., & Hillenbrand, C.-D. (2014). Understanding controls on rapid ice-stream retreat during the last

deglaciation of Marguerite Bay, Antarctica, using a numerical model. *Journal of Geophysical Research: Earth Surface, 119*, 247–263. https://doi.org/10.1002/2013JF002934

Jenkins, A., Shoosmith, D., Dutrieux, P., Jacobs, S., Kim, T. W., Lee, S. H., Ha, H. K., & Stammerjohn, S. (2018). West Antarctic Ice Sheet retreat in the Amundsen Sea driven by decadal oceanic variability. *Nature Geoscience, 11*(10), 733–738. https://doi.org/10.1038/s41561-018-0207-4

Jones, R. S., Gudmundsson, G. H., Mackintosh, A. N., McCormack, F. S., & Whitmore, R. J. (2021). Ocean-driven and topography-controlled nonlinear glacier retreat during the Holocene: Southwestern Ross Sea, Antarctica. *Geophysical Research Letters*, 48, e2020GL091454. https://doi.org/10.1029/2020GL091454

Jordan, T. A., Porter, D., Tinto, K., Millan, R., Muto, A., Hogan, K., Larter, R. D., Graham, A. G. C., & Paden, J. D. (2020). New gravity-derived bathymetry for the Thwaites, Crosson, and Dotson ice shelves revealing two ice shelf populations. *The Cryosphere, 14*(9), 2869-2882. https://doi.org/10.5194/tc-14-2869-2020

Joughin, I., Smith, B. E., & Schoof, C. G. (2019). Regularized Coulomb friction laws for ice sheet sliding: Application to Pine Island Glacier, Antarctica. *Geophysical Research Letters, 46*, 4764–4771. https://doi.org/10.1029/2019GL082526

Kamb, B. (1970). Sliding motion of glaciers: Theory and observation. *Reviews of Geophysics, 8*(4), 673-728. https://doi.org/10.1029/RG008i004p00673

Kavanaugh, J. L., & Clarke, G. K. C. (2006). Discrimination of the flow law for subglacial sediment using in situ measurements and an interpretation model. *Journal of Geophysical Research: Earth Surface*, 111(F1), F01002. https://doi.org/10.1029/2005JF000346

Kazmierczak, E., Sun, S., Coulon, V., & Pattyn, F. (2022). Subglacial hydrology modulates basal sliding response of the Antarctic ice sheet to climate forcing. *The Cryosphere, 16*(10), 4537–4552. https://doi.org/10.5194/tc-16-4537-2022

King, L. H., Rokoengen, K., Fader, G. B. J., & Gunleiksrud, T. (1991). Till-tongue stratigraphy. *Geological Society of America Bulletin, 103*(5), 637–659. https://doi.org/10.1130/0016-7606(1991)103<0637>2.3.co;2

Kirkham, J. D., Hogan, K. A., Larter, R. D., Arnold, N. S., Nitsche, F. O., Golledge, N. R., & Dowdeswell, J. A. (2019). Past water flow beneath Pine Island and Thwaites glaciers, West Antarctica. *The Cryosphere, 13*(7), 1959-1981. https://doi.org/10.5194/tc-13-1959-2019

Kyrke-Smith, T. M., Gudmundsson, G. H., & Farrell, P. E. (2018). Relevance of detail in basal topography for basal slipperiness inversions: A case study on Pine Island Glacier, Antarctica. *Frontiers in Earth Science, 6*. https://doi.org/10.3389/feart.2018.00033

Larter, R. D., Anderson, J. B., Graham, A. G. C., Gohl, K., Hillenbrand, C.-D., Jakobsson, M., Johnson, J. S., Kuhn, G., Nitsche, F. O., Smith, J. A., Witus, A. E., Bentley, M. J., Dowdeswell, J. A., Ehrmann, W., Klages, J. P., Lindow, J., Ó Cofaigh, C., & Spiegel, C. (2014). Reconstruction of changes in the Amundsen Sea and Bellingshausen Sea sector of the West Antarctic Ice Sheet since the Last Glacial Maximum. *Quaternary Science Reviews, 100*, 55-86. https://doi.org/10.1016/j.quascirev.2013.10.016

Law, R., Christoffersen, P., Mackie, E., Cook, S., Haseloff, M., & Gagliardini, O. (2023). Complex motion of Greenland Ice Sheet outlet glaciers with basal temperate ice. *Science Advances, 9*(6), eabq5180. https://doi.org/10.1126/sciadv.abq5180

Li, X., Sun, B., Siegert, M. J., Bingham, R. G., Tang, X., Zhang, D., Cui, X., & Zhang, X. (2010). Characterization of subglacial landscapes by a two-parameter roughness index. *Journal of Glaciology, 56*(199), 831-836. https://doi.org/10.3189/002214310794457326

Livingstone, S. J., Ó Cofaigh, C., Stokes, C. R., Hillenbrand, C.-D., Vieli, A., & Jamieson, S. S. R. (2012). Antarctic palaeo-ice streams. *Earth-Science Reviews, 111*(1–2), 90–128. https://doi.org/10.1016/j.earscirev.2011.10.003

Lowe, A. L., & Anderson, J. B. (2002). Reconstruction of the West Antarctic Ice Sheet in Pine Island Bay during the Last Glacial Maximum and its subsequent retreat history. *Quaternary Science Reviews, 21*(16-17), 1879-1897. https://doi.org/10.1016/S0277-3791(02)00006-9

Lowry, D. P., Golledge, N. R., Bertler, N. A. N., Jones, R. S., & McKay, R. (2019). Deglacial grounding-line retreat in the Ross Embayment, Antarctica, controlled by ocean and atmosphere forcing. *Science Advances, 5*(8). https://doi.org/10.1126/sciadv.aav8754

MacKie, E. J., Schroeder, D. M., Zuo, C., Yin, Z., & Caers, J. (2021). Stochastic modeling of subglacial topography exposes uncertainty in water routing at Jakobshavn Glacier. *Journal of Glaciology, 67*(261), 75-83. https://doi.org/10.1017/jog.2020.84

Morlighem, M., Williams, C. N., Rignot, E., An, L., Arndt, J. E., Bamber, J. L., Catania, G., Chauché, N., Dowdeswell, J. A., Dorschel, B., Fenty, I., Hogan, K., Howat, I., Hubbard, A., Jakobsson, M., Jordan, T. M., Kjeldsen, K. K., Millan, R., Mayer, L., Mouginot, J., Noël, B. P. Y., O'Cofaigh, C., Palmer, S., Rysgaard, S., Seroussi, H., Siegert, M. J., Slabon, P., Straneo, F., van den Broeke, M. R., Weinrebe, W., Wood, M., & Zinglersen, K. B. (2017). BedMachine v3: Complete Bed Topography and Ocean Bathymetry Mapping of Greenland From Multibeam Echo Sounding Combined With Mass Conservation. *Geophysical Research Letters*, 44(21). https://doi.org/10.1002/2017gl074954

Morlighem, M., Rignot, E., Binder, T., Blankenship, D., Drews, R., Eagles, G., Eisen, O., Ferraccioli, F., Forsberg, R., Fretwell, P., Goel, V., Greenbaum, J. S., Gudmundsson, H., Guo, J., Helm, V., Hofstede, C., Howat, I., Humbert, A., Jokat, W., Karlsson, N. B., Lee, W. S., Matsuoka, K., Millan, R., Mouginot, J., Paden, J., Pattyn, F., Roberts, J., Rosier, S., Ruppel, A., Seroussi, H., Smith, E. C., Steinhage, D., Sun, B., van den Broeke, M. R., van Ommen, T. D., van Wessem, M., & Young, D. A. (2020). Deep glacial troughs and stabilizing ridges unveiled beneath the margins of the Antarctic Ice Sheet. *Nature Geoscience, 13*, 132-137. https://doi.org/10.1038/s41561-019-0510-8

Mosola, A. B., & Anderson, J. B. (2006). Expansion and rapid retreat of the West Antarctic Ice Sheet in eastern Ross Sea: possible consequence of over-extended ice streams? *Quaternary Science Reviews*, 25(17–18), 2177–2196. https://doi.org/10.1016/j.quascirev.2005.12.013

Nitsche, F. O., Gohl, K., Larter, R. D., Hillenbrand, C.-D., Kuhn, G., Smith, J. A., Jacobs, S., Anderson, J. B., & Jakobsson, M. (2013). Paleo ice flow and subglacial meltwater dynamics in Pine Island Bay, West Antarctica. *The Cryosphere, 7*(1), 249-262. https://doi.org/10.5194/tc-7-249-2013

Noble, T., Rohling, E., Aitken, A. R. A., Bostock, H. C., Chase, Z., Gomez, N., et al. (2020). The sensitivity of the Antarctic Ice Sheet to a changing climate: Past, present, and future. *Reviews of Geophysics, 58*(4), e2019RG000663. https://doi.org/10.1029/2019RG000663

Nowicki, S., & Seroussi, H. (2018). Projections of future sea level contributions from the Greenland and Antarctic ice sheets: Challenges beyond dynamical ice sheet modeling. *Oceanography, 31*(2), 109–117. https://www.jstor.org/stable/26542657

Nye, J. F. (1970). Glacier sliding without cavitation in a linear viscous approximation. *Proceedings of the Royal Society A, 315*, 381-403. https://doi.org/10.1098/rspa.1970.0050

Oppenheimer, M., Glavovic, B., Hinkel, J., van de Wal, R., Magnan, A. K., Abd-Elgawad, A., Cai, R., Cifuentes-Jara, M., Deconto, R. M., Ghosh, T., & Hay, J. (2019). Sea level rise and implications for low lying islands, coasts and communities. *IPCC Special Report on the Ocean and Cryosphere in a Changing Climate, 355*(6321), 126–129. https://doi.org/10.1126/science.aam6284

Otosaka, I. N., Shepherd, A., Ivins, E. R., Schlegel, N.-J., Amory, C., van den Broeke, M. R., Horwath, M., Joughin, I., King, M. D., Krinner, G., Nowicki, S., Payne, A. J., Rignot, E., Scambos, T., Simon, K. M., Smith, B. E., Sørensen, L. S., Velicogna, I., Whitehouse, P. L., Agosta, C., Ahlstrøm, A. P., Blazquez, A., Colgan, W., Engdahl, M. E., Fettweis, X., Forsberg, R., Gallée, H., Gardner, A., Gilbert, L., Gourmelen, N., Groh, A., Gunter, B. C., Harig, C., Helm, V., Khan, S. A., Kittel, C., Konrad, H., Langen, P. L., Lecavalier, B. S., Liang, C.-C., Loomis, B. D., McMillan, M., Melini, D., Mernild, S. H., Mottram, R., Mouginot, J., Nilsson, J., Noël, B., Pattle, M. E., Peltier, W. R., Pie, N., Roca, M., Sasgen, I., Save, H. V., Seo, K.-W., Scheuchl, B., Schrama, E. J. O., Schröder, L., Simonsen, S. B., Slater, T., Spada, G., Sutterley, T. C., Vishwakarma, B. D., van Wessem, J. M., Wiese, D., van der Wal, W., & Wouters, B. (2023). Mass balance of the Greenland and Antarctic ice sheets from 1992 to 2020. *Earth System Science Data, 15*, 1597–1616. https://doi.org/10.5194/essd-15-1597-2023

Paolo, F. S., Padman, L., Fricker, H. A., Adusumilli, S., Howard, S., & Siegfried, M. R. (2018). Response of Pacific-sector Antarctic ice shelves to the El Niño/Southern Oscillation. *Nature Geoscience, 11*(2), 121–126. https://doi.org/10.1038/s41561-017-0033-0

Pattyn, F., Favier, L., Sun, S., & Durand, G. (2017). Progress in numerical modeling of Antarctic ice-sheet dynamics. *Current Climate Change Reports, 3*(3), 174–184. https://doi.org/10.1007/s40641-017-0069-7

Pollard, D., & DeConto, R. M. (2012). Description of a hybrid ice sheet-shelf model, and application to Antarctica. *Geoscientific Model Development, 5*, 1273–1295. https://doi.org/10.5194/gmd-5-1273-2012

Powell, R. D. (1981). A model for sedimentation by tidewater glaciers. *Annals of Glaciology, 2*, 129–134. https://doi.org/10.3189/172756481794352306

Pritchard, H. D., Ligtenberg, S. R. M., Fricker, H. A., Vaughan, D. G., van den Broeke, M. R., & Padman, L. (2012). Antarctic ice-sheet loss driven by basal melting of ice shelves. *Nature, 484*(7395), 502–505. https://doi.org/10.1038/nature10968

Prothro, L. O., Simkins, L. M., Majewski, W., & Anderson, J. B. (2018). Glacial retreat patterns and processes determined from integrated sedimentology and geomorphology records. *Marine Geology, 395*, 104–119. https://doi.org/10.1016/j.margeo.2017.09.012

Prothro, L. O., Majewski, W., Yokoyama, Y., Simkins, L. M., Anderson, J. B., Yamane, M., Miyairi, Y., & Ohkouchi, N. (2020). Timing and pathways of East Antarctic Ice Sheet retreat. *Quaternary Science Reviews, 230*, 106166. https://doi.org/10.1016/j.quascirev.2020.106166

Rignot, E. J. (1998). Fast recession of a West Antarctic glacier. *Science, 281*, 549-551. doi: 10.1126/science.281.5376.549

Rignot, E., Bamber, J. L., van den Broeke, M. R., Davis, C., Li, Y., van de Berg, W. J., & van Meijgaard, E. (2008). Recent Antarctic ice mass loss from radar interferometry and regional climate modelling. *Nature Geoscience, 1*(2), 106–110. https://doi.org/10.1038/ngeo102

Rignot, E., Mouginot, J., Scheuchl, B., van den Broeke, M., van Wessem, M. J., & Morlighem, M. (2019). Four decades of Antarctic Ice Sheet mass balance from 1979-2017. *Proceedings of the National Academy of Sciences, 116*(4), 1095-1103. https://doi.org/10.1073/pnas.1812883116

Rippin, D. M., Bamber, J. L., Siegert, M. J., Vaughan, D. G., & Corr, H. F. J. (2006). Basal conditions beneath enhanced-flow tributaries of Slessor Glacier, East Antarctica. *Journal of Glaciology, 52*(179), 481-490. https://doi.org/10.3189/172756506781828467

Rippin, D. M., Vaughan, D. G., & Corr, H. F. J. (2011). The basal roughness of Pine Island Glacier, West Antarctica. *Journal of Glaciology, 57*(201), 67-76. https://doi.org/10.3189/002214311795306574

Rippin, D. M., Bingham, R. G., Jordan, T. A., Wright, A. P., Ross, N., Corr, H. F. J., Ferraccioli, F., Le Brocq, A. M., Rose, K. C., & Siegert, M. J. (2014). Basal roughness of the Institute and Möller Ice Streams: Process determination and landscape interpretation. *Geomorphology, 214*, 481-490. https://doi.org/10.1016/j.geomorph.2014.01.021

Ritz, C., Edwards, T. L., Durand, G., Payne, A. J., Peyaud, V., & Hindmarsh, R. C. A. (2015). Potential sea-level rise from Antarctic ice-sheet instability constrained by observations. *Nature, 528*, 115-118. https://doi.org/10.1038/nature16147

Robel, A. A., Roe, G. H., & Haseloff, M. (2018). Response of marine-terminating glaciers to forcing: Time scales, sensitivities, instabilities, and stochastic dynamics. *Journal of Geophysical Research: Earth Surface, 123*, 2205–2227. https://doi.org/10.1029/2018JF004709

Robel, A. A., Seroussi, H., & Roe, G. H. (2019). Marine ice sheet instability amplifies and skews uncertainty in projections of future sea-level rise. *Proceedings of the National Academy of Sciences, 116*(30), 14887–14892. https://doi.org/10.1073/pnas.1904822116

Robel, A. A., Pegler, S. S., Catania, G., Felikson, D., & Simkins, L. M. (2022). Ambiguous stability of glaciers at bed peaks. *Journal of Glaciology, 68*(272), 1177-1195. https://doi.org/10.1017/jog.2022.31

Seroussi, H., Nakayama, Y., Larour, E., Menemenlis, D., Morlighem, M., Rignot, E., & Khazendar, A. (2017). Continued retreat of Thwaites Glacier, West Antarctica, controlled by bed topography and ocean circulation. *Geophysical Research Letters, 44*, 6191–6199. https://doi.org/10.1002/2017GL072910

Schoof, C. (2002). Basal perturbations under ice streams: form drag and surface expression. *Journal of Glaciology, 48*(162), 407-416. https://doi.org/10.3189/172756502781831269

Schoof, C. (2007). Ice sheet grounding line dynamics: Steady states, stability, and hysteresis. *Journal of Geophysical Research, 112*(F03S28). https://doi.org/10.1029/2006JF000664

Schroeder, D. M., Blankenship, D. D., Young, D. A., Witus, A. E., & Anderson, J. B. (2014). Airborne radar sounding evidence for deformable sediments and outcropping bedrock beneath Thwaites Glacier, West Antarctica. *Geophysical Research Letters, 41*, 7200–7208. https://doi.org/10.1002/2014GL061645

Shepherd, A., Fricker, H. A., & Farrell, S. L. (2018). Trends and connections across the Antarctic cryosphere. *Nature, 558*, 223–232. https://doi.org/10.1038/s41586-018-0171-6

Shepherd, A., Gilbert, L., Muir, A. S., Konrad, H., McMillan, M., Slater, T., et al. (2019). Trends in Antarctic Ice Sheet elevation and mass. *Geophysical Research Letters, 46*, 8174–8183. https://doi.org/10.1029/2019GL082182

Shipp, S., Anderson, J. B., & Domack, E. (1999). Late Pleistocene–Holocene retreat of the West Antarctic Ice-Sheet system in the Ross Sea: Part 1. Geophysical results. *Bulletin of the Geological Society of America, 111*(10), 1486–1516. https://doi.org/10.1130/0016-7606(1999)111<1486:lphrot>2.3.co;2

Shipp, S. S., Wellner, J. S., & Anderson, J. B. (2002). Retreat signature of a polar ice stream: sub-glacial geomorphic features and sediments from the Ross Sea, Antarctica. *Geological Society, London, Special Publications*, 203(1), 277–304. https://doi.org/10.1144/gsl.sp.2002.203.01.15

Siegert, M. J., Taylor, J., Paune, A. J., & Hubbard, B. (2004). Macro-scale bed roughness of the Siple Coast ice stream in West Antarctica. *Earth Surface Processes and Landforms, 29*(13), 1591-1596. https://doi.org/10.1002/esp.1100

Siegert, M. J., Taylor, J., & Payne, A. J. (2005). Spectral roughness of subglacial topography and implications for former ice-sheet dynamics in East Antarctica. *Global and Planetary Change, 45*(1-3), 249-263. https://doi.org/10.1016/j.gloplacha.2004.09.008

Simkins, L. M., Greenwood, S. L., & Anderson, J. B. (2018). Diagnosing ice sheet grounding line stability from landform morphology. *The Cryosphere, 12*, 2707–2726. https://doi.org/10.5194/tc-12-2707-2018

Smith, B. E., Raymond, C. F., & Scambos, T. (2006). Anisotropic texture of ice sheet surfaces. *Journal of Geophysical Research: Earth Surface, 111*, F01019. https://doi.org/10.1029/2005JF000393

Smith, M. W. (2014). Roughness in the Earth Sciences. *Earth-Science Reviews, 136*, 202-225. https://doi.org/10.1016/j.earscirev.2014.05.016

Smith, J. A., Graham, A. G. C., Post, A. L., Hillenbrand, C.-D., Bart, P. J., & Powell, R. D. (2019). The marine geological imprint of Antarctic ice shelves. *Nature Communications, 10*(1). https://doi.org/10.1038/s41467-019-13496-5

Spagnolo M., Clark C. D., Ely J. C., Stokes C. R., Anderson J. B., Andreassen K., Graham A. G. C. and King E. C. (2014), Size, shape and spatial arrangement of mega-scale glacial lineations from a large and diverse dataset, *Earth Surface Processes and Landforms*, 39, pages 1432–1448, doi: 10.1002/esp.3532

Stokes, C. R., & Clark, C. D. (2003). The Dubawnt Lake palaeo-ice stream: Evidence for dynamic ice sheet behaviour on the Canadian Shield and insights regarding the controls on ice-stream location and vigour. *Boreas, 32*(2), 263-279. https://doi.org/10.1111/j.1502-3885.2003.tb01442.x

Stokes, C. R., Clark, C. D., Lian, O. B., & Tulaczyk, S. (2007). Ice stream sticky spots: A review of their identification and influence beneath contemporary and palaeo-ice streams. *Earth-Science Reviews, 81*(3-4), 217-249. https://doi.org/10.1016/j.earscirev.2007.01.002

Stokes, C. R. (2018). Geomorphology under ice streams: Moving from form to process. *Earth Surface Processes and Landforms, 43*(1), 85-123. https://doi.org/10.1002/esp.4259

Taylor, J., Siegert, M. J., Payne, A. J., & Hubbard, B. (2004). Regional-scale bed roughness beneath ice masses: Measurement and analysis. *Computers & Geosciences, 30*(8), 899-908. https://doi.org/10.1016/j.cageo.2004.06.007

Tsai, V. C., Stewart, A. L., & Thompson, A. F. (2015). Marine ice-sheet profiles and stability under Coulomb basal conditions. *Journal of Glaciology*, 61, 205–215. https://doi.org/10.3189/2015JoG14J221

Tulaczyk, S., Kamb, W. B., & Engelhardt, H. F. (2000). Basal mechanics of Ice Stream B, west Antarctica: 1. Till mechanics. *Journal of Geophysical Research: Solid Earth*, 105(B1), 463–481. https://doi.org/10.1029/1999JB900329

Vaughan, D.G., Comiso, J.C., Allison, I., Carrasco, J., Kaser, G., Kwok, R., Mote, P., Murray, T., Paul, F., Ren, J., Rignot, E., Solomina, O., Steffen, K., & Zhang, T. (2013). Observations: Cryosphere. In *Climate Change 2013: The Physical Science Basis. Contribution of Working Group I to the Fifth Assessment Report of the Intergovernmental Panel on Climate Change* (pp. 317-382). T.F. Stocker et al. (Eds.). Cambridge University Press.

Weertman, J. (1957). On the sliding of glaciers. *Journal of Glaciology, 3*(21), 33-38. https://doi.org/10.3189/S0022143000024709

Weertman, J. (1964). The theory of glacier sliding. *Journal of Glaciology, 5*(39), 287-303. https://doi.org/10.3189/S0022143000029038

Weertman, J. (1974). Stability of the junction of an ice sheet and an ice shelf. *Journal of Glaciology, 13*(67), 3–11. https://doi.org/10.3189/S0022143000023327

Wellner, J. S., Lowe, A. L., Shipp, S. S., & Anderson, J. B. (2001). Distribution of glacial geomorphic features on the Antarctic continental shelf and correlation with substrate: Implications for ice behavior. *Journal of Glaciology, 47*(158), 397-411. https://doi.org/10.3189/172756501781832043

Whillans, I. M., & van der Veen, C. J. (1997). The role of lateral drag in the dynamics of Ice Stream B, Antarctica. *Journal of Glaciology, 43*(144), 231-237. https://doi.org/10.3189/S0022143000003178

Winsborrow, M. C. M., Clark, C. D., & Stokes, C. R. (2010). What controls the location of ice streams? *Earth-Science Reviews, 103*(1-2), 45-59. https://doi.org/10.1016/j.earscirev.2010.07.003

Wise, M., Dowdeswell, J., Jakobsson, M., & Larter, R. (2017). Evidence of marine ice-cliff instability in Pine Island Bay from iceberg-keel plough marks. *Nature, 550*, 506–510. https://doi.org/10.1038/nature24458